

NASA TM-87771

NASA Technical Memorandum 87771

NASA-TM-87771 19860020435

TENSION STRENGTH OF A THICK GRAPHITE/EPOXY
LAMINATE AFTER IMPACT BY A 1/2-IN.-RADIUS IMPACTOR

C. C. Poe, Jr., W. Illg, and D. P. Garber

JULY 1986

FOR REFERENCE

NOT TO BE TAKEN FROM THIS ROOM

LIBRARY COPY

AUG 1 6 1986

LANGLEY RESEARCH CENTER
LIBRARY, NASA
HAMPTON, VIRGINIA

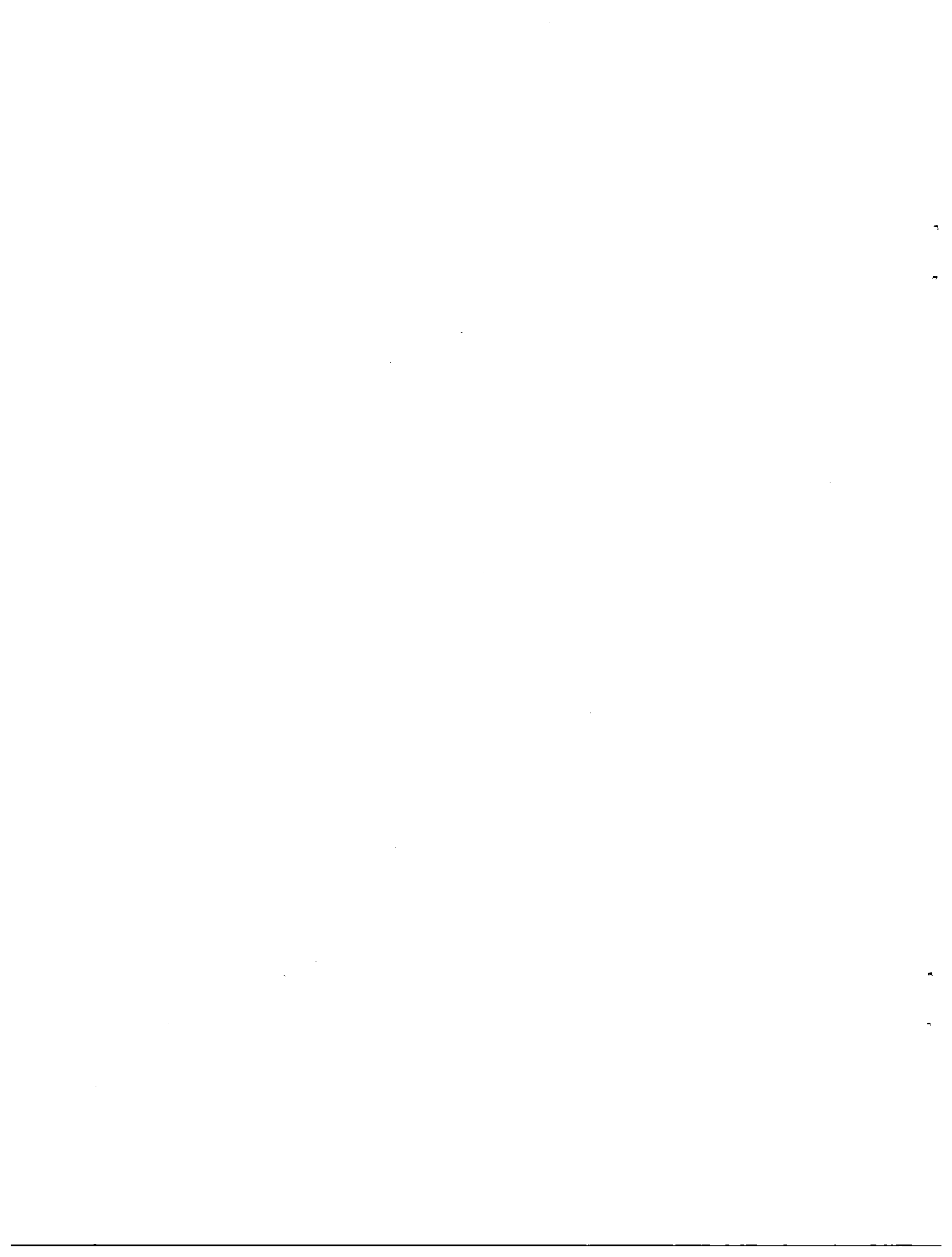
NASA

National Aeronautics and
Space Administration

Langley Research Center
Hampton, Virginia 23665



NF01642



CONTENTS

	page
LIST OF TABLES	ii
LIST OF FIGURES	iii
SUMMARY OF SIGNIFICANT FINDINGS	1
INTRODUCTION	2
SYMBOLS	3
MATERIAL	5
TEST APPARATUS AND PROCEDURE	7
Impact Tests	7
Static Compliance Tests	9
X-ray Tests	10
Residual Strength Tests	10
Strength Tests of Undamaged Specimens	11
RESULTS	11
Strength Tests of Undamaged Specimens	11
Strengths	11
Gripping failures	12
Wrinkle-type defects	13
Load-stroke curves	13
Stress-strain curves	14
Static Compliance Tests	15
Impact Tests	16
Impact force	16
Impact damage	21
Residual Strength Tests	24
Radiographs made after loading to first-ligament failure	24
Load-stroke records	25
Strengths	25
Equivalent cut depth	28
Delamination depths after loading to first-ligament failure	29
CONCLUSIONS	31
REFERENCES	33
TABLES	34
FIGURES	42

LIST OF TABLES

	page
Table I.- Test results for filled ring.	34
Table II.- Test results for empty ring.	37
Table III.- Strengths of undamaged specimens.	40

LIST OF FIGURES

	page
1. Solid rocket motors of space shuttle with FWC's.	42
2. Specimens and testing sequence.	43
3. Sketch of impactor.	44
4. Calibration check of impactor signals.	
(a) Energy correlation.	45
(b) Impulse correlation.	46
5. Strengths of undamaged specimens.	47
6. Cumulative probability of strengths for undamaged specimens and 36-in.-diameter cylinders.	48
7. Cumulative probability of normalized strengths for undamaged specimens and 36-in.-dia. cylinders.	49
8. Photographs of failed undamaged specimens.	
(a) 1.0 inches wide.	50
(b) 1.3 inches wide.	51
(c) 1.5 inches wide.	52
9. Photograph of fracture detail in specimen 3-28.	53
10. Photographs of edges of a tensile specimen and a coupon from an actual FWC.	54
11. Load-stroke records for undamaged specimens.	
(a) 1.0 inches wide.	55
(b) 1.3 inches wide.	56
(c) 1.5 inches wide.	57
12. Load versus strain for 1-in.-wide undamaged specimens.	58
13. Effect of kinetic energy on impact force versus time for 19.9-lbm impactor.	
(a) Filled ring.	59
(b) Empty ring.	60
14. Effect of impact mass on impact force versus time.	
(a) Filled ring, KE = 50 ft-lbf.	61
(b) Empty ring, KE = 50 ft-lbf.	62
(c) Empty ring, KE = 100 ft-lbf.	63
15. Fourier coefficients of accelerometer signal for 19.9 lbm impactor and 99.5 ft-lbf kinetic energy.	
(a) Filled ring.	64
(b) Empty ring.	65

16.	Velocity ratio versus mass ratio.	66
17.	Impacter force versus impacter energy.	
	(a) Filled ring, $\bar{m}_2 = 159$ lbm.	67
	(b) Empty ring, $\bar{m}_2 = 22$ lbm.	68
18.	Impacter force versus impacter energy for filled and empty rings.	69
19.	Principal shear stress contours from Love's solution for hemispherical contact pressure.	70
20.	Damage size versus contact pressure according to Love's solution and principal shear criterion for failure.	71
21.	Contact diameter versus impact force.	72
22.	Average contact pressure versus impact force.	73
23.	Comparison of predicted impact damage and radiographs.	74
24.	Radiographs of first-ligament failure - filled ring.	
	(a) Specimen 7-6 (P = 9.2 kips).	75
	(b) Specimen 7-27 (P = 14.6 kips).	76
	(c) Specimen 7-7 (P = 13.5 kips).	77
	(d) Specimen 7-1.	78
	(e) Specimen 7-13.	79
	(f) Specimen 7-8 (P = 17.8 kips).	80
	(g) Specimen 7-2 (P = 17.9 kips).	81
	(h) Specimen 7-12 (P = 21.7 kips).	82
	(i) Specimen 7-14 (P = 21.2 kips).	83
25.	Radiographs of first-ligament failure - empty ring.	
	(a) Specimen 5-26 (P = 8.9 kips).	84
	(b) Specimen 5-5 (P = 8.3 kips).	85
	(c) Specimen 5-17 (P = 8.4 kips).	86
	(d) Specimen 5-16 (P = 14.9 kips).	87
	(e) Specimen 5-18 (P = 12.4 kips).	88
	(f) Specimen 5-41 (P = 9.7 kips).	89
	(g) Specimen 5-6 (P = 17.2 kips).	90
	(h) Specimen 5-21 (P = 13.9 kips).	91
	(i) Specimen 5-23 (P = 11.6 kips).	92
	(j) Specimen 5-32 (P = 19.0 kips).	93
	(k) Specimen 5-13.	94
	(l) Specimen 5-14 (P = 20.4 kips).	95
26.	Load-stroke records for impacted specimens from filled ring.	
	(a) $m_1 = 6.1$ lbm and KE = 30.3 ft-lbf.	96
	(b) $m_1 = 6.1$ lbm and KE = 60.6 ft-lbf.	97
	(c) $m_1 = 11.1$ lbm and KE = 55.5 ft-lbf.	98
	(d) $m_1 = 11.1$ lbm and KE = 111. ft-lbf.	99

(e) $m_1 = 19.9$ lbm and KE = 49.8 ft-lbf.	100
(f) $m_1 = 19.9$ lbm and KE = 99.5 ft-lbf.	101
(g) $m_1 = 19.9$ lbm and KE = 199. ft-lbf.	102
(h) $m_1 = 41.1$ lbm and KE = 51.4 ft-lbf.	103
(i) $m_1 = 41.1$ lbm and KE = 206. ft-lbf.	104
27. Load-stroke records for impacted specimens from empty ring.	
(a) $m_1 = 6.06$ lbm and KE = 30.3 ft-lbf.	105
(b) $m_1 = 6.06$ lbm and KE = 60.6 ft-lbf.	106
(c) $m_1 = 11.1$ lbm and KE = 27.8 ft-lbf.	107
(d) $m_1 = 11.1$ lbm and KE = 55.5 ft-lbf.	108
(e) $m_1 = 11.1$ lbm and KE = 111. ft-lbf.	109
(f) $m_1 = 19.9$ lbm and KE = 49.8 ft-lbf.	110
(g) $m_1 = 19.9$ lbm and KE = 99.5 ft-lbf.	111
(h) $m_1 = 19.9$ lbm and KE = 199. ft-lbf.	112
(i) $m_1 = 41.1$ lbm and KE = 103. ft-lbf.	113
(j) $m_1 = 41.1$ lbm and KE = 206. ft-lbf.	114
(k) $m_1 = 41.1$ lbm and KE = 329. ft-lbf.	115
28. Ratio of stress for first-ligament failure to undamaged strength versus impact force.	116
29. Ratio of stress for remaining-ligament failure to undamaged strength versus impact force.	117
30. Cumulative frequency versus coefficient of variation of strengths for a given impactor mass and kinetic energy.	118
31. Comparison of tensile tests and design conditions.	119
32. Comparison of fracture behavior for full- and quarter-scale laminates. $c/a = 0.8$ and $K_Q = 27.3$ ksi/in.	120
33. Comparison of equivalent cut depth and measured and predicted damage depth.	121
34. Comparison of delamination and damage depth.	122
35. Photographs of deepest layer with fibers broken by impact (second helical layer below the outermost hoop layer).	123



SUMMARY OF SIGNIFICANT FINDINGS

NASA is developing graphite/epoxy filament-wound cases (FWC) for the solid rocket motors of the space shuttle. The cases are 12 feet in diameter and approximately 25 feet in length. They are wet-wound with AS4W graphite fiber and HBRF-55A epoxy. The membrane region away from the ends is about 1.4 inches thick. A test program is being conducted by Langley Research Center to determine the residual tension strength of an FWC after low-velocity impacts to the membrane region. Cylinders or rings that were 30 inches in diameter, 12 inches long, and 1.4 inches thick were made by Hercules Inc. for specimens.

Preliminary tests indicated that impacts by a blunt impactor were the most critical because the damage was not visible. Accordingly, many additional tests were conducted with 1/2-inch-radius impactors of various masses and kinetic energies. After the impactors were dropped onto the 30-inch-diameter rings, the rings were cut into 2-by-12-inch specimens. Each was centered on an impact site. Two rings were impacted 44 times each (every 2 inches of circumference). One ring was empty and one was filled with inert propellant. The propellant was cast into the ring, much like an actual FWC. The impactor masses varied from 6.1 to 41.1 lbm. They were instrumented to measure impact force and dropped from various heights giving kinetic energies from 30.3 to 329 ft-lbf. The specimens were x-rayed to determine the extent of impact damage, and loaded in uniaxial tension to measure the residual strength.

The impact forces were generally larger for the filled ring than for the empty ring and increased with kinetic energy and the ratio of impactor mass to ring mass. The propellant increased the inertia of the ring much more than its stiffness. The impact forces ranged from 8 to 22 kips. Up to about 17 kips, the impacts did not cause visible surface damage. From 17 to 22 kips, the impacts made shallow but visible craters. The strengths were reduced by as much as 37 percent without visible surface damage. Even the radiographs did not generally reveal the nonvisible impact damage. Moreover, the radiographs did not reveal the full extent of impact damage even when the impactors made craters. For the largest impact forces, the strengths were reduced by as much as 50 percent. The required factor of safety in the membrane region is 1.4. The factors of safety corresponding to 37 and 50 percent strength losses were estimated to be 1.3 and 1.0, respectively.

The local deformations, contact diameters, and contact pressures were predicted reasonably well with the Hertz law. Also, the effect on impact force of kinetic energy, impactor mass, and ring mass were predicted reasonably well with rigid body mechanics. However, the impact force predicted with rigid body mechanics using the static stiffness of the rings was much too small. Because the impact duration was only a few milliseconds, the rings were effectively smaller than their actual size and very stiff. The depth of broken fibers, which was determined by destructive examination, was predicted reasonably well using Love's solution for pressure applied on part of the boundary of a semi-infinite body and a principal shear stress criterion. However, the reduction in strengths corresponded to damage deeper than the depth of the broken fibers. Fibers below the broken fibers were apparently weakened by the impacts.

INTRODUCTION

NASA is developing graphite/epoxy filament-wound cases (FWC) for the solid rocket motors of the space shuttle. Each motor consists of four cases -- a forward case, two center cases, and an aft case. The cases are 12 feet in diameter and the ends are joined to short steel segments with pins. The forward and center cases are approximately 25 feet in length, and the aft case is somewhat shorter. They are wet-wound with AS4W graphite fiber and HBRF-55A epoxy. The membrane region away from the ends is about 1.4 inches thick. A test program is being conducted by Langley Research Center to determine the residual tension strength of an FWC after low-velocity impacts to the membrane region. Test specimens 2 by 12 inches were cut from 30-inch-diameter by 12-inch-long cylinders or rings. The rings were cut from an 84-inch-long cylinder of full-thickness that was made by Hercules Inc. Following impact, the specimens were loaded uniaxially to failure to measure residual strengths. In order to apply uniaxial load in the hoop direction and have straight specimens, the 30-inch-diameter cylinder was wound with fiber orientations rotated 90° so that the hoop direction of the FWC was the longitudinal direction of the 30-inch-diameter cylinder.

In the initial phase of the program, preliminary tests were conducted in which impacters of various shapes and masses were dropped on the 2-by-12-inch specimens from various heights. The specimens were lying on inert propellant to represent an FWC loaded with propellant. The impacted specimens were then loaded to failure. The shapes of the impacters were 1/4- and 1/2-inch-radius hemispheres, 1/4-inch-diameter rod, and 90° corner. The strengths were about the same for the various shapes, but the damage caused by the 1/2-inch-radius impacters was much less visible. Thus, the 1/2-inch-radius impacters were considered to be the most critical. Also, surface cuts of various sizes were made in some of the specimens to demonstrate that impact damage and surface cuts are equivalent. These results were reported in reference 1.

Results from the second phase of this test program are reported here. In this phase, many additional tests were conducted with the more critical 1/2-inch-radius impacters. The impacters were instrumented to measure impact force. In contrast to the preliminary tests in the first phase, the impacters were dropped onto the 30-inch-diameter by 12-inch-long rings rather than the 2-by-12-inch specimens. After the impacts, the rings were cut into 2-by-12-inch specimens. Each was centered on an impact site. Two rings were impacted 44 times each (every 2 inches of circumference). One ring was empty and one was filled with inert propellant. The propellant was cast into the ring, much like an actual FWC. The impactor masses varied from 6.1 to 41.1 lbm. They were dropped from various heights giving kinetic energies from 30.3 to 329 ft-lbf. The specimens were x-rayed to determine the extent of impact damage, and loaded in uniaxial tension to measure the residual strength. A few specimens were depled and the fibers were examined for impact damage. In addition, 16 specimens without impacts were loaded to failure to determine the undamaged strengths. Rigid body mechanics and the Hertz law were used to predict impact force, local deformations, contact diameters, and contact pressures. The depth of impact damage was predicted using Love's solution for pressure applied on part of the boundary of a semi-infinite body and a principal shear stress criterion. The predictions were compared to the experiments.

SYMBOLS

a	equivalent surface cut depth or impact damage depth, in.
a(t)	accelerometer signal, ft/sec ²
c	half-length of surface cut, in.
D	contact diameter, in.
E	Young's modulus, psi
F(t)	strain gage signal
G	Shear modulus, psi
k _{eq}	equivalent spring constant, lbf/in.
k _f	spring constant for flexure, lbf/in.
k _h	spring constant for a linear Hertz law, lbf/in.
k ₁ , k ₂	factors in the Hertz law, psi ⁻¹
K _Q	fracture toughness, psi/in.
KE	kinetic energy, ft-lbf
L	length of impactor rod, in.
m ₁	mass of impactor, lbm
m ₂	mass of target or composite ring, lbm
\bar{m}_2	effective mass of composite ring, lbm
n	factor in the Hertz law, lbf/in. ^{3/2}
P	impact force, lbf
p _c	average contact pressure, psi
R ₁	radius of impactor, in.
S _c	gross stress for failure of first ligament, psi

S_u	allowable principal shear stress, psi
t	time, sec
t_o	impact duration, sec
u_f	flexural displacement, in.
u_h	Hertz displacement, in.
v_i	initial velocity of impacter (immediately before collision), ft/sec
v_f	final velocity of impacter (immediately after last separation), ft/sec
v_r	rebound velocity of impacter (immediately after first separation), ft/sec
W	width of specimen in test section, in.
ν	Poisson's ratio

Subscripts:

x, y	Cartesian coordinates (The x-direction corresponds both to the axial direction of the special 30-inch-diameter full-thickness cylinder and to the hoop direction of the FWC.)
ρ, z	polar coordinates (The z-direction is normal to the laminate.)
$1, 2$	principal ply coordinates (1 refers to fiber direction) or refers to impacter and target

Abbreviations:

FWC	Filament Wound Case
MEOP	Maximum Expected Operating Pressure

The following notation is used to describe the winding pattern or layup. Fiber angles are separated by a slash and listed in the order of layup from the outside to the inside. A numerical subscript on the fiber angle denotes how many consecutive layers are at that angle. Likewise, a numerical subscript on a group of layers denotes how many consecutive groups have that pattern. Within a group of helical layers, the plus and minus fiber angles actually pass over and under one another as in a weave. Thus, the order of the helical layers within a group varies over the laminate.

MATERIAL

The membrane region of an aft FWC segment was chosen for this investigation. This segment is 12 feet in diameter, approximately 25 feet long, and about 1.4 inches thick in the membrane region. From outside to inside, the layers are as follows:

$(\pm 33.5^\circ)_2 / 90^\circ / [(\pm 33.5^\circ)_2 / 90^\circ]_3 / [(\pm 33.5^\circ)_2 / 90^\circ]_7 / (\pm 33.5^\circ / 90^\circ)_4 / (\pm 33.5^\circ)_2 / (0^\circ / 90^\circ)$

where the 90° layers are the hoop wraps and the $\pm 33.5^\circ$ layers are the helicals.

The underlined $\pm 33.5^\circ$ helical layers have about 1.6 times as many tows per inch per layer as the other helical layers and are thus thicker in the same

proportion. The $0^\circ / 90^\circ$ layers at the inner surface are actually one layer of cloth. The layup is balanced (equal numbers of $+33.5^\circ$ and -33.5° layers) but not symmetrical about the midplane. Most of the hoop layers are closer to the inner surface than the outer surface.

Except for hydrostatically testing actual FWC's, no biaxial loading equipment was available to break a full-thickness FWC specimen with a two-to-one biaxial stress ratio. Moreover, specimens from an FWC that are loaded uniaxially in the hoop direction (the most highly stressed direction) would bend because of the curvature of the hoop fibers. The most logical option was to make a special full-thickness case with the winding angles rotated 90° , and uniaxially load specimens in the longitudinal direction. Then the hoop fibers of the FWC, which correspond to the axial fibers of the special case, would be straight. Hercules Inc. had a 30-inch-diameter mandrel available, but 0° (longitudinal) plies could not be wound. Thus, the 0° layers were hand-laid on the mandrel and the helicals were wound wet. The hand-laid material was a unidirectional prepregged-broadgoods. The different epoxys in the wet-winding and broadgoods were compatible. These layers of broadgoods had the same fiber count and thickness as the wet-wound hoop layers in the FWC.

The dimensions and winding angles of the special case are shown in figure 2(a). Each hoop layer in the FWC is replaced by three plies of broadgoods. The case is 1.4 inches thick, 30 inches in diameter, and 7 feet long. It was cut into seven 12-inch-long rings for testing. From outside to inside, the layers are as follows:

$(\pm 56.5^\circ)_2 / 0^\circ / [(\pm 56.5^\circ)_2 / 0^\circ]_3 / [(\pm 56.5^\circ)_2 / 0^\circ]_7 / (\pm 56.5^\circ / 0^\circ)_4 / (\pm 56.5^\circ)_2 / (90^\circ / 0^\circ)$.

The graphite fiber is Hercules Inc.'s AS4W-12K, and the winding resin is Hercules Inc.'s HBRF-55A. The epoxy in the unidirectional broadgoods is Hercules Inc.'s MX-16. Fiber-lot-acceptance (FLA) tests were conducted on the fiber used to make the test case. Properties of the helical fiber, broadgoods fiber, and matrix or winding resin are given in the table below. (The helical and broadgoods fibers were from different lots.)

	Helical fiber	Broadgoods fiber	Matrix
Tensile modulus, Msi	33	33	0.414
Poisson's ratio	-	-	.35
Tensile strength, ksi	574	544	-
Elongation at failure	0.0167	-	-
Density, lbm/in. ³	0.0648	.0642	.0444

The physical properties, which were measured on six coupons cut from the ends of the test case, and lamina constants were reported by Hercules Inc. to be as follows:

Composite density, lbm/in. ³	0.05397
Resin mass fraction	0.3459
Resin volume fraction	0.3845
Fiber volume fraction	0.5449
Void content	0.0706

	Unidirectional broadgoods	Helical layers	Cut helical layers	Cloth
E_{11} , Msi	15.35	16.17	16.17	8.596
E_{22} , Msi	0.9272	.2781	.2781	8.596
G_{12} , Msi	0.6490	.6212	.6212	.5331
ν_{12}	0.2750	.2670	.2670	.0348
Thickness per ... layer, in.	^a 0.01683	.01683	.02804	.01683

^aEqual to three plies of broadgoods.

The elastic constants of the test case laminate were predicted with lamination theory using the lamina constants in the table above. It was assumed that bending and stretching were not coupled, that is, the laminate was symmetric. The predictions are $E_x = 4.44$ Msi, $E_y = 5.66$ Msi, $G_{xy} = 2.86$ Msi, $\nu_{xy} = 0.351$, and $\nu_{yx} = 0.447$. (The x-direction corresponds to the axial direction of the test case and the hoop direction of the FWC.)

TEST APPARATUS AND PROCEDURE

Impact Tests

Rings 5 and 7 of the special case were impacted with the 1/2-inch-radius impactor. See figure 2(b). It was believed that the 30-inch-diameter rings were large enough to simulate the full-sized FWC's because the disturbance would only travel about 12 inches during the impact event (ref. 1). The impact force for a FWC containing propellant should be higher than that for an empty FWC. Thus, it was desirable to simulate the empty and filled FWC's. To this end, inert propellant was cast in ring 7 by Morton Thiokol International using a procedure similar to that used to cast propellant in an actual FWC. Ring 5 was left empty.

Each ring was impacted 44 times with the following masses and kinetic energies.

Mass, lbm	Kinetic energy, ft-lbf	Comments
6.1	30.3 60.6	
11.1	27.8 55.5 111.	ring 5 only
19.9	49.8 99.5 199.	
41.1	51.4 103. 206. 329.	ring 7 only ring 5 only ring 5 only

Prior to impact, 44 impact sites were marked on each ring at equal intervals of arc length (2 inches plus an amount to allow for the kerf of the saw and final machining). The specimens were consecutively numbered 5-1 through 5-44 and 7-1 through 7-44 for rings 5 and 7, respectively. The impact sites were selected so that no contiguous specimens were impacted with the same mass and energy. Each ring was impacted, rotated, and impacted again until all 44 impacts were made. Radiographs indicated that the impact damage never extended into adjacent specimens. The empty ring lay on a thin rubber sheet in a shallow aluminum cradle and was secured to the concrete floor during impact with bolts and a cross-bar to prevent rebound. The filled ring lay on the same rubber sheet and cradle during impact, but the propellant prevented the use of the bolts and cross-bar. However, it was so massive compared to the impacters that its rebound was imperceptible and attachment to the floor was not necessary. (The empty and filled rings weighed 89 and 635 lbf, respectively.)

The impacts were made by free-falling masses. A description of the apparatus is given in reference 1. A sketch of the impacters is shown in figure 3. The impacters consisted of three basic parts: a 2-inch-diameter steel rod, a tup, and a striker or indenter. Four rods of different masses were used. The lengths of the rods and total masses are given in the table in figure 3. The steel tup was recessed into one end of the rod. The tup contained a piezoelectric accelerometer and four strain gages for measuring acceleration and impact force. A steel indenter shaped like a 1/2-inch-radius hemisphere was screwed into the end of the tup. The accelerometer and strain gage signals were transmitted to a digital storage oscilloscope by wires that passed through slots in the tup and rod. The oscilloscope recorded the signals at the rate of 500,000 samples per second and only began storing data 100 μ sec before the signals exceeded a threshold value. The accelerometer signal was unfiltered, but oscillations in the strain gage signal above 10 khz were filtered out.

The velocity at impact was measured with a laser type velocimeter. The laser was located a few inches above the rings. Newton's law was used to extrapolate the measured velocity to the surface of the rings. The kinetic energies calculated from the measured velocities were within a few percent of the preselected potential energies of the impacter masses. Thus, the velocity measurements are not reported.

The area of contact between the specimen and the 1/2-inch-radius impactor was recorded by placing a sheet of paper covered by a sheet of carbon paper on the specimen before the impactor was dropped. The pressure over the contact area transferred carbon to the paper. The diameter of the carbon area was measured with a scale.

The impact forces and contact diameters are given in tables I and II for the filled and empty rings respectively.

The accelerometer in the tup can measure accelerations from 0 to 20,000 g's in the range of 5 to 15,000 Hz and has a resonant frequency of 80 kHz. It was calibrated in a centrifugal acceleration device. The strain gages, which were connected in series, were statically calibrated in a testing machine by applying a load to the indenter and reacting it at the opposite end of the rod. The capability of the strain gages and accelerometer to make dynamic measurements was verified by checking energy and momentum balances. The kinetic energy is plotted against work in figure 4(a). Sometimes the signals were improperly recorded. Calculations for those tests are not plotted. However, the data that are plotted do represent all the impact conditions. Kinetic energy was calculated with $m_1 v_i^2 / 2$, where m_1 is the mass of the impactor and v_i is the initial impactor velocity from the velocimeter and work was calculated with $\int F(t) [\int a(t) dt] dt$, where $F(t)$ is the strain gage signal and $a(t)$ is the accelerometer signal. The impulse is plotted against the change in momentum in figure 4(b). Impulse was calculated with $\int F(t) dt$ and change in momentum was calculated with $m_1 (v_i - v_f)$, where m_1 , v_i , and $F(t)$ are the same as before and v_f is the final velocity after the last collision determined from $\int a(t) dt$. The solid lines in figures 4(a) and 4(b) represent perfect correlation and the dashed lines represent a plus and minus 10 percent deviation. Most of the calculations are well within the 10 percent lines. Thus, the energy and momentum balance quite well.

Static Compliance Tests

One of the specimens from the empty ring was not impacted. Instead, the impactor was mounted in a large testing machine and statically pressed against the ring. The force was reacted at the opposite side of the ring, much as in the case of the impact tests. The maximum force applied by the testing machine to the ring was 16,800 lbf, which corresponded to the impact force produced by some of the impacts. The intent of this test was to measure the static compliance and determine if strength loss is the same for a statically and a dynamically applied impact force. The total displacement and the displacement of the inner surface beneath the impactor were measured. The difference between the displacements is approximately the displacement given by the Hertz law.

Also, a force of 16,920 lbf was statically applied to one specimen from ring 1, which was filled with inert propellant like ring 7. (All the specimens in ring 7 had been impacted when the decision was made to conduct these tests. The intention was to apply 16,800 lbf as before, but a slight error was made.) The total displacement and the displacement of the inner surface at the edge was measured. The displacement of the inner surface beneath the impactor could not be measured because of the inert propellant.

X-ray Tests

After the static tests and impacts were completed, each ring was cut into 44 specimens that were approximately 2-inches wide by 12-inches long. See figure 2(c). The specimens were centered on the impact sites. Next, the cut edges were ground flat and parallel so that the width was exactly 2 inches. Then the impacted face of each specimen was soaked in a zinc iodide penetrant for half an hour, and radiographs were made from the top and side. The penetrant was contained by a circular dam on the surface of the specimen. The depth of impact damage in the radiographs was measured and recorded in tables I and II. When the impacters made craters, the surface around the crater was pushed up by the material that was squeezed aside and wedged between layers. Then the depths were measured from the original surface, not the raised surface.

Residual Strength Tests

After the specimens were x-rayed, circular arcs were symmetrically ground into the specimens' edges with a 18.5-inch-diameter silicon carbide wheel to reduce the width in the test section to 1.3 or 1.5 inches. See figure 2(d). The preliminary investigation in reference 1 revealed that, even with impact damage, straight sided specimens tended to fail prematurely beneath the leading edges of the grips. The widest test section was desirable in order to minimize edge effects. Thus, the 1.3-inch-wide test sections were used for the lowest kinetic energies where the least damage was expected, and the 1.5-inch-wide test sections for higher energies. Approximately 3-1/2 inches on each end remained a full 2 inches wide for gripping.

After the specimens were machined, they were uniaxially loaded to failure in a 100,000 lbf stroke-controlled, hydraulic testing machine with hydraulically actuated grips. (The preliminary tests reported in reference 1 indicated that partial failures were more difficult to detect when load was controlled.) The load and stroke signals were recorded on an x-y recorder.

To allow for the curved surfaces of the specimens, aluminum shims were placed between the surfaces of the specimens and grips. They were 3/8 inch thick, 4 inches long, and 2 inches wide. One surface was flat and the other conformed to the curvature of the specimens. Sheets of abrasive screen were placed between the shims and specimen to increase the coefficient of friction and prevent slip. Due to the squeezing action of the grips, the stresses beneath the leading edge of a grip are singular. For this reason, the specimens were inserted into the grips so that the leading edge of the grips was even with the shoulders of the specimens (intersections of the flat sides with the circular arcs) and did not extend into the narrower test section. On the other hand, the shims did extend at least 1/8 inch beyond the leading edge of the grips and shoulder of the specimen. In this way, the singular stresses were alleviated.

Most of the impacted specimens failed in two stages: first the layers with impact damage (first ligament) and then, with increasing load, the others (remaining ligament). When the first ligament failed, it seemed to delaminate simultaneously from the remaining ligament. The failing stresses of the first and remaining ligaments are given in tables I and II. The stresses were

calculated by dividing the loads by the gross area of the test section. The thickness was assumed to be 1.4 inches for all specimens.

For each combination of impactor mass and kinetic energy, one of the duplicate specimens was not loaded to complete failure. Instead, it was unloaded when the first ligament failed, removed from the testing machine, and x-rayed. Then, it was reinstalled in the testing machine and loaded to complete failure. Depths of the delaminations in the radiographs were measured. The delamination depths are also given in tables I and II.

Strength Tests of Undamaged Specimens

The strengths of only three undamaged specimens were reported in reference 1. The width of the test sections in those three specimens was 1 inch. Since then, impacted specimens that were 1.3- and 1.5-inches wide have been tested. In order to increase the data base of undamaged strengths and to determine the effect of specimen width, sixteen undamaged specimens with 1.0, 1.3, and 1.5-inch-wide test sections were loaded to failure in tension using the same testing machine and procedure as that used for the impacted specimens. The failing stresses, which were calculated in the same manner as those of the impacted specimens, are given in table III.

In order to reveal any misalignments in the testing machine that might cause bending, some of the 16 specimens were oriented with the inside surfaces to the front of the testing machine, and others were oriented with the inside surfaces to the back. Inside surface denotes the concave side of the specimen that was in contact with the mandrel. In the specimen names in table III, the suffixes A and B denote the two different positions of the specimens. (All of the impacted specimens in tables I and II were loaded in position A.) Also, strain gages were affixed to the inside and outside surfaces of five of the 1-inch-wide specimens to reveal any bending strains in the test section. They were located midway between the edges and ends of the specimens. The strain gage bridges were balanced before the specimens were clamped in the grips in order to measure the clamp-up strains.

RESULTS

Strength Tests of Undamaged Specimens

Strengths.- Average values of the undamaged strengths in table III are plotted in figure 5. The three 1-inch-wide undamaged specimens in reference 1 were tested in position A. The strengths are about the same for the different widths and positions. The coefficient of variation is below 10 percent for most of the groups of specimens. For all undamaged specimens, the average strength is 50.1 ksi and the coefficient of variation is 0.0805.

Hercules Inc. made and tested numerous 36-inch-diameter cylinders with a scaled-down thickness to determine design allowables for the FWC's. The cumulative probability of exceeding a given strength is plotted in figure 6. The strengths are given in terms of hoop fiber stress at failure. Using lamination theory, the hoop fiber stresses for the undamaged specimens in table

III were calculated and plotted in figure 6 for comparison. The mean value for the tensile specimens is 38 percent less than that for the cylinders, 317 ksi compared to 513 ksi. For the 36-inch-diameter cylinders, the mean fiber strength as determined from fiber-lot-acceptance tests was 590 ksi (ref. 1). The mean strength of the broadgoods fiber used in making the special 30-inch-diameter cylinder was 544 ksi. Thus, one would expect the stress in the hoop fibers of the tensile specimens at failure to be about 473 ksi ($513 \times 544 / 590$), not 317 ksi!

The fiber stresses in figure 6 were normalized by their mean values and replotted in figure 7. The normalized fiber stresses for the tensile specimens and cylinders coincide, indicating that the variability in the two sets of data is about the same. Thus, the cause of the low strengths is probably the specimen configuration itself or some small-scale defect in the material that is uniformly distributed throughout the laminate.

The only unusual characteristic of the specimen configuration is the relatively small width compared to the thickness. Fibers of finite length that are imbedded in matrix have zero axial stress at the ends but are fully stressed only a short distance (less than 10 fiber diameters) from the ends. Thus, for relatively wide specimens, the off-axis plies that terminate at a specimen's edge are fully stressed across virtually the entire width of the specimen. However, for these thick and narrow specimens, the helicals may not be fully stressed across a significant portion of the width. Accordingly, Dr. I. S. Raju of Analytical Services and Materials, Inc., Tabb, Virginia analyzed the FWC laminate and found that the off-axis layers were fully stressed a distance from the free edge equal to the thickness of the repeating group of layers, which is about 0.13 inches or about 10 percent of the specimens' widths. (Similar results are reported in reference 2 for thick laminates with other layups.) Lamination theory, which assumes that the helical fibers are fully stressed, predicts that the helical layers carry only 20 percent of the hoop load. Thus, if the layers remain fully bonded, the edges would reduce the hoop strength by less than 4 percent (two times 10 percent of 20 percent). Even if interlaminar stresses at the edges cause the helical layers to completely delaminate from the hoop layers, the hoop strength would be reduced no more than 20 percent. For the FWC layup, interlaminar failure is not likely to occur under static loading. Moreover, it was shown in reference 2 that thick laminates are much less likely to delaminate than thin laminates. Thus, edge effects alone are not likely to have caused the low strengths.

Gripping failures.— Photographs of 15 of the 16 broken specimens are shown in figure 8. The inner surfaces of the laminate are toward the viewer. The light and dark bands are the hoop and helical layers, respectively. Specimen 3-28 was inadvertently left out of the photograph in figure 8(a). It looked much like 3-8, 3-18, and 3-30. One can see in figures 8(a) and 8(c) that the inner surface layers of two of the 1-inch-wide specimens (3-10 and 3-20) and all of the 1.5-inch-wide specimens broke just inside the test section at the edge of an aluminum shim and delaminated from the remainder of the laminate. Also, for two of the 1.5-inch-wide specimens (4-19 and 4-34), the outer surface layers also broke at the edge of a shim. On the other hand, the fracture paths in the 1.3-inch-wide specimens were well within the test section and away from the shims.

Large stresses at the leading edge of the shims caused the surface layers to break prematurely. The stresses were elevated by the large gripping pressure

even though the ends of the shims were located outside the grips. The stresses at the edge of the shims would have been lower had the shims been longer, thinner, or tapered outside of the grips.

The broken surface layers did not appear to include the stiff hoop layers. Therefore, they carry too little load to have caused the lower than expected strengths.

Wrinkle-type defects.- A photograph revealing the details of the fracture near the outer surface of specimen 3-28 is shown in figure 9. The second hoop layer has several severe wrinkles near the center of the photograph. The fracture path from the broken surface layer passes through wrinkles.

For comparison, photographs of an edge of a tensile coupon and a coupon cut from the tag end of an actual FWC case (excess material at end) are shown in figure 10. Although the layups are different, notice that the hoop layers (light bands) of the FWC case are straight, but those of the tensile specimen are wavy. The inset shows an enlargement of one wrinkle that is so high the epoxy did not fill in beneath it. These wrinkles are part of a pattern of waviness that occurs throughout all the specimens in varying degrees. It was probably caused when the helical layers were wound over the hand-layed hoop layers, which had no pre-tension.

For carbon/carbon composites, Jones and Studdert (ref. 3) noted that wrinkle-free laminates are stronger than wrinkled laminates. The differences in strength were not given. However, in unpublished work of one of the present authors (Poe), two 16-ply-panels made of graphite/epoxy tape failed at remote wrinkles rather than at five-inch-long cuts at the center of the panels. The strengths were about half those of an uncut laminate, indicating that the stress concentration factor at the wrinkles was about two. A stress concentration factor of 1.6 would account for the lower than expected strengths in figure 6.

Load-stroke curves.- The load-stroke curves for the sixteen undamaged specimens with 1.0-, 1.3-, and 1.5-inch-wide test sections are shown in figure 11. The nonlinearity in the stroke curves is due primarily to movement within the grips. The curves increase monotonically except for three of the 1-inch-wide specimens in figure 11(a) where the load dropped momentarily (3-10, 3-28, and 3-30). Immediately after the drop in load, delaminations were observed near the inner surface of specimen 3-10 and the outer surface of specimen 3-28. The delamination in specimen 3-28 is visible between the second and third hoop layers from the outer surface in figure 9. These three specimens were the weakest of the six 1-inch-wide specimens. The load drops were likely to have been caused by partial failures that reduced the stiffnesses of the specimens.

The gripping failures (premature failures of the surface layers at the aluminum shims) were analyzed to determine if they could have caused the load drops. Removal of the helicals on the outside surface will reduce the stiffness less than 1 percent, and removal of the cloth and helicals on the inside surface less than 4 percent. The load drops in figure 11(a) correspond to stiffness changes of approximately 10 percent. Therefore, gripping failures could not have caused the load drops in figure 11(a). Moreover, the load did not always drop when the surface layers failed at the shims and vice versa. For example, the load applied to specimen 3-30 dropped momentarily even though the surface layers did not break at the shims, and the load applied to specimen 3-10 and the

1.5-inch-wide specimens did not drop momentarily even though the surface layers did break at the shims.

More than the helical layers on the surface must fail to cause the 10 percent drops in stiffness observed in figure 11(a). For example, removal of the outermost helicals down through the first, second, third, or fourth hoop layers inclusive will reduce the stiffness 5, 11, 18, or 24 percent, respectively. Removal of the innermost cloth up through the first or second double-hoop layer will reduce it 12 or 21 percent. (Recall that the thickness of the inner hoop layers is twice that of the outer hoop layers.) Thus, hoop layers must also fail to cause a 10 percent drop in stiffness. Therefore, it seems likely that wrinkled hoop layers broke prematurely and caused the momentary load drops in figure 11(a).

Stress-strain curves.- The load versus strain curves for five of the 1-inch-wide undamaged specimens are shown in figure 12. The clamping action caused the inside and outside surfaces of the specimens to be in tension and compression, respectively, regardless of the specimen position. Thus, the bending was probably due to some characteristic of the specimens and not the grips. The initial strain was largest on the inside surface, as large as 0.0015. The difference between the strains decreased slightly with increasing load as though the bending was coupled to the stretching. Because the laminate is asymmetrical, a realistic, though slight, flexibility of the grips would have permitted this type of bending. For the initial linear portion of the load versus strain curves, the average Young's modulus in the hoop direction, E_x , is 5.55 and 5.20 Msi on the inner and outer surfaces, respectively. These moduli are about 20 percent greater than the 4.44 Msi predicted by lamination theory for the case of no bending. The difference between the strain on the inner and outer surfaces is not nearly large enough to indicate that bending could have caused the low undamaged strengths noted previously. In fact, the larger moduli indicate that the strengths should have been larger than predicted.

At a hoop strain of 0.005 to 0.006 on the outside surface, the curves become nonlinear. At these hoop strains, the transverse strain in the helical layers is 0.0030 to 0.0035, probably large enough to cause cracking in the helical layers. The cloth material, which comprises the innermost layer, does not crack as readily as the helical layers, which comprise the outermost layers. Thus, the linear range of hoop strain on the inside surface is larger than that on the outside surface. The maximum hoop strain readings never exceeded 0.012. However, once the surface layers crack, the hoop strain readings may not represent the interior strains.

Notice that the signals of both strain gages on specimen 3-10 and the one on the inside surface of specimen 3-28 became chaotic at about 64 kips. The load applied to these specimens also dropped prematurely in figure 11(a) at the same time. The jumps in strains were probably caused by failure of the surface layers to which the strain gages were affixed. Thus, the wrinkled hoop layers that broke prematurely must have been near the surface as also indicated by the observed delaminations in specimens 3-10 and 3-28.

Previously (ref. 1), a 1-inch-wide undamaged specimen was loaded to failure with strain gages affixed to the edges as well as the inside and outside surfaces. However, the strain gage bridges were balanced at zero load after the

grips were clamped, not before the grips were clamped as in the present case. The strains on the edges were usually between those on the inside and outside surfaces. For the inside and outside gages, the results in reference 1 are consistent with those in figure 12 if the initial strains in figure 12 are removed.

Static Compliance Tests

The displacement of the spherical impactor has two components: overall flexure of the composite ring and local indentation. For a semi-infinite body that is homogeneous and isotropic, the local indentation is given by the Hertz law (ref. 4),

$$u_h = (P/n)^{2/3} \quad (1)$$

where

$$n = 4R_1^{1/2} / [3\pi(k_1 + k_2)]$$

$$k_1 = (1 - \nu_1^2) / (\pi E_1)$$

$$k_2 = (1 - \nu_2^2) / (\pi E_2)$$

and ν_1 , ν_2 , E_1 , and E_2 are the Poisson's ratio and Young's modulus of the sphere and half-space, respectively, and R_1 is the radius of the sphere.

The flexural component can be represented by a linear spring,

$$u_f = P/k_f \quad (2)$$

where k_f is the spring constant.

Values of k_f and n were calculated from the displacements measured during the static tests. For the empty ring, k_f was calculated from the displacement of the inner surface beneath the impactor, and n was calculated from the total displacement less the displacement of the inner surface beneath the impactor.

The results were $k_f = 29.0$ kips/in. and $n = 531$ kips/in.^{3/2}.

The total displacements of the filled ring were measured, but not those beneath the impactor. Thus, values of k_f and n could not be calculated from the displacements of the filled ring alone. Because the contact stresses decrease rapidly with distance from the contact point and the composite is very thick, the indentations for the filled and empty rings were assumed to be equal. Then k_f was calculated from the total displacements less the Hertzian indentation

calculated with equation (2) and $n = 531 \text{ kips/in.}^{3/2}$. The result was $k_f = 36.2 \text{ kips/in.}$

The value of k_f for the filled ring is only 25 percent greater than that for the empty ring. The inert propellant, which has a Young's modulus of 180 to 5,000 psi, depending on loading rate, contributed less to the stiffness than one would expect. Therefore, most of the load was carried around the composite ring in flexure rather than through the inert propellant. Also, the Hertzian indentation was only about 1/5 the flexural spring-type displacements.

Impact tests

Impact force.— Equations for impact behavior were derived in reference 4 using rigid body mechanics and elasto-static stiffnesses. They agreed with measurements for impacts of a small steel ball against a small, thin composite plate that was relatively massless. A spring-mass model in reference 5, which similarly assumes elasto-static stiffnesses, also agreed with the impact behavior of similar plates. However, the filled and empty rings are large and have masses of 89 and 635 lbm, respectively. It will be shown subsequently that the flexural stiffnesses of the filled and empty rings during impact were much greater than those measured in the static compliance tests. For that reason, the analyses in references 4 and 5, which use static stiffnesses, predict impact forces that are much too small for the filled and empty rings. A more exact dynamic analysis is beyond the scope of the present paper. However, equations like those in reference 4 can be used as a framework to qualitatively understand how the impact parameters affect the results for the filled and empty rings.

Assuming that two colliding bodies obey rigid body mechanics, one body is at rest, and that the displacements and forces follow the Hertz law, one can show (ref. 4) that the maximum impact force is

$$P = n^{2/5} \{5KE/[2(1 + m_1/m_2)]\}^{3/5} \quad (3)$$

and the impact duration is

$$t_o = 2.942^{-9/10} [n(1 + m_1/m_2)/5]^{-2/5} m_1^{1/2} (KE)^{-1/10} \quad (4)$$

where

$$KE = m_1 v_1^2 / 2$$

is the kinetic energy of the spherical impactor, m_1 and v_1 are the mass and velocity of the impactor, and m_2 is the mass of the composite ring.

For the linear flexural spring,

$$P = [2k_f KE / (1 + m_1/m_2)]^{1/2} \quad (5)$$

and

$$t_o = \pi m_1 / [k_f (1 + m_1/m_2)] \quad (6)$$

Some impact force signals from the strain gages are shown in figures 13 and 14. The high frequency oscillations are mostly ringing of the impactor. The magnitude of the Fourier coefficients of the accelerometer signal for positive frequencies are plotted in figure 15 for the filled and empty rings impacted by the 19.9 lbm impactor at 99.5 ft-lbf. The largest coefficients, which occur near zero frequency, correspond to the first mode response of the rings. Most of the other large coefficients occur near multiples of 4.34 kHz, the natural frequency of the impactor rod when struck on the end. Thus, the peak values of the oscillations probably do not represent an actual force between the impactor and target. Accordingly, the oscillations were treated as noise, and the maximum impact forces in tables I and II were determined from the impact force signal after the data were numerically smoothed. The coefficients for the filled and empty rings are very similar, also indicating that the high frequency oscillations are ringing in the impactor.

The duration of the impacts in figures 13 and 14 vary with kinetic energy and mass as predicted by equations (4) and (6). For example, in figure 13, the duration decreases only slightly with kinetic energy. Equations (4) and (6) predict little (-1/10 power) or no variation with kinetic energy. Also, in figure 14, the duration increases with mass to approximately the 0.63 power, which is between the 1/2 power in equation (4) and the proportionality in equation (6).

Notice in figures 13 and 14 that the 19.9 and 41.1 lbm impactors collided twice with the empty ring. Moreover, the second collision with the 41.1 lbm impactor had two peaks without breaking contact. It appears that an impactor with a mass slightly larger than 41.1 lbm would have remained in contact and only collided once. The impact force for the second impact increased with impactor mass, opposite to that for the first impact. The ratio of initial to subsequent impact forces was about 0.5 and 0.8 for the 19.9 and 41.1 lbm impactors, respectively. For these two masses, the impactors did not rebound (reverse motion) on the first collision and were caught in the way when the ring rebounded. The less massive impactors rebounded on the first collision and were out of the way when the ring rebounded. Consider the empty ring to be represented by a spring and mass. Recall that when a moving body collides with a body initially at rest, the moving body will be stopped if the masses are equal. If the mass of the moving body is less than that of the body at rest, the moving body will rebound or reverse direction and vice versa. Such was approximately the situation here. The 19.9 lbm impactor was nearly stopped, indicating that the effective mass of the empty ring was approximately 20 lbm.

To determine the effective masses of the rings, the negative ratios of initial velocities to rebound velocities (after first collision) are plotted against the ratio of impactor to ring masses in figure 16. (Multiple collisions occurred only for $m_1/m_2 = 0.224$ and 0.462 .) Each symbol represents the average value for a given kinetic energy. Nominal values of energy were used: 30

represents 27.8 and 30.3 ft-lbf; 50 represents 49.8, 51.4, 55.5, and 60.6 ft-lbf; 100 represents 99.5, 103, and 111 ft-lbf; and 200 represents 199 and 206 ft-lbf. The calculations were made with $m_2 = 89$ and 635 lbm for the empty and filled rings, respectively. The effective mass corresponds to zero rebound velocity. For the empty ring, the data indicate that the effective mass is about 1/4 the total mass or 22 lbm ($89/4$). For the filled ring, even the 41.1-lbm impactor rebounded without multiple collisions. Thus, the effective mass was greater than 41.1 lbm and can only be estimated by extrapolation.

The equation

$$-v_r/v_i = 1 - (4m_1/m_2)^{0.318} \quad (7)$$

was fit to all the data in figure 16 with a linear regression analysis. The factor 4 was assumed on the basis of the data for the empty ring. Equation (7) models the data for the filled and empty rings quite well. Therefore, the effective mass of the filled ring was also assumed to be 1/4 the total mass or 159 lbm. As it turns out, the masses of the impactors are so much smaller than 1/4 the mass of the filled ring that the accuracy of 1/4 is not critical in analyzing the data for the filled ring.

For $m_1/m_2 \leq 0.125$, the masses and rings collided only once and the negative velocity ratios in figure 16 are coefficients of restitution. When multiple collisions occur, the negative velocity ratio after the final collision, not the first, is the coefficient of restitution. For $m_1/m_2 \geq 0.224$, the average velocity ratios after the final collision (not shown in figure 16) were 0.50 and 0.55 for $m_1/m_2 = 0.224$ and 0.462, respectively. Therefore, the coefficients of restitution were near unity for very small m_1/m_2 , had a minimum value of about 0.2 for $m_1/m_2 = 0.125$, and increased to about 0.5 for $0.224 \leq m_1/m_2 \leq 0.462$. The decrease in coefficient of restitution with m_1/m_2 is mainly associated with the increase in energy stored in the moving ring and propellant, not damage to the composite.

The maximum values of the impact force are plotted against the modified kinetic energy of the impactor $KE/(1 + m_1/\bar{m}_2)$ in figure 17(a) and 17(b) for the filled and empty rings, respectively. The term \bar{m}_2 is the effective mass of the empty and filled rings, which was assumed equal to 22 and 159 lbm, respectively. The impact forces for the various impactor masses correlate quite well with $KE/(1 + m_1/\bar{m}_2)$. For the empty ring, the impact forces vary significantly with impactor mass for a given kinetic energy. See table II. The term $1 + m_1/\bar{m}_2$, which varies from 1.28 to 2.87, causes the data to coalesce in figure 17. For the filled ring, the impact forces vary little with impactor mass for a given impact energy. See table I. In this case, $1 + m_1/\bar{m}_2$ only varies from 1.04 to 1.26.

Also, equations (3) and (5) are plotted in figures 17(a) and 17(b) using the static stiffnesses $k_f = 29.0$ kips/in. and $n = 531$ kips/in.^{3/2} for the empty ring and $k_f = 36.2$ kips/in. and $n = 531$ kips/in.^{3/2} for the filled ring. Equation (3) for the Hertz law overestimates the impact forces and equation (5) for the flexural spring greatly underestimates the impact forces.

One can show as follows that equations (3) and (5) should both overestimate the impact forces. The total displacement of the impacter during contact is the sum of u_h and u_f in equations (1) and (2). Thus, the springs for the Hertz law and flexure are in series. For convenience, assume the Hertzian spring is a linear spring with a stiffness k_h . (This assumption greatly simplifies the analysis but does not compromise the result.) The equivalent stiffness for two linear springs in series is

$$k_{eq} = k_f / (1 + k_f / k_h)$$

or

$$k_{eq} = k_h / (1 + k_h / k_f)$$

Therefore,

$$k_f = k_{eq} (1 + k_f / k_h)$$

and

$$k_f > k_{eq}$$

Similarly,

$$k_h > k_{eq}$$

If equation (5) with $k_f = k_{eq}$ gives forces equal to the test data, then equation (5) with $k_f > k_{eq}$ or $k_h > k_{eq}$ will give forces greater than the test data. In order for equation (5) to give values of impact force greater than the test data, k_f must be more than four times the values measured in the static compliance tests. Because of the transient nature of the impact, the static stiffness or first mode greatly overestimates the flexural displacements during impact. (The time for the disturbance to travel around the rings was large compared to the duration of the impact.) On the other hand, equation (3) for the Hertz law probably gives a fairly good estimate of the indentation during impact because of the very local stress field that is associated with the Hertz law. As will be shown subsequently, the contact diameter is estimated quite well by the Hertz law. Viscoelasticity of the epoxy matrix may also cause the static deformations to be a little larger than those that occur during impact. The local deformation given by the Hertz law depends much more on the matrix

properties than the flexural deformation. Thus, the local deformation should be affected much more by viscoelasticity than the flexural deformation.

The impact forces in figures 17(a) and 17(b) for the filled and empty rings are plotted together in figure 18. The data coincide indicating that the dynamic stiffnesses for the filled and empty rings are approximately equal. Recall that the static stiffnesses only differed by 25 percent. Thus, the effect of the inert propellant was to increase the inertia of the composite ring but not the stiffness. The symbols were filled in figure 18 to indicate when impacters made visible craters. The 1/2-inch-radius impacter made visible surface craters in the filled ring for impact forces as small as 16.9 kips and in the empty ring as small as 20.4 kips. Below the threshold, the impacter only made a slight indentation and gave luster or sheen to the surface -- not a very detectable mark. The transition from crater to no crater was somewhat vague as evidenced by the variability in impact force to cause a crater.

The equation

$$P = 1,810[KE/(1 + m_1/\bar{m}_2)]^{0.516} \quad (9)$$

which has the same form as equations (3) and (5) for the Hertz law and a linear spring, was also plotted in figure 18. A linear regression analysis, excluding the data with craters, was used to determine the constants 1,810 and 0.516. Equation (9) fits the data without craters quite well. When craters were made, the impact forces were smaller than predicted, indicating that the damage had a softening effect. The exponent 0.516 is between 3/5 and 1/2, the exponents in equations (3) and (5), respectively.

It is believed that equation (9) can be used to predict the impact force to an actual FWC. The value of effective mass \bar{m}_2 in equation (9) should be approximately the same for an FWC and the 30-inch-diameter ring. For an empty ring, the effective mass was 22 lbm. However, for the ring filled with inert propellant, recall that the impacters were not massive enough to exactly determine the effective mass. Instead, it was assumed to be 1/4 of the total mass, like the empty ring, or 159 lbm. For impacter masses no greater than 41 lbm, 159 lbm should be reasonably valid for an FWC filled with propellant, much as for the ring. But for impacter masses much greater than 41 lbm, the use of 159 lbm may not give good predictions.

For individual specimens lying on inert propellant and impacted by the 19.9-lbm impacter (ref. 1), the impact forces were about half those for the filled ring. They increased in proportion to $954(KE)^{0.504}$ compared to equation (9), which gives $1,920(KE)^{0.516}$ for the 19.9-lbm impacter. In fact, the impact forces for the specimens lying on propellant were less than those for the empty ring, where they increased in proportion to $1,300(KE)^{0.516}$ for the 19.9 lbm impacter. For the filled ring, the propellant acted like a mass increasing the inertia of the composite ring. However, for the individual specimens lying on propellant, the propellant acted like a spring that was more compliant than the composite ring.

Hercules Inc. impacted four quarter-scale cases with 30-lbm impacters: one each in the membrane and transition regions with blunt and sharp impacters. The thickness, diameter, and length of the quarter-scale case were one-fourth those of a full-sized FWC. The proportion of hoop and helical layers in the quarter-scale case was the same as that in the full-sized FWC. The quarter-scale cases contained a tightly fitting diametric post and was impacted over one end of the post to make the impact "hard" like an actual FWC containing propellant. For the quarter-scale case impacted in the membrane region with a 1/2-inch-radius impacter at a kinetic energy of 50 ft-lbf, the impact force was 18.50 kips. (The impacter mass and kinetic energy were incorrectly reported in reference 1 as 51.0 lbm and 76.42 ft-lbf.) On the other hand, impact of another quarter-scale case in the transition region (near the end where the laminate is in transition from membrane layup to joint layup) with the 1/2-inch-radius impacter resulted in 16 percent less impact force with 50 percent more kinetic energy, 15.63 kips for 75 ft-lbf. Thus, the impact to the membrane region was much "harder" than that to the transition region. It is not obvious that the difference between the laminates in the membrane and transition regions can account for this difference. Also, the impact force signals were very different. The signal for the impact to the membrane region indicates that the impacter collided twice with the case, much as the empty ring impacted with the 19.9- and 41.1-lbm impacters. However, the signal indicates that the impacter only collided once for the transition region, as well as for the two tests with the sharp impacter. Therefore, the test results for the quarter-scale case impacted in the membrane with the 1/2-inch-radius impacter are suspect.

From equation (9), the impact forces for the filled ring impacted with a 30-lbm impacter at 50 and 75 ft-lbf are 12.5 and 15.4 kips, respectively. Recall that they were 18.50 and 15.63 kips, respectively, for the quarter-scale cases. Therefore, the impact forces for the filled ring and the quarter-scale cases are approximately equal for the impact to the transition region (75 ft-lbf), but not for the impact to the membrane region (50 ft-lbf).

Impact damage.- Love's solution for stresses in a semi-infinite body produced by hemispherical pressure on part of the boundary (ref. 6) can be used to predict the depth of impact damage in terms of impact force. This solution is for a body that is homogeneous and isotropic but should be accurate, at least qualitatively, when the contact diameter is large compared to layer thickness. Anisotropic finite element solutions give lower stresses than the isotropic theory but of the same character (ref. 4). No tension stresses exist beneath the contact area. The compression stress in the plane of the fibers is a maximum at the center of the contact surface and decreases rapidly with distance from the surface. The maximum value is $1/2 + \nu$ times the average contact pressure. As will be shown subsequently, the average contact pressure for the impacts without crater type damage varied from 70 to 100 ksi. Consequently, the compression stresses did not exceed 100 ksi, not high enough to predict the deep damage that was observed. Thus, the fiber damage is not likely associated with normal stresses. For this reason, attention was given to shear stresses.

The contours of principal shear stress from the solution are plotted in figure 19. The coordinates z and ρ are normalized by the contact radius. Contours are plotted for different ratios of average contact pressure to allowable shear stress. The average contact pressure p_c is the impact force

divided by the contact area or $p_c = P/(\pi D^2/4)$. The maximum value of the hemispherical pressure is 1.5 times the average value and occurs at $\rho = 0$. Assuming failure occurs at a critical value of principal shear stress, the contours of principal shear stress represent damage contours. The depth and width of the damage contours are plotted against the contact pressure in figure 20. Damage initiates below the surface at $\rho = 0$ and $2z/D = 0.47$ when the contact pressure is approximately 1.61 times the allowable shear stress. As the pressure increases, the damage spreads in all directions and reaches the surface at a pressure equal to approximately 5.0 times the allowable shear stress. After damage initiates, the width increases rapidly with pressure until it is about equal to the contact diameter. Then it increases with pressure very slowly. The depth of damage is always larger than the half-width of damage.

The curves in figure 20 can be used to predict the depth of impact damage if the allowable shear stress, the contact radius, and the contact pressure are known. For the Hertz law (ref. 4), the contact diameter is

$$D = 2R_1^{1/2}(P/n)^{1/3} \quad (10)$$

The contact diameter measured with the carbon paper is plotted against impact force in figure 21. Different symbols were used to indicate when the impacters made craters. (In the empty ring, the contact area was not measured when the impacters made craters.) The paper was obliterated in the contact area when the impacters made craters, and the outline of the area was somewhat ragged. Thus, the dispersion is greater when impacters made craters. Equation (10) was fit to the data without permanent craters and also plotted in figure 21. The regression analysis gave $n = 408 \text{ kips/in.}^{3/2}$. Equation (10) models the effect of impact force very well except when the impacters made craters. Then, the contact diameter was considerably above the curve. The Hertz law does not account for the crater type damage.

Eliminating the contact diameter in equation (10) with $D = [4P/(\pi p_c)]^{1/2}$ and solving for the average contact pressure p_c ,

$$p_c = n(P/n)^{1/3}/(\pi R_1) \quad (11)$$

Thus, both contact diameter and pressure increase in proportion to impact force to the 1/3 power.

The impact forces divided by the circular contact area $\pi D^2/4$ and equation (11) with $n = 408 \text{ kips/in.}^{3/2}$ are plotted against impact force in figure 22. Different symbols were used when impacters made craters. Without craters, the pressures are 70 to 100 ksi. Recall that the peak value of the hemispherical pressure in Love's solution is 50 percent greater than the average value. When craters were made, the contact diameters were so large that the pressures dropped about 40 percent.

Recall that the static compliance tests gave a value of $n = 531$ kips/in.^{3/2}, which is only 30 percent greater than the value of $n = 408$ kips/in.^{3/2} from the regression analysis. Thus, the Hertz law appears to be fairly accurate for the impacts.

The value of n can also be calculated from the elastic constants of the composite and spherical indenter using equation (1). However, equation (1) was derived for isotropic materials and there is some uncertainty about what to use for E_2 . Because most of the deformation is transverse to the laminate, the Young's modulus for the laminae E_{22} is probably a good representation of E_2 . Unfortunately, values of E_{22} for the hoop and helical layers were reported to be quite different, 0.9272 and 0.2781 Msi, respectively. Assuming $E_1 = 30$ Msi (steel), $\nu_1 = \nu_2 = 0.3$, and $R_1 = 0.5$ inches, equation (1) gives $n = 932$ and 285 kips/in.^{3/2} for $E_2 = 0.9272$ and 0.2781 Msi, respectively. These values bound $n = 531$ and 408 kips/in.^{3/2}, which were determined from the static compliance measurements and the contact diameter measurements. Therefore, E_{22} is a good estimate for E_2 . Conversely, using equation (1) and the average of 531 and 408 kips/in.^{3/2} gives an effective E_2 of 0.4532 Msi.

Using equations (10) and (11) and the curve for damage depth in figure 20, the depth of damage (distance to innermost damage) was calculated and plotted in figure 23 for shear stress allowables of 15 and 45 ksi. The 15 ksi allowable corresponds to the onset of matrix failure. It is typical for the shear strength of unidirectional graphite/epoxy. The 45 ksi allowable represents failure of matrix and fibers. The locations of hoop layers are indicated on the ordinate. The impact force threshold (smallest impact force that causes damage) is predicted to increase in proportion to the shear stress allowable to the one-third power. For fiber damage (45 ksi), the threshold is 6.67 kips. However, for matrix damage (15 ksi), the threshold is virtually zero, only 0.25 kips. The depth at which the damage initiates is predicted to increase in proportion to the shear stress allowable. Fiber damage is predicted to initiate in the outermost hoop layer and matrix damage in the helical layers closer to the outer surface.

The depths of impact damage in the radiographs are also plotted in figure 23. Different symbols were used to indicate when the impacters made craters. The damage depths were very similar for the filled and empty rings. The damage was not visible for impact forces less than 9 kips. The damage was not always visible for impact forces between 9 and 20 kips. However, it was visible whenever impacters made craters. In general, damage depth increased with impact force above 9 kips and did not extend below the second hoop layer.

If the dye penetrated to the innermost matrix damage, the depth of damage in the radiographs should correspond to the predicted curve for matrix damage. However, it does not; the depths in the radiographs correspond more to the predicted curve for fiber damage. Actually they are a little less than the curve for fiber damage. Radiographs were made of an impacted specimen (18.3 kip

impact force) before and after a small hole was drilled deep into the impact site (ref. 1). There was no visible surface damage. The radiograph made before the hole was drilled also did not reveal damage. However, the radiograph made afterward did. Therefore, the radiographs do not reveal all the damage because the dye apparently cannot penetrate the relatively undamaged surface layers. Also, the damage depths are probably overpredicted somewhat because isotropic theory gave larger stresses than anisotropic theory (ref. 4).

The 45 ksi shear stress allowable was obtained by crushing circular coupons or disks that were cut from one of the rings. The disks were made by drilling normal to the laminate with a core drill. The diameters of the disks were 1, 1.5, and 2 inches. Several specimens with each diameter were tested by applying uniform compressive stresses to the inner and outer surfaces. The average normal compressive stress at failure was 88.6 ksi. The strength varied little with specimen width. The failure surfaces intersected the free edge forming a 45° wedge, typical of shear. For uniform pressure applied to a circular area of the boundary of a semi-infinite solid that is isotropic and homogeneous (ref. 6), the largest principal shear stresses occur beneath the center of the circular area. On the surface, the ratio of principal shear stress to pressure is equal to $1/2 - \nu$. The ratio increases with distance into the laminate to a maximum value and then decreases, much like the contours in figure 19 for a hemispherical distribution of pressure. For a value of $\nu = 0.3$, the maximum value of the principal shear stress is 0.55 times the pressure and occurs at a depth equal to 0.59 times the radius of the circular area. At the free edges, where the stress state is uniaxial, the principal shear stress is $1/2$ times the pressure. Thus, it seemed reasonable to assume that the principal shear stress at failure is $1/2$ the pressure, or approximately 45 ksi ($1/2$ of 88.6).

Residual Strength Tests

Specimens with surface cuts were also tested (refs 1 and 7). The specimens were observed to fail as two parts or in two stages. First, the cut sublaminates failed transversely and delaminated from the remainder of the laminate. The delamination initiated near the bottom of the surface cut separating the failed sublaminates with the surface cut from the unfailed remainder, which was essentially uncut. Then, with additional load, the remainder failed. For shallow surface cuts, the first failure overloaded the remainder of the laminate causing what appeared to be simultaneous failures. The stress at which the cut sublaminates failed decreased with increasing surface cut size according to linear elastic fracture mechanics, and the strength of the remainder varied inversely with its thickness, much as an uncut laminate. (Similar results were reported in reference 8 for a 0.4-inch-thick quasi-isotropic T300/5208 laminate.) Failures of the cut sublaminates and the remainder were referred to as first- and remaining-ligament failures, respectively.

Impacted specimens failed similarly indicating that impact damage and surface cuts were equivalent for this laminate.

Radiographs made after loading to first-ligament failure.— Radiographs of impacted specimens made before and after loading to first-ligament failure are shown in figures 24 and 25 for the filled and empty rings, respectively. They

represent each combination of kinetic energy and impactor mass. A top and a side view are shown for each condition. In the radiographs, the dark narrow bands are the hoop layers and the light bands are the helical layers. (The light and dark bands are transposed in the photographs, wherein the dark bands are the helical layers and the light bands are the hoop layers.) The delaminations are not confined to a single interface or plane but meander among layer interfaces. Thus, the delaminations do not appear as narrow lines in the radiographs of the sides but as wide dark bands. The innermost path of the delaminations seemed to lie at an interface of hoop and helical layers. Thus, the delamination depths were recorded in tables I and II as distances to hoop layers. It is important for the reader to understand that these delaminations were caused by the loading, not the impacts. The impacts themselves did not cause delaminations.

For 7 of the 21 specimens, the radiographs in figures 24 and 25 also revealed that the innermost surface layers had broken prematurely at the shims, much like the undamaged specimens. See for example figure 25(c). The failures were approximately evenly divided between the 1.3- and 1.5-inch-wide specimens, 4 out of 11 and 3 out of 10, respectively. Postmortem examination revealed that the innermost surface layers of many other specimens broke at the edge of a shim. A note was made in tables I and II for these specimens. It happened to 66 percent of all the impacted specimens, as often to the 1.3-inch-wide specimens as to the 1.5-inch-wide specimens. It is puzzling that none of the surface layers failed at the edge of the shims for the five 1.3-inch-wide undamaged specimens in figure 8(b), and that none of the outermost surface layers of the impacted specimens broke at the shims as did those of two of the undamaged specimens in figure 8(c).

Load-stroke records.- The load-stroke records for all the specimens with impact damage are presented in figures 26 and 27 for the filled and empty rings, respectively. The records for replicate tests are shown in the same graph for ease of comparison. Those for the specimens that were statically indented (1-14 and 5-12) were included in figures 26(f) and 27(j) where the impact forces were nearest to the static forces. Two load-stroke curves are shown for those specimens that were unloaded, x-rayed, and reloaded after first-ligament failure. The curves were expected to have one or two peaks, depending on whether or not failure of the first ligament overloaded the remaining ligament. However, for 40 percent of the specimens, the curves had more than two peaks. Like the undamaged specimens in figure 11(a), the extra peaks may have been caused by the wrinkles. However, as will be shown subsequently, the extra peaks may also be caused by impact damage.

Strengths.- The first load peak and the largest load peak were used to calculate the stresses in tables I and II for failure of the first and remaining ligaments. When the ligaments failed simultaneously and only one peak occurred, the failing stress was recorded as that of the first ligament.

The stresses to fail the first and remaining ligaments were divided by the mean undamaged strength of 50.1 ksi and plotted in figures 28 and 29, respectively. For surface cuts, the fracture toughness and the undamaged strengths (ref. 1) were apparently reduced in the same proportion by the wrinkles (or whatever else caused the lower than expected strengths). Thus, the strength ratios should have been unaffected. Because impact damage seemed equivalent to a surface cut (ref. 1), the strength ratios of the impacted

specimens should also be unaffected by the wrinkles. Thus, it is believed that the ratios can be directly compared to the actual FWC laminate.

When the first and remaining ligaments failed simultaneously, the strength was plotted in figures 28 and 29. Thus, the failing stresses in figure 29 are also the maximum or ultimate strengths of all the specimens. Different symbols were used for the empty and filled rings, and the symbols were filled when the impacters made craters. The stresses for first-ligament failure decrease with increasing impact force. On the other hand, the stresses for remaining-ligament failure appear to be independent of impact force and whether or not the impacters made craters. It is very important for the reader to realize that the stress to fail the remaining ligament was calculated with total thickness (gross stress) -- not the thickness of the remaining ligament (net stress). One would expect the net stress on the remaining ligament at failure to be nearly constant but not the gross stress. For the largest impact forces, the stresses for first-ligament failure are as low as 50 percent of the mean undamaged strength. On the other hand, the stresses for remaining-ligament failure are no lower than 75 percent of the mean undamaged strength. The lowest stresses for first- and remaining-ligament failures without visible craters is 63 and 78 percent of the mean undamaged strength, respectively. Also, the failing stresses do not drop dramatically as the impact-force threshold for causing visible craters is exceeded. On the basis of appearance, one would expect the failing stresses with visible craters to be much lower than those without craters.

The failing stresses of the impacted and undamaged specimens overlap considerably. For several specimens, in fact, the stress to fail the remaining ligament is greater than the mean undamaged strength. Also, the failing stresses for specimens from the filled ring are typically 5 to 10 percent higher than those for specimens from the empty ring. It is believed that this difference is caused by material or testing variations and not by the inert propellant.

The impact force threshold for nonvisible damage is indicated in figures 28 and 29 by the vertical line at 16.9 kips. The 1/2-inch-radius impacter never made visible surface craters in the filled ring for impact forces below 16.9 kips and in the empty ring below 20.4 kips. As noted previously, the transition from no crater to crater was somewhat vague. On the other hand, impact damage was usually visible in radiographs for impacts above 9 kips. See figure 23. However, one would not expect to search for impact damage in the field by x-raying large areas such as the walls of the FWC's. In the preliminary tests (ref. 1), the 1/4-inch-radius hemisphere, 90° corner, and 1/4-inch-diameter rod made more visible damage than the 1/2-inch-radius hemisphere. More tests with filled and empty rings and these more damaging indenters are underway.

The failing stresses for the two statically indented specimens were also plotted in figures 28 and 29. They fall among those for the impacted specimens from the empty ring indicating that the static and impact tests were equivalent. Others have suggested that statically applied forces can be used to represent low-velocity impacts, for example references 4 and 9.

The scatter among the strengths of specimens impacted under like conditions is shown in figure 30 where the cumulative frequency is plotted against coefficients of variation for first-ligament and ultimate strengths. (The

ultimate strength is the maximum of the first- and remaining-ligament failing stresses.) The first-ligament strengths are dispersed significantly more than the ultimate strengths. The mean coefficient of variation is 0.0466 for ultimate strengths and 0.0705 for first-ligament strengths. Both are smaller than the coefficient of variation (0.0805) for the undamaged specimens in table III. Strengths of specimens with notches or damage usually have less dispersion than those of unnotched or undamaged specimens.

The failing stress ratios in figures 28 and 29 were replotted in figure 31 differentiating only between first- and remaining-ligament strengths. The average values for a given impactor mass and kinetic energy, rather than individual values, were plotted to clarify the trends. The minimum factor of safety for the membrane of the FWC is 1.4. The stress ratios that correspond to the maximum expected operating pressure (MEOP) and the minimum factor of safety are also plotted. Typically, the stresses to fail the remaining ligament in figure 31 correspond to a factors of safety greater than 1.4. However, the stresses to fail the first ligament correspond to factors of safety less than 1.4 for impact forces above 12 kips. At 16.9 kips, the threshold for nonvisible damage, the factor of safety is about 1.3 and, at 21 kips, almost as low as 1.0.

The strength ratios are for a uniaxial state of stress and the factors of safety correspond to a two-to-one biaxial state of stress. Daniel (ref. 10) found that the strength of $(0/\pm 45/90)_S$ graphite/epoxy with a hole was about 23 percent less for uniaxial tension loads than for a one-to-one biaxial stress state. On the other hand, Daniel (ref. 11) found that the strength of $(0_2/\pm 45)_S$ graphite/epoxy with a hole was about 19 percent more for a uniaxial stress state than for a two-to-one biaxial stress state, which is like the stress state in the FWC. Unfortunately, laminate thickness also affects notched strength. For through-the-thickness cuts, the notched strength of $(0/\pm 45/90)_S$ decreases as much as 25 percent with thickness and that of $(0_2/\pm 45)_S$ increases as much as 18 percent with thickness (ref. 12). Thus, the effects of biaxial stress in Daniel's tests might be offset by scaling up the thickness. Also, the FWC laminate is approximately $0/(\pm 60)_2$, which is not like either of Daniel's layups. It is believed that the stress state effect in Daniel's tests is related to premature cracking and delaminating at the hole. Cracking and delaminating should be much less in the thick FWC laminate than in the 8 and 6 ply laminates of Daniel. Therefore, it is believed that the effect of stress state on the FWC laminate is small.

For the impacted quarter-scale case, the burst pressure and impact force were reported as 1371 psi and 18.5 kips, respectively. The burst pressure for the impacted case was divided by the average burst pressure of three cases without damage (1626 psi) and plotted in figure 31. The burst pressure ratio is somewhat above the strength ratios for first-ligament failure but agrees with the ratios for remaining-ligament. There was no evidence from strain gages nor acoustic emissions that the quarter-scale case failed as two parts. Therefore, it is not obvious how to compare the quarter-scale and tension tests.

The following fracture mechanics analysis gives insight into how to compare the tests. The strength for a full-thickness and a quarter-thickness laminate with surface cuts is plotted against surface-cut depth in figure 32. The curves

for first-ligament failure were calculated with a surface flaw analysis (ref. 1) and a predicted fracture toughness of 27.3 ksi/in. This value of fracture toughness accurately predicted strengths of specimens with surface cuts deeper than 0.2 inch. The predicted aspect ratio (half-width to depth) of impact damage is approximately 0.8. See figure 20. Therefore, the depth of the surface cut was assumed to be 0.8 times the half-length. For convenience, the laminates were assumed to be very wide compared to the thickness. The stair-stepped curves for remaining-ligament failure were calculated by multiplying Young's modulus for the remaining ligament by the failing strain of the laminate (ref. 1). Young's modulus was calculated with lamination theory after removing groups of helical and hoop layers from the surface down to the bottom of the cut. The largest strength drops are caused by removal of the stiff hoop layers and the smallest by removal of the more compliant helical layers. The curve is not straight in the overall sense because the hoop layers are not distributed uniformly. More hoop layers are located near the inner surface than the outer surface causing the curve to be convex upward. The curve for the quarter-thickness laminate was estimated by multiplying the abscissa of the full-thickness curve by one fourth. In actual tests, stresses to fail the remaining ligament were somewhat less than the predicted curve (ref. 1). Nevertheless, these curves are sufficiently accurate for this exercise, which is more qualitative than quantitative.

For the full-thickness laminate, the remaining-ligament strengths in figure 32 are greater than the first-ligament strengths when cuts are deeper than 0.2 inches. However, for the quarter-thickness laminate, the first-ligament strengths are greater than the remaining-ligament strengths for all cut depths. Therefore, one would expect the ligaments to fail simultaneously in the quarter-scale laminate but not in the full-thickness laminate when damage is deeper than 0.2 inches. Also, for impact damage of a given depth, one would expect the quarter-thickness laminate to have a strength less than or equal to the first-ligament strength of the full-thickness laminate, which was not the case in figure 31. However, as noted previously, the 18.50-kip impact force for the quarter-scale case is suspect. Recall that the 18.50-kip force was associated with 50 ft-lbf of energy; whereas, for the transition region, a 15.63-kip force resulted from an impact with 75 ft-lbf of energy. Assuming that the impact force is proportional to the square root of the kinetic energy, the impact force in the transition region for 50 ft-lbf would be $15.63\sqrt{(50/75)}$ or 12.76 kips. It does not seem that the impact force should be different for the membrane and transition regions when both cases contained the same diametric post. If the pressure ratio were replotted in figure 31 with an impact force of 12.76 kips rather than 18.5 kips, it would be approximately equal to the stress ratios for first-ligament failure, and the quarter-scale and tension tests would be in agreement.

It has not been established whether or not failure of the first ligament constitutes failure of the structure. If not, figure 31 indicates that the FWC has an adequate margin of safety for nonvisible damage. However, if the accompanying delamination spreads over most of the case as it spread throughout the tensile specimens, first-ligament failure would constitute failure of the case on the basis of the current accept/reject criteria for delaminations. Then, the FWC does not have an adequate margin of safety for non visible damage.

Equivalent cut depth.- One can infer the thickness of the remaining ligament and hence the depth of an equivalent surface cut from the strength of

the remaining ligament. The stair-stepped curve in figure 32 was found to predict remaining-ligament strengths for surface cuts that were somewhat larger than test values (ref. 1). Therefore, the following equation, which was fit to the surface cut data, was used to calculate equivalent surface cut depth from remaining-ligament strength S_c .

$$a = (S_c/30,100)^{-1/0.278} \quad (12)$$

The equivalent surface cut depths were calculated for all specimens that failed as two parts. The equivalent depths were recorded in tables I and II and plotted against impact force in figure 33. The large exponent in equation (12) would greatly amplify the scatter in strengths among like specimens. Thus, the average values for a given impactor mass and kinetic energy, rather than individual values, were plotted to clarify the trends. The location of the hoop layers are shown on the ordinate, and the symbols were filled when the impacters made craters. Also, the maximum damage depths predicted with shear allowables of 15 and 45 ksi (matrix and fiber damage, respectively) were plotted for comparison. The equivalent depths are between those predicted for fiber and matrix failure. The equivalent cut depths are more independent of impact force than the predicted curves so that the equivalent cut depths agree best with the fiber-failure curve for large impact forces.

The average depths of impact damage in the radiographs made before loading are also plotted in figure 33 for comparison. The radiographs reveal much less impact damage than predicted and implied by the remaining-ligament strengths.

Delamination depths after loading to first-ligament failure.- For $[0/\pm 45/90]_{10s}$ T300/5208 laminates with surface cuts, the delamination that accompanied first-ligament failure developed at the bottom of the cut (ref. 8). However, for surface cuts in the FWC laminate, the delamination was not always at the bottom (private communication from Dr. D. H. Morris, Virginia Polytechnic Institute and State University, Blacksburg, Virginia). It was at the interface of hoop and helical layers that was nearest the bottom of the surface cut. For this reason, the delamination depths could differ from the surface cut depths by as much as half the thickness of a group of helical layers, which is 0.056 inch for the $(\pm 56.5)_2$ double helical layers near the outer surface. (In the T300/5208 laminate, the delamination could also have been at the interface of the $\pm 45^\circ$ and 0° layers nearest the bottom of the surface cut. However, the difference probably would not have been noticed because only about 0.016 inch separates the 0° plies.)

The depths of delaminations in the radiographs in figures 24 and 25 were measured and plotted against impact force in figure 34. They were also recorded in tables I and II. Recall that, in all but one instance, the radiographs were made of only one specimen with a given impactor mass and kinetic energy. Thus, the values plotted in figure 34 are for individual specimens, not averages. The data in figure 33 were also replotted for comparison. If impact damage is equivalent to a surface cut, one would expect the delamination depths to differ from the depths of impact damage by no more than half the thickness of a group of helical layers. The delaminations depths were generally in agreement with

the equivalent surface cut depths but were much deeper than the damage depths measured in the radiographs made before loading.

Actual impact damage to the fibers was also determined by destructive examination. A specimen lying on fuel was impacted with the 1/2-inch-radius impactor. The kinetic energy was 369 ft-lbf and the impact force was 12.2 kips. A 1-inch by 1-inch coupon of full thickness was cut from the impact site, and the layers were separated by pyrolysis (300° F for 90 minutes). Then, the individual layers were examined with an optical microscope and a scanning electron microscope for broken fibers. The layers from the surface through the second helical layer below the first hoop layer, inclusively, contained obviously broken fibers. Two photographs of the deepest layer with damage, which is 0.14 inches from the surface, are shown in figure 35. They were made in the scanning electron microscope with 13X and 280X magnification. A 0.2-inch-long "crack" (locus of fiber breaks) can be seen in the 13X photograph. The "crack" was directly below the impact site and oriented normal to the fibers. The "cracks" in layers above this layer were similar, and all the layers below this layer were largely free of "cracks." The "cracks" in each layer were oriented normal to the fibers. Thus, they did not lie in a single plane like a surface cut. The region of the "crack" covered by the 280X photograph is outlined by the rectangle drawn on the 13X photograph. The individual fiber breaks can be seen in the 280X photograph. The broken fibers do not have the appearance of fibers that have failed in a compression field by shear kinking.

The depth of the "cracked" layer in figure 35 was also plotted in figure 34 for the corresponding impact force. Although this layer is much deeper than the damage revealed in the radiographs, it is only half as deep as the equivalent surface cuts and delaminations. However, it is almost as deep as the predicted curve for fiber failure (45 ksi). Perhaps fibers below the "cracked" layer in figure 35 were weakened but not visibly broken in the deplied layers. Elber (ref. 9) found evidence to this effect. He removed fiber bundles from the impact site of a thin graphite/epoxy laminate and loaded them to failure. The strengths of some bundles were 30 to 50 percent of the undamaged strength without a corresponding number of visibly broken fibers (private communication from Dr. Elber, NASA, Langley Research Center, Hampton, Virginia).

The behavior of other specimens, which were impacted with the 1/4-inch-radius hemisphere and 90° corner, is also consistent with the existence of weakened fibers below the broken fibers. Observations revealed that a delamination appeared in the first or second group of helical layers with the first load peak, and additional delaminations appeared in deeper groups of helical layers with the additional load peaks. The following scenario based on weakened fibers is consistent with these observations: the ligament with broken fibers failed and delaminated without overloading the remaining ligament; after some increase in load, the weakened fibers in the remaining ligament failed, causing the outer part of the remaining ligament to fail and delaminate, much like the first ligament; and finally, after some additional increase in load, the inner part of the remaining ligament failed. Thus, the weakened fibers reduced the remaining-ligament strength and made the equivalent cut depth greater than the depth of the "crack" in figure 35. Load-stroke curves for the specimens with surface cuts (ref. 7) did not have extra load peaks (private communication from Dr. C. E. Harris, Texas A&M University, College Station,

Texas). The specimens with surface cuts also contained the wrinkles, but they did not have weakened fibers below the cut. Therefore, weakened fibers were more likely than wrinkles to have caused the extra load peaks for the impacted specimens.

The predicted curves for shear allowables of 15 and 45 ksi in figure 34 represented matrix and fiber failure, respectively. An intermediate allowable would be associated with fibers that are weakened but not broken. Accordingly, a curve was predicted and plotted in figure 34 for an allowable of 35 ksi. This curve passes through the approximate median of the equivalent cut depths and impact forces.

CONCLUSIONS

A special 30-inch-diameter cylinder, 1.4-inches thick, was filament wound to represent the membrane of an aft segment of the graphite/epoxy solid rocket motor for the space shuttle. The cylinder was cut into 12-inch-long rings. Two of the rings were impacted with 1/2-inch-radius impacters. One of the rings was filled with inert propellant and one was empty. The masses of the impacters varied from 6.1 to 41.1 lbm and the kinetic energies from 30 to 330 ft-lbf. Two-inch-wide specimens were cut out of the two rings and uniaxially loaded to failure in tension. The center of each specimen coincided with an impact site. Each specimen was x-rayed after impact to determine the amount of impact damage. Moreover, one specimen of each combination of impacter mass and kinetic energy was x-rayed immediately after loading to the first partial failure. Also, one impacted specimen was destructively examined (deplied by pyrolysis) to determine the extent of actual broken fibers. The results indicate the following:

1. The inert propellant increased the inertia of the ring much more than its stiffness.
2. The impact force varied with kinetic energy and mass as predicted with rigid body mechanics and the Hertz law. For these tests, impact forces ranged from 8 to 22 kips. The Hertz law gave reasonably correct local deformations, contact diameters, and contact pressures. However, the impact force predicted with rigid body mechanics using the static stiffness of the rings was much too small. The rings were effectively more stiff in impact than in static loading.
3. Except for very shallow damage, the impacted specimens failed as two parts when loaded: first the outermost layers of the laminate containing the impact damage and then, with additional load, the remaining part. The two parts delaminated when the first failure occurred. For very shallow damage, the two parts failed simultaneously. The stresses at which the two parts failed correlated well with impact force. The stress to fail the first ligament decreased with impact force much more than the stress to fail the remaining ligament. For the largest impact forces, the stresses to fail the first and remaining ligaments were as low as 50 and 75 percent of the mean undamaged strengths, respectively. These stresses correspond to factors of safety for the FWC of about 1.0 and 1.4.

4. The impact force threshold for nonvisible damage was 16.9 kips. Above 16.9 kips, the impacts usually caused visible surface craters. The radiographs sometimes revealed damage for impact forces as low as 9 kips. However, the radiographs did not reveal the full depth of damage for any impact force. Impact damage inferred from remaining-ligament strength and delamination depth was considerably deeper, especially for the smallest impact forces. For nonvisible damage, the stresses to fail the first and remaining ligaments were as low as 63 and 78 percent of the mean undamaged strengths, respectively. These stresses correspond to factors of safety of about 1.3 and 1.4.
5. The depth of broken fibers was reasonably well predicted using Love's solution for pressure applied on part of the boundary of a semi-infinite body and a principal shear stress criterion.
6. The undamaged strength was about 39 percent less than expected on the basis of fiber-lot-acceptance tests. Wrinkles in the 0° layers probably caused the low strengths. It is believed that the wrinkles reduced the strengths of the impacted specimens likewise. For this reason, the ratios of impact strength to undamaged strength should not have been affected by the wrinkles.

REFERENCES

1. Poe, Jr., C. C.; Illg, W.; and Garber, D. P.: A Program to Determine the Effect of Low-velocity Impacts on the Strength of the Filament-wound Rocket Motor Case for the Space Shuttle. NASA TM 87588, September 1985.
2. Whitcomb, John D.; and Raju, Ivatury S.: Analysis of Interlaminar Stresses in Thick Composite Laminates With and Without Edge Delamination. Delamination and Debonding of Materials, ASTM STP 876, American Society for Testing and Materials, 1985, pp. 69-94.
3. Jones, Walter C.; and Studdert, G. Michael: Improved Processing Developments for Carbon/Carbon Composites. Society of Aerospace Material and Process Engineers. Proceedings of 16th National Symposium and Exhibit, Vol. 16, April 1971. pp. 67-80.
4. Greszczuk, Longin B.: Damage in Composite Materials due to Low Velocity Impact. Impact Dynamics, John Wiley & Sons, Inc., 1982, pp. 55-94.
5. Shivakumar, K. N.; Elber, W.; and Illg, W.: Prediction of Impact Force and Duration During Low Velocity Impact on Circular Composite Laminates. Journal of Applied Mechanics, Vol. 52, September 1985. pp. 675-680.
6. Love, A. E. H.: The Stress Produced in a Semi-infinite Solid by Pressure on Part of the Boundary. Phil. Trans. Roy. Soc. Lond. A, Vol. 228, 1929, pp. 377-420
7. Harris, C. E.; and Morris, D. H.: Preliminary Report on Tests of Tensile Specimens with a Part-Through Surface Notch for a Filament-Wound Graphite/Epoxy Material. NASA CR-172545, 1985.
8. Harris, C. E.; and Morris, D. H.: The Fracture of Thick Graphite/Epoxy Laminates with Part-Through Surface Flaws. Composite Materials: Fatigue and Fracture, ASTM STP 907, American Society for Testing and Materials, 1986, pp. 100-114.
9. Elber, Wolf: Failure Mechanics in Low-Velocity Impacts on Thin Composite Plates. NASA TP 2152, May 1983.
10. Daniel, Issac M.: Behavior of Graphite/Epoxy Plates with Holes under Biaxial Loading. Experimental Mechanics, Vol. 20, 1980, pp. 1-8.
11. Daniel, Issac M.: Biaxial Testing of $[0_2/\pm 45]_s$ Graphite/Epoxy Plates with Holes. Experimental Mechanics, Vol. 22, 1982, pp. 188-195.
12. Harris, C. E.; and Morris, D. H.: Fracture Behavior of Thick, Laminated Graphite/Epoxy Composites. NASA CR-3784, 1984.

Table 1. Test results for filled ring.

Specimen number	Width, in.	Kinetic energy, ft-lbf	Impact force, kips	Contact dia., in.	Damage depth, in.	Delam. depth, in. (a)	Equiv. cut depth, in.	Gross stress, ksi for —	
								1st-lig. failure	Rem.-lig. failure
Mass = 6.1 lbm									
7-6	1.3	30.3	9.2	0.40	0.00	0.33	0.22	45.6	45.6
7-15			10.1	.41	.00	—	—	47.4	(b,d)
7-24			10.0	.40	.00	—	—	49.2	(b,d)
7-33			9.8	.41	.00	—	—	51.6	(b)
7-42			10.6	.39	.00	—	.21	46.2	46.5
7-9	1.3	60.6	14.9	.45	.06	—	.17	49.0	49.0
7-18			14.9	.44	.00	—	—	47.1	(b,d)
7-27			14.6	.49	.03	.33	.24	42.8	44.7
7-36			15.3	.48	.10	—	.23	44.0	45.1
7-39			14.1	.46	.13	—	.18	42.3	48.7
Mass = 11.1 lbm									
7-7	1.3	55.5	13.5	.44	.05	.33	.21	44.8	d46.6
7-16			14.0	.46	.10	—	.36	39.6	d39.9
7-25			13.8	.45	.00	—	.17	44.5	49.2
7-34			14.1	.47	.00	—	.20	47.2	47.2
7-43			14.1	.46	.00	—	.22	43.4	d46.0
7-8	1.5	111.	c17.8	.62	.16	.33	.21	41.7	d46.6
7-17			c17.7	.68	.20	—	.23	39.5	d45.4
7-26			c19.3	.66	.20	—	.19	41.4	d47.7
7-35			19.8	.55	.11	—	.21	39.5	d46.4
7-44			19.0	.55	.11	—	.23	41.9	d45.5

a After first ligament failed.

b First and remaining ligaments failed simultaneously.

c Impact caused visible crater.

d Innermost surface layers broke at grip.

Table I. Continued.

Specimen number	Width, in.	Kinetic energy, ft-lbf	Impact force, kips	Contact dia., in.	Damage depth, in.	Delam. depth, in. (a)	Equiv. cut depth, in.	Gross stress, ksi for —	
								1st-lig. failure	Rem.-lig. failure
Mass = 19.9 lbm									
7-1	1.3	49.8	—	0.43	0.00	0.33	0.20	43.4	f46.9
7-10	1.3		12.3	.42	.00	—	.23	42.9	f45.1
7-19	1.16		12.4	.45	.00	—	.23	45.4	45.4
7-28	1.3		12.4	.45	.00	—	.18	47.3	f48.2
7-2	1.5	99.5	17.9	.49	.10	.33	.30	41.6	41.9
7-11	1.42		18.0	.49	.18	—	.21	41.2	f46.6
7-20	1.5		c16.9	.62	.13	—	.19	38.1	47.5
7-29	1.5		17.5	.50	.15	—	.19	41.4	47.7
7-37	1.5		17.7	.54	.00	—	.25	43.8	f44.1
7-3	1.3	199.	c22.3	.72	.20	—	.16	31.3	f50.1
7-12	1.5		c21.7	.71	.23	.45	.22	36.6	f45.6
7-21	1.5		c20.5	.72	.22	—	.22	26.2	f45.6
7-30	1.3		c19.5	.80	.32	—	.15	30.6	51.4
7-38	1.5		c19.0	.76	.20	--	--	(d)	(d)

a After first ligament failed.

b First and remaining ligaments failed simultaneously.

c Impact caused visible crater.

d Specimen was inadvertently loaded in compression.

e Signal overranged and actual force was a little larger.

f Innermost surface layers broke at grip.

Table I. Concluded.

Specimen number	Width, in.	Kinetic energy, ft-lbf	Impact force, kips	Contact dia., in.	Damage depth, in.	Delam. depth, in. (a)	Equiv. cut depth, in.	Gross stress, ksi for —	
								1st—lig. failure	Rem.—lig. failure
Mass = 41.1 lbm									
7-4	1.3	51.4	11.4	0.42	0.07	—	—	43.4	(b,d)
7-13			—	.46	.00	.33	.18	43.7	d48.6
7-22			11.7	.43	.00	—	.20	45.1	d47.2
7-31			—	.42	.00	—	.18	48.1	d48.6
7-40			11.7	.42	.00	—	—	46.2	(b)
7-5	1.3	206.	c21.6	.66	.20	—	.29	37.4	d42.6
7-14	1.5		c21.2	.74	.20	.33	.27	32.0	d43.4
7-23	1.5		c18.9	.72	.20	—	.23	38.1	45.1
7-32	1.5		c21.1	.77	.21	—	.17	32.9	d49.2
7-41	1.49		c21.7	.70	.20	—	.31	36.1	41.8
Static indentation test									
1-14	1.5	—	16.9	—	.00	—	.31	37.3	41.5

a After first ligament failed.

b First and remaining ligaments failed simultaneously.

c Impact caused visible crater.

d Innermost surface layers broke at grip.

Table II. Test results for empty ring.

Specimen number	Width, in.	Kinetic energy, ft-lbf	Impact force, kips	Contact dia., in.	Damage depth, in.	Delam. depth, in. (a)	Equiv. cut depth, in.	Gross stress, ksi for -	
								1st-lig. failure	Rem.-lig. failure
Mass = 6.1 lbm									
5-3	1.3	30.3	9.0	0.38	0.00	-	-	46.8	(b,c)
5-15			9.1	.39	.00	-	-	41.8	(b,c)
5-26			8.9	.38	.00	.33	0.27	42.3	c43.3
5-36			9.0	.37	.00	-	-	47.6	(b,c)
5-4	1.3	60.6	15.0	.46	.10	-	.37	34.6	c39.6
5-16			14.9	.45	.08	.33	.21	46.5	c46.5
5-27			13.3	.47	.08	-	.21	39.0	46.7
5-37			14.0	.45	.03	-	.39	39.1	c39.1
Mass = 11.1 lbm									
5-5	1.3	27.8	8.3	.36	.00	.45	.26	43.1	c44.0
5-17			8.4	.40	.00	.20	.23	40.4	c45.5
5-38			8.2	.37	.00	-	.24	37.4	c44.9
5-18	1.3	55.5	12.4	.43	.03	.45	.31	40.8	c41.9
5-28			12.0	.43	.10	-	.34	39.6	c40.7
5-39			11.9	.42	.00	-	.29	41.8	42.4
5-6	1.5	111.	17.2	.49	.11	.33	.31	39.1	41.7
5-19			17.7	.50	.11	-	.30	38.1	c42.0
5-29			16.3	.54	.16	-	.29	36.7	42.3
5-40			17.5	.48	.10	-	.36	33.8	c40.1
5-7		114.	17.3	.48	.11	-	.28	37.1	42.9

a After first ligament failed.

b First and remaining ligaments failed simultaneously.

c Innermost surface layers broke at grip.

Table II. Continued.

Specimen number	Width, in.	Kinetic energy, ft-lbf	Impact force, kips	Contact dia., in.	Damage depth, in.	Delam. depth, in. (a)	Equiv. cut depth, in.	Gross stress, ksi for -	
								1st-lig. failure	Rem.-lig. failure
Mass = 19.9 lbm									
5-8	1.3	49.8	9.4	0.39	0.07	-	0.30	41.8	c42.1
5-20			9.8	.39	.10	-	-	46.1	(b)
5-30			9.6	.38	.00	-	-	44.3	(b,c)
5-41			9.7	.39	.00	.45	.24	44.0	c44.6
5-9	1.5	99.5	13.9	.46	.10	-	-	38.4	(b)
5-21			13.9	.46	.08	.20	.33	40.0	c41.1
5-31			13.9	.44	.06	-	.26	41.4	c43.8
5-42			14.0	.49	.10	-	.29	35.7	c42.3
5-10	1.5	199.	18.5	.57	.20	-	.27	31.4	c43.3
5-22			18.3	.61	.20	-	.27	33.3	c43.3
5-32			19.0	.56	.16	.33	.31	41.0	c41.5
5-43			19.6	.54	.16	-	.25	33.8	c44.4

a After first ligament failed.

b First and remaining ligaments failed simultaneously.

c Innermost surface layers broke at grip.

Table II. Concluded.

Specimen number	Width, in.	Kinetic energy, ft-lbf	Impact force, kips	Contact dia., in.	Damage depth, in.	Delam. depth, in. (a)	Equiv. cut depth, in.	Gross stress, ksi for —	
								1st—lig. failure	Rem.—lig. failure
Mass = 41.1 lbm									
5-11	1.5	103.	11.5	0.42	0.00	—	—	46.7	(b,d)
5-23			11.6	.42	.00	.33	.29	42.3	42.3
5-33			11.5	.43	.00	—	—	48.0	(b)
5-44			11.6	.43	.00	—	.27	41.4	d43.2
5-1	1.5	206.	17.2	.49	.12	—	.32	35.2	d41.1
5-13			—	.47	.12	.33	.27	37.9	43.4
5-24			16.9	.44	.11	—	.29	35.2	d42.3
5-34			20.0	—	.00	—	—	43.9	(b)
5-2	1.5	329.	c21.2	—	.12	—	.27	29.5	d43.2
5-14			c20.4	—	.15	.45	.29	37.1	d42.7
5-25			c—	—	.20	—	.37	33.3	39.8
5-35			c20.9	—	.12	—	.39	36.7	d39.0
Static indentation test									
5-12	1.5	—	16.9	—	.12	—	.32	37.1	d41.3

a After first ligament failed.

b First and remaining ligaments failed simultaneously.

c Impact caused visible crater.

d Innermost surface layers broke at grip.

Table III. Strengths of undamaged specimens.

Specimen number	Width, W, in.	Strength, ksi (a)
3-30A	1.0	45.6
3-10A		b45.7
3-28A		46.2
3-18A		54.8
average		48.1 (0.0934)
3-8B	1.0	48.9
3-20B		b51.9
average		50.4 (0.0421)
c3-2A	1.0	52.8
c3-16A		54.0
c3-6A		55.6
average		54.1 (0.0259)
average for W = 1.0 in.		50.6 (0.0803)
4-4A	1.3	49.1
4-17A		51.3
4-7A		56.6
average		52.3 (0.0737)

a Numbers in parentheses are coefficients of variation.

b Innermost surface layers broke at grip.

c Reported in reference 1.

Table III. Concluded.

Specimen number	Width, W, in.	Strength, ksi (a)
4-30B	1.3	42.5
4-24B		52.5
average		47.5 (0.149)
average for W = 1.3 in.		50.4 (0.103)
4-34A	1.5	b49.9
4-19A		b50.3
4-29A		c51.4
average		50.5 (0.0154)
4-16B	1.5	c43.1
4-6B		c50.0
average		46.6 (0.105)
average for W = 1.5 in.		48.9 (0.0678)
average for A specimens		50.1 (0.0739)
average for B specimens		48.2 (0.0902)
average for all specimens		50.1 (0.0805)

a Numbers in parentheses are coefficients of variation.

b Innermost and outermost surface layers broke at grip.

c Innermost surface layers broke at grip.

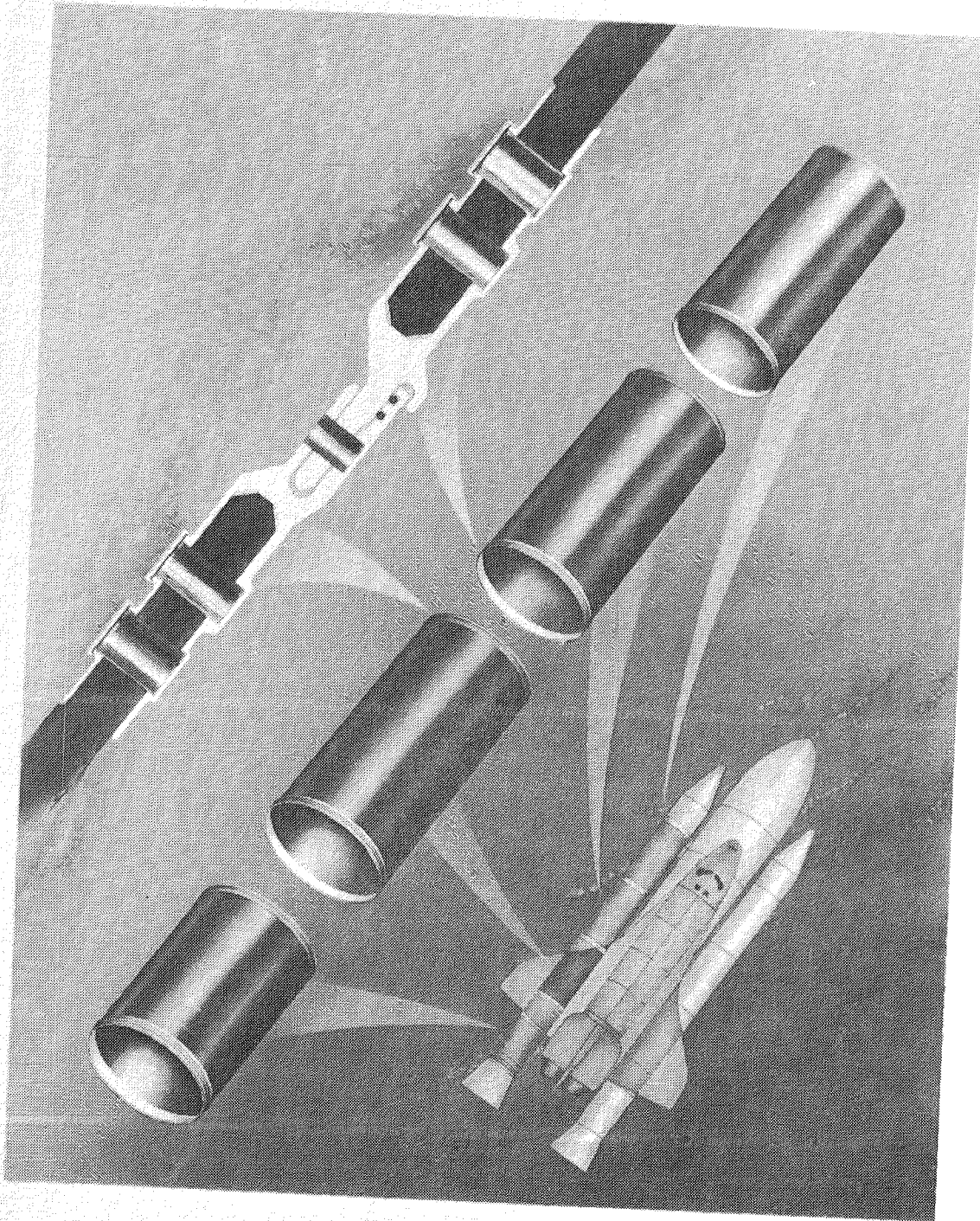
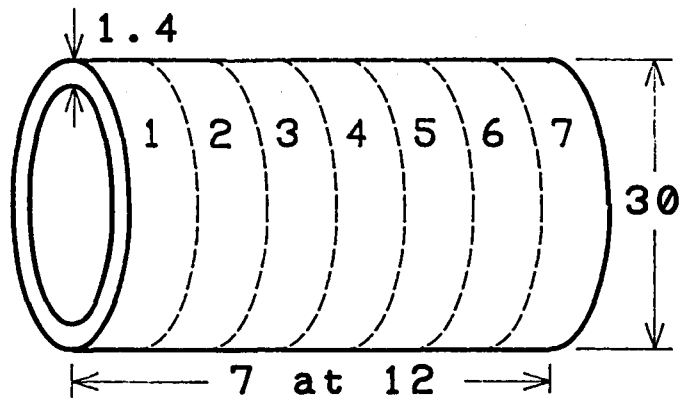
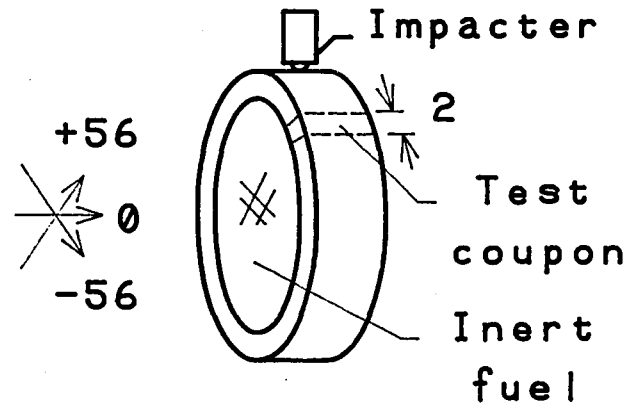


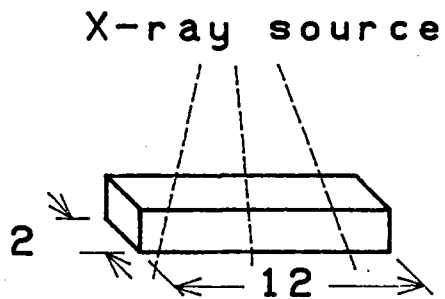
Figure 1.— Space shuttle solid rocket motor.



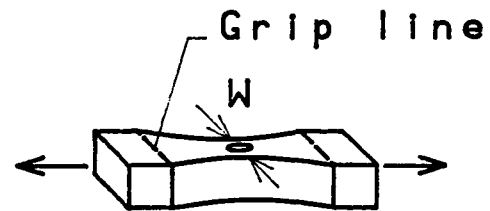
(a) Original cylinder



(b) Impact test



(c) NDE



W = 1.0, 1.3, or 1.5

(d) Tensile test

Figure 2.- Specimens and testing sequence.

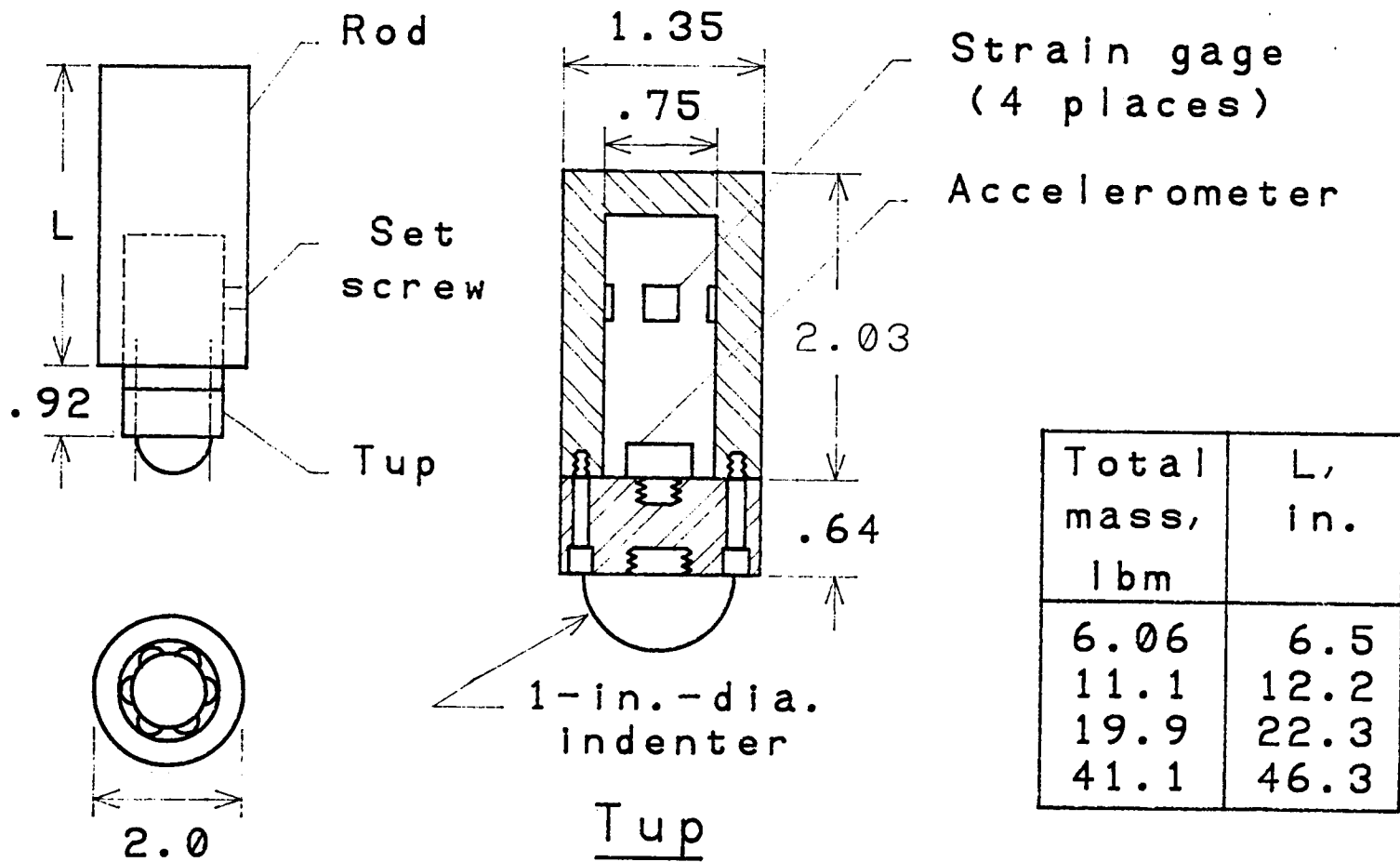
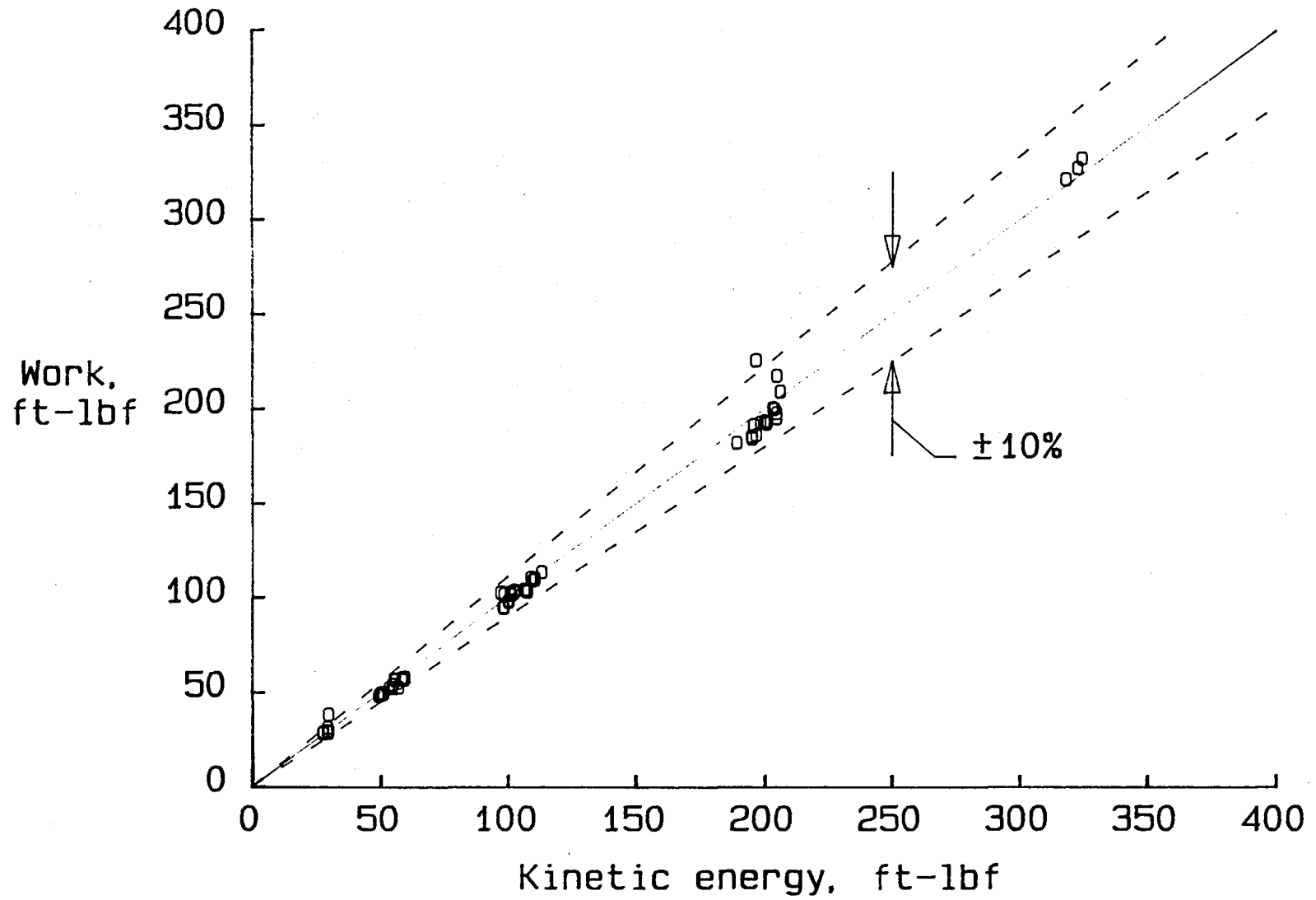
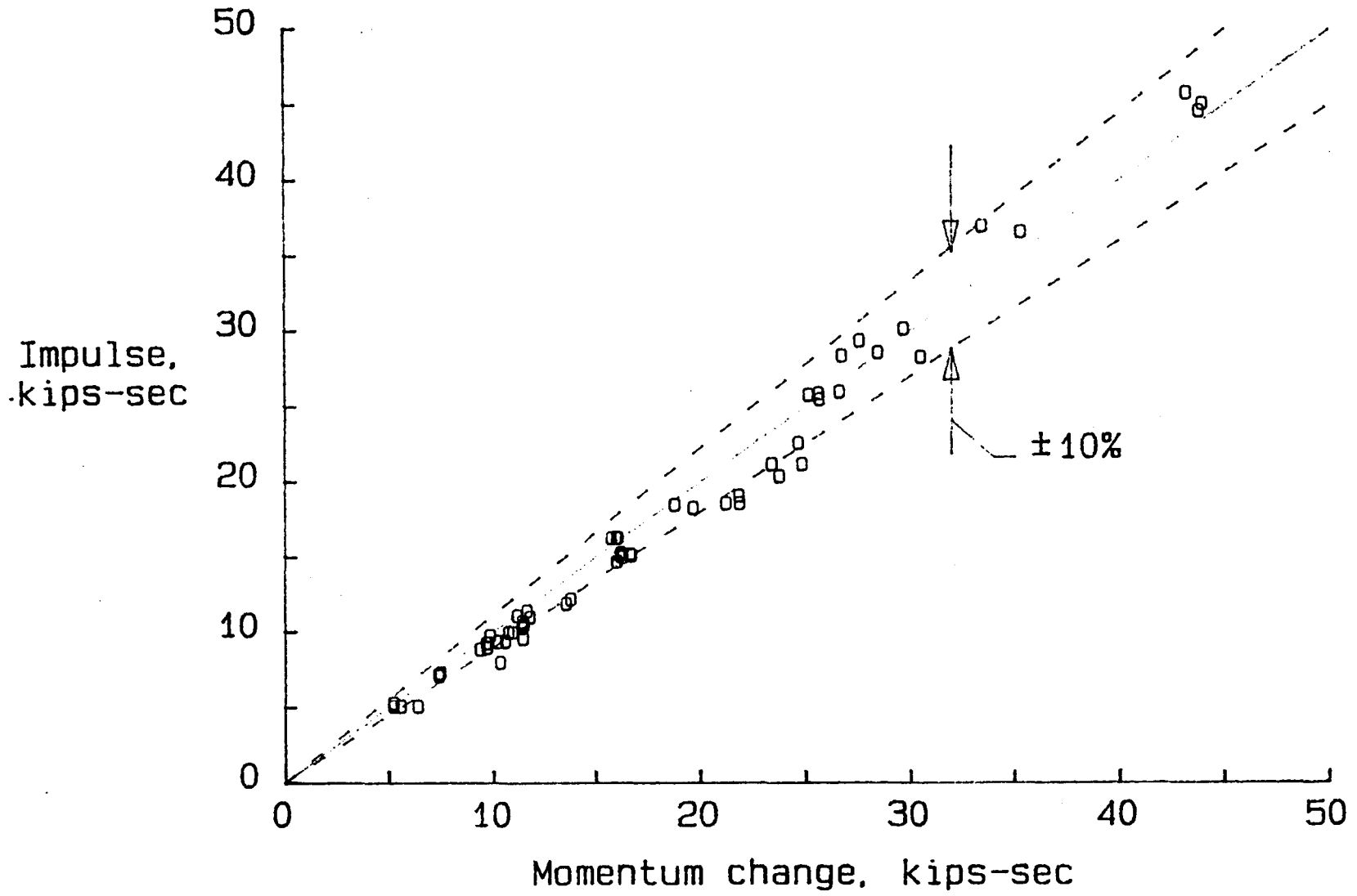


Figure 3.- Sketch of impactor.



(a) Energy correlation

Figure 4.- Calibration check of impactor signals.



(b) Impulse correlation.

Figure 4.- Concluded.

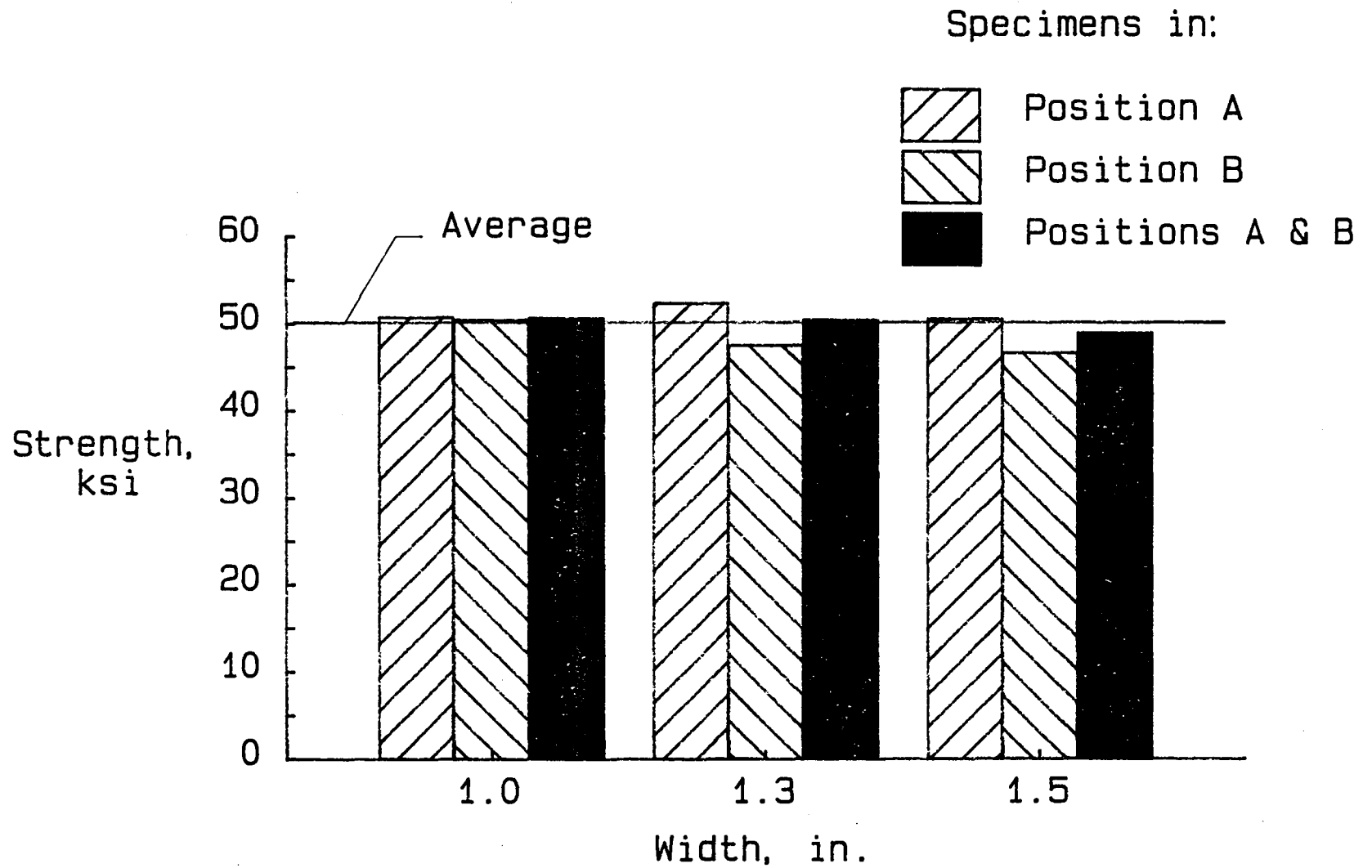


Figure 5.- Strengths of undamaged specimens.

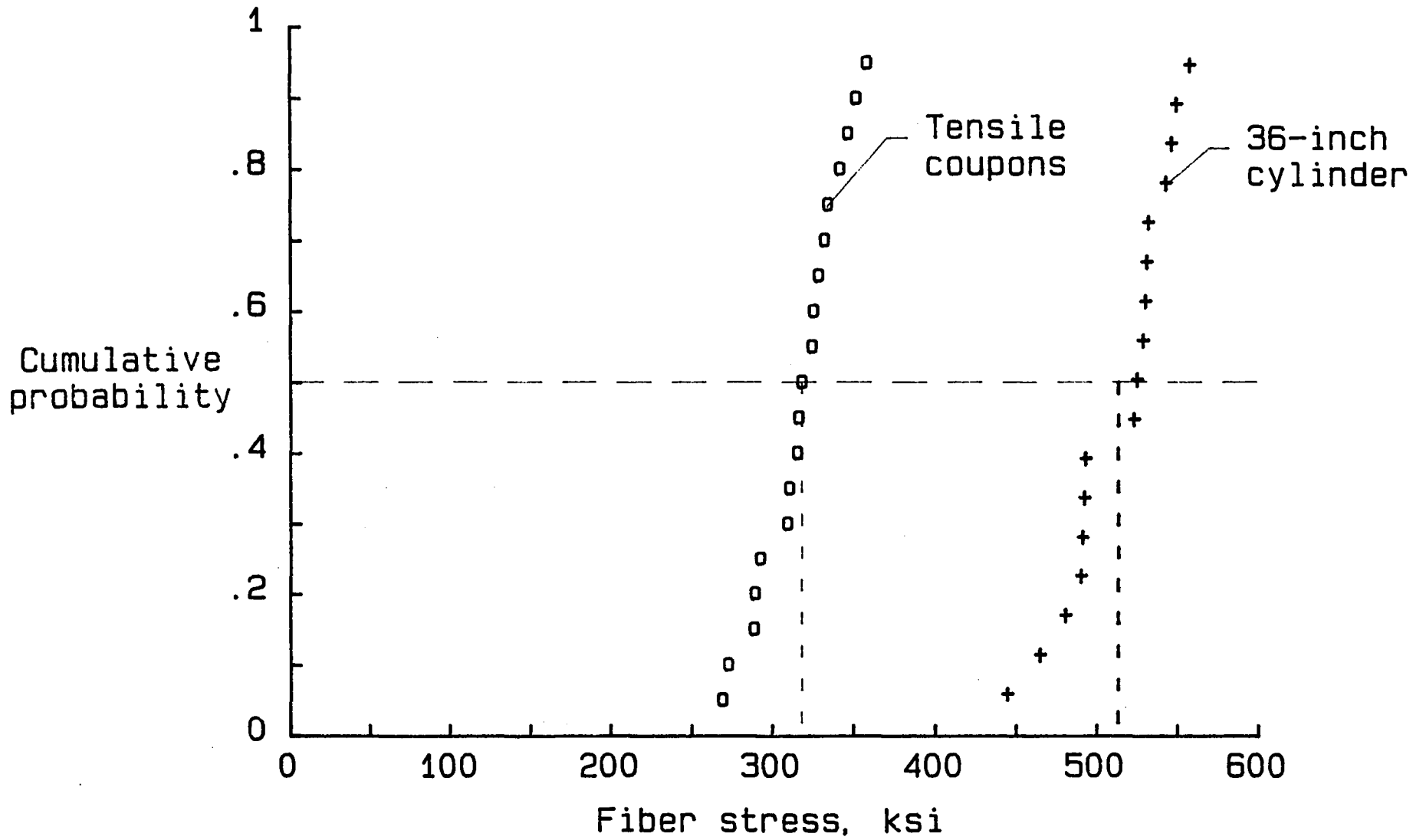


Figure 6.- Cumulative probability of strengths for undamaged specimens and 36-inch-diameter cylinders.

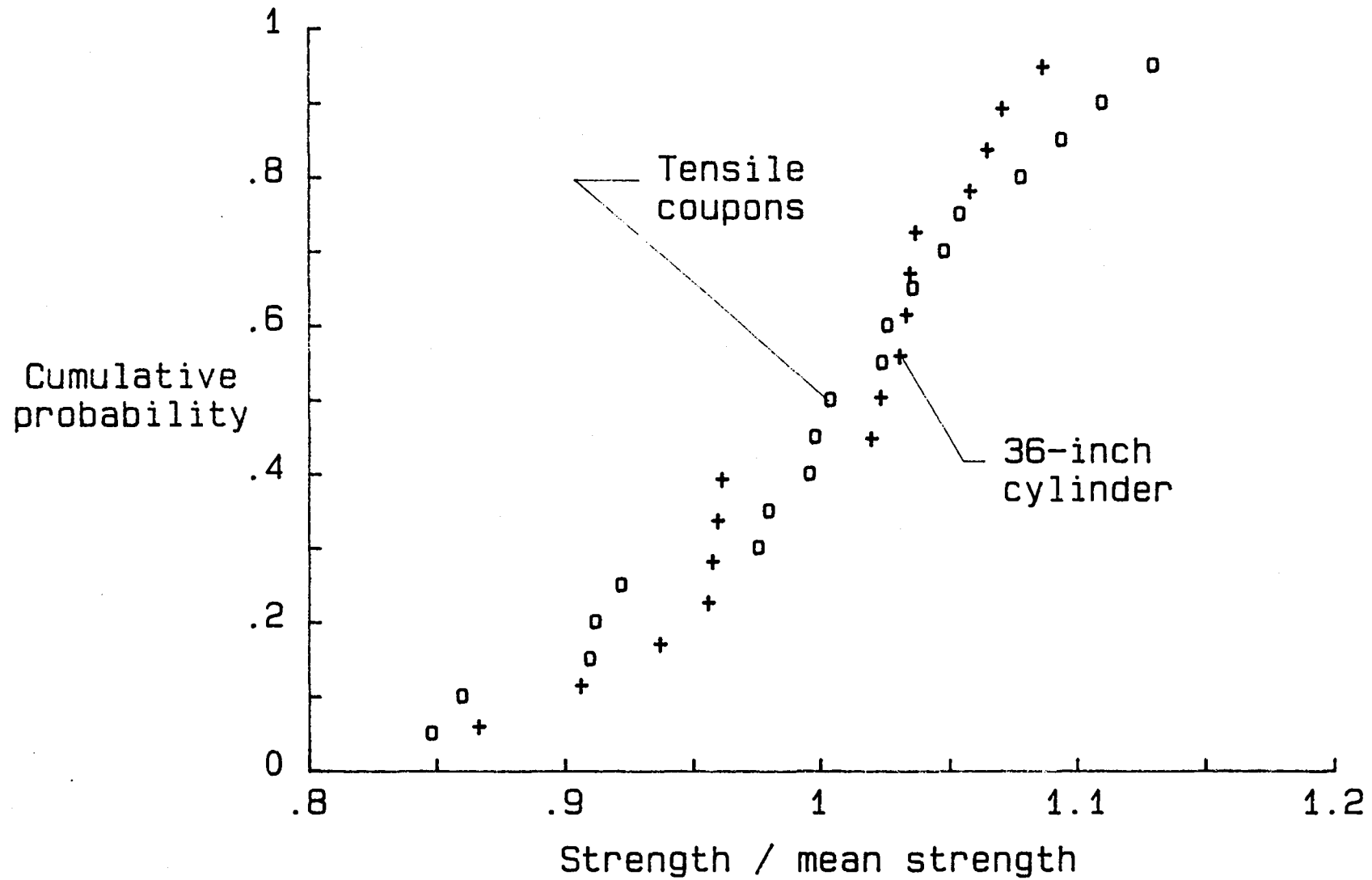
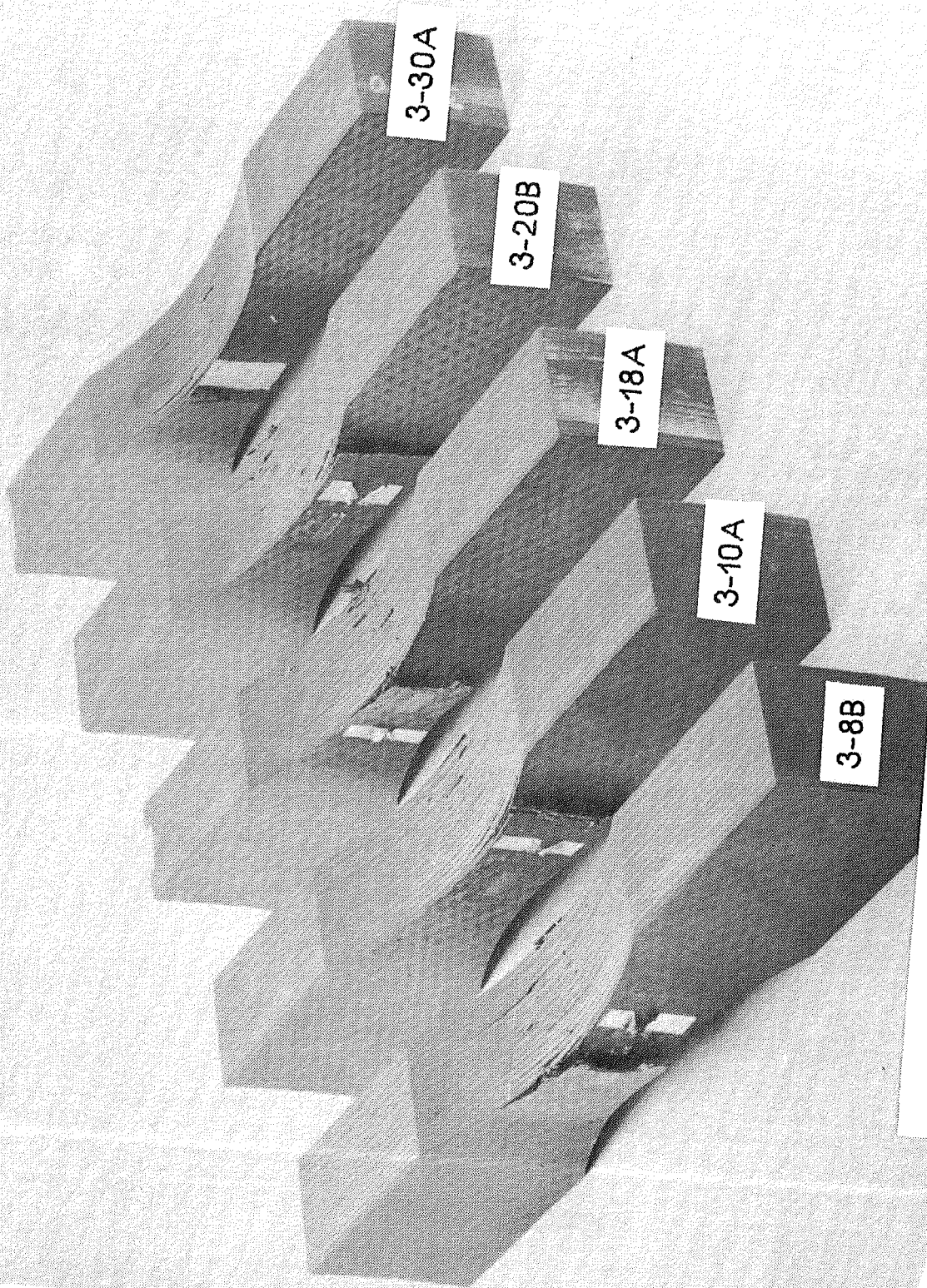
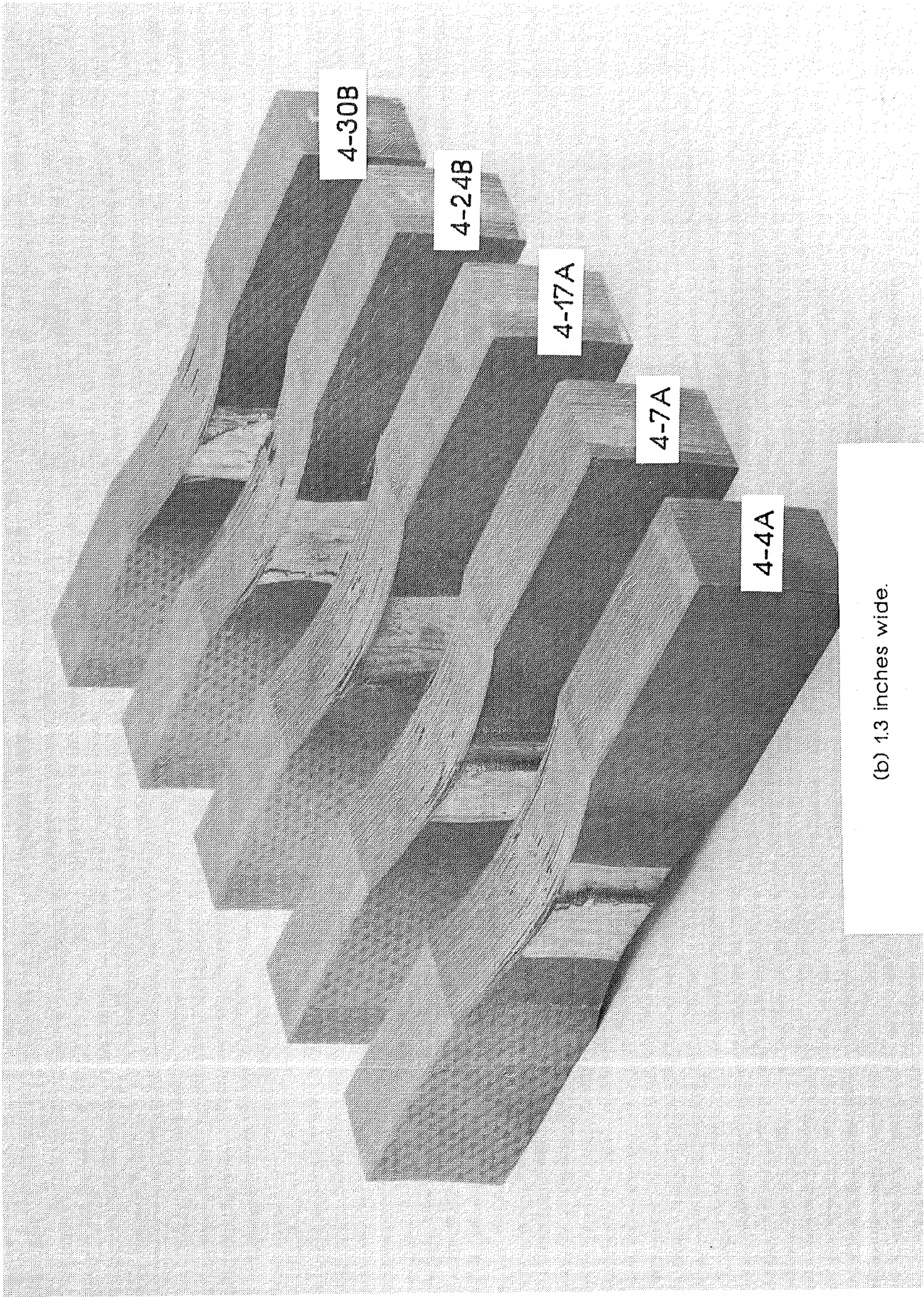


Figure 7.- Cumulative probability of normalized strengths for undamaged specimens and 36-inch-diameter cylinders.



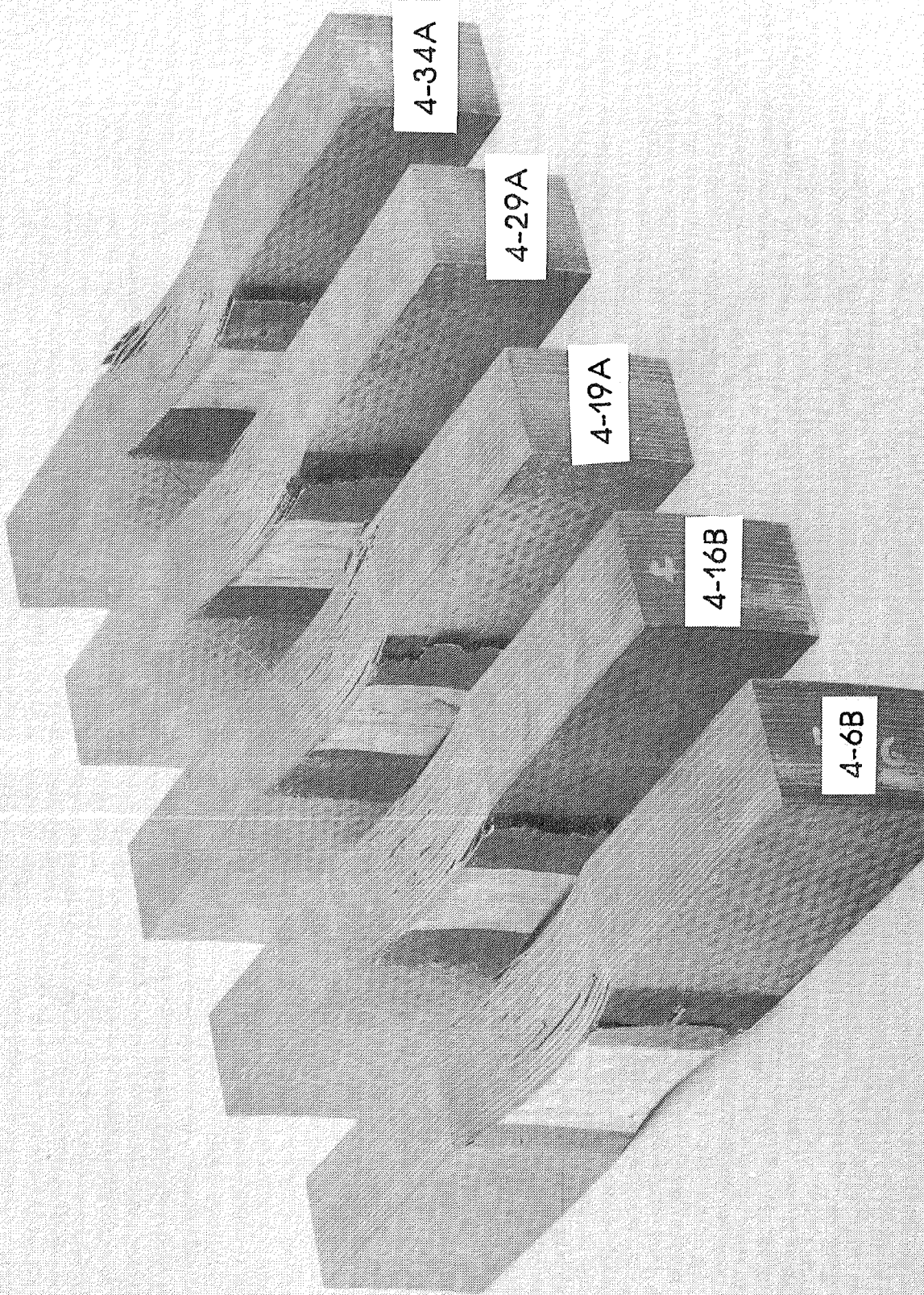
(a) 1.0 inches wide.

Figure 8.- Photographs of failed undamaged specimens.



(b) 1.3 inches wide.

Figure 8.- Continued.



(c) 1.5 inches wide.

Figure 8.- Concluded.

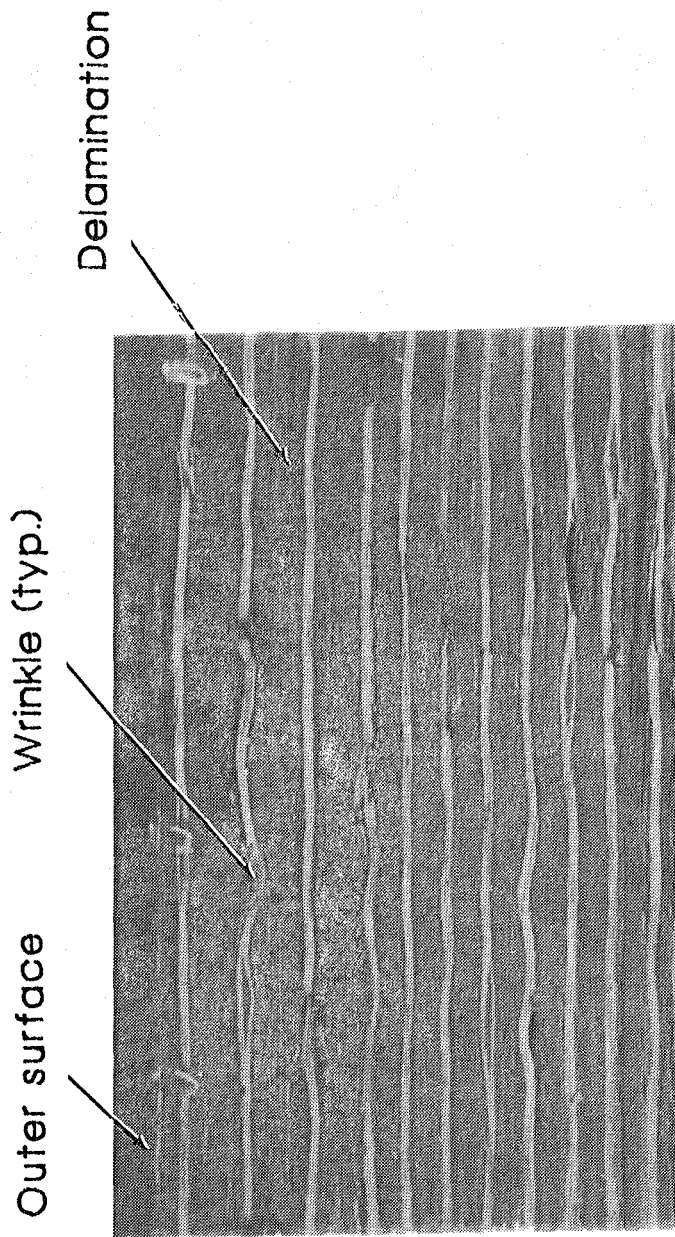


Figure 9.- Photograph of fracture detail in specimen 3-28.

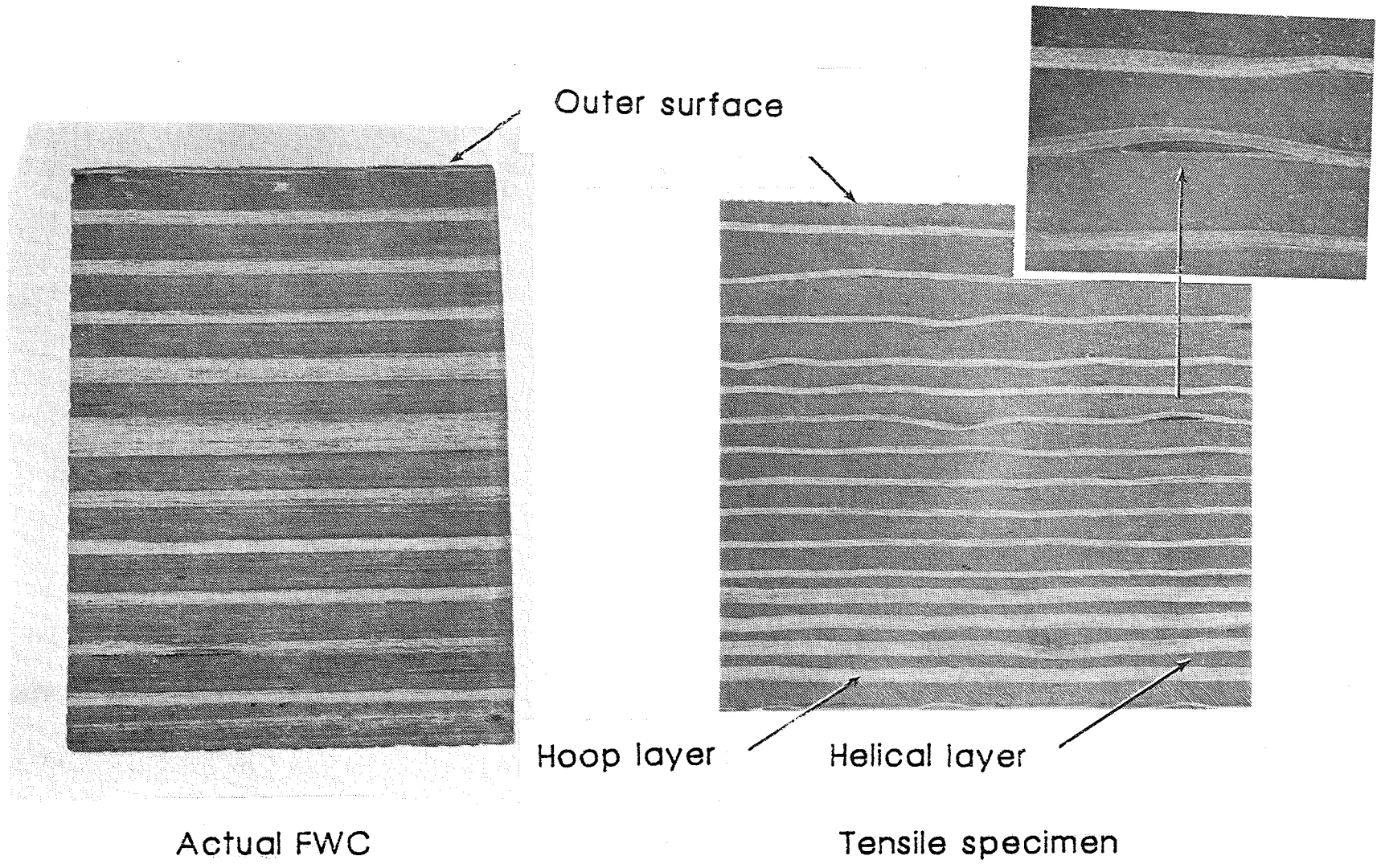
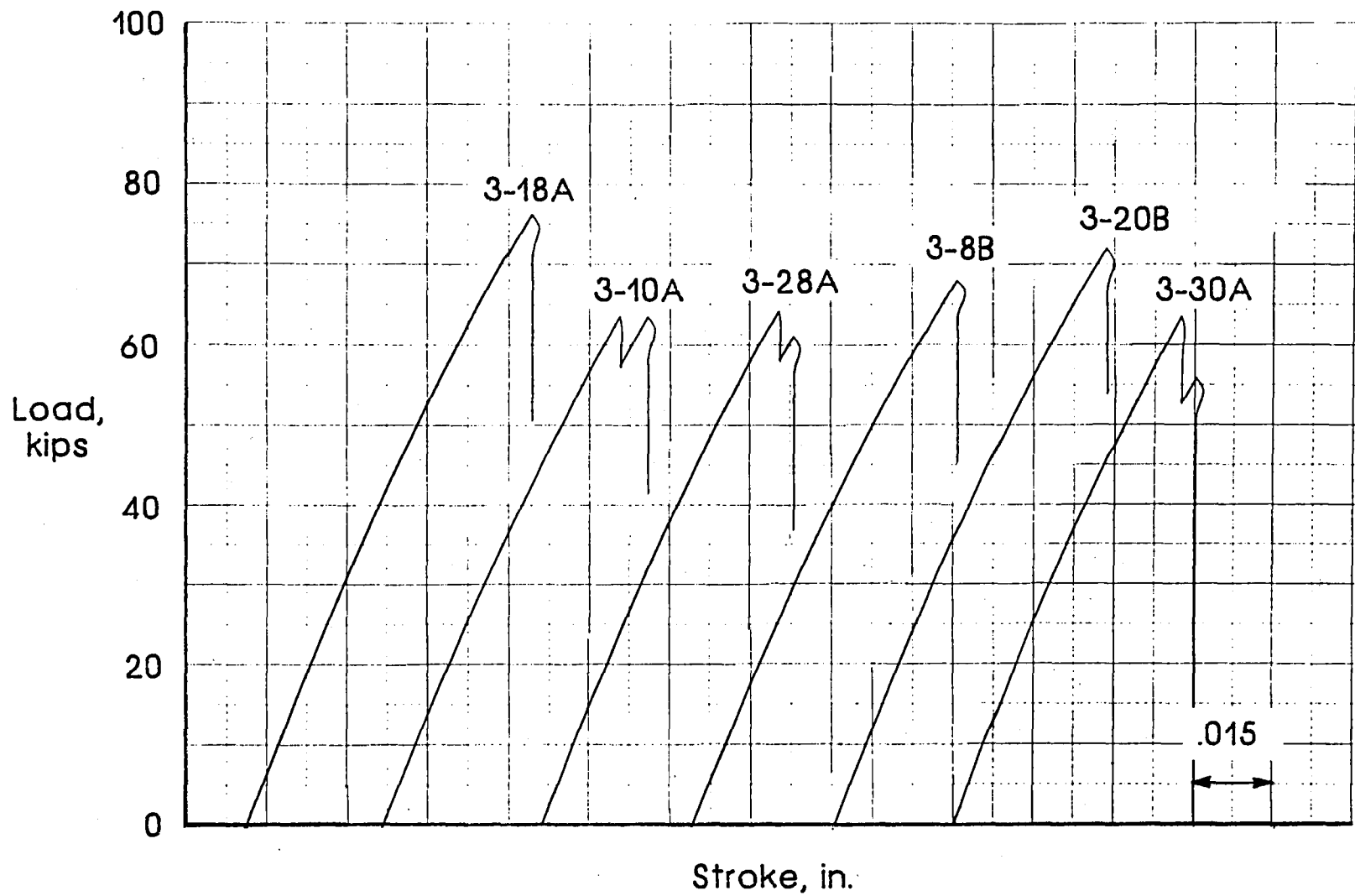
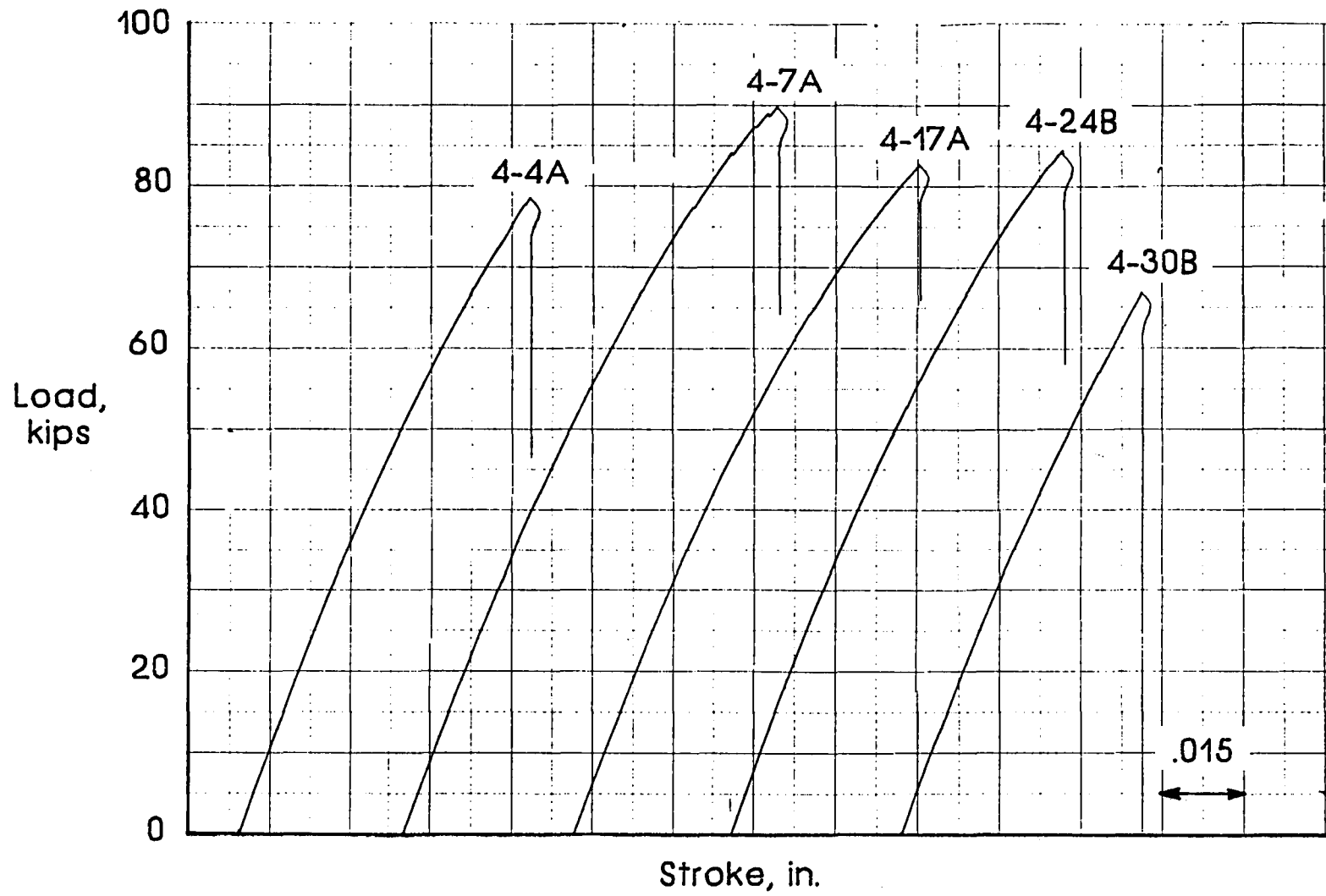


Figure 10.- Photographs of edges of a tensile specimen and a coupon from an actual FWC.



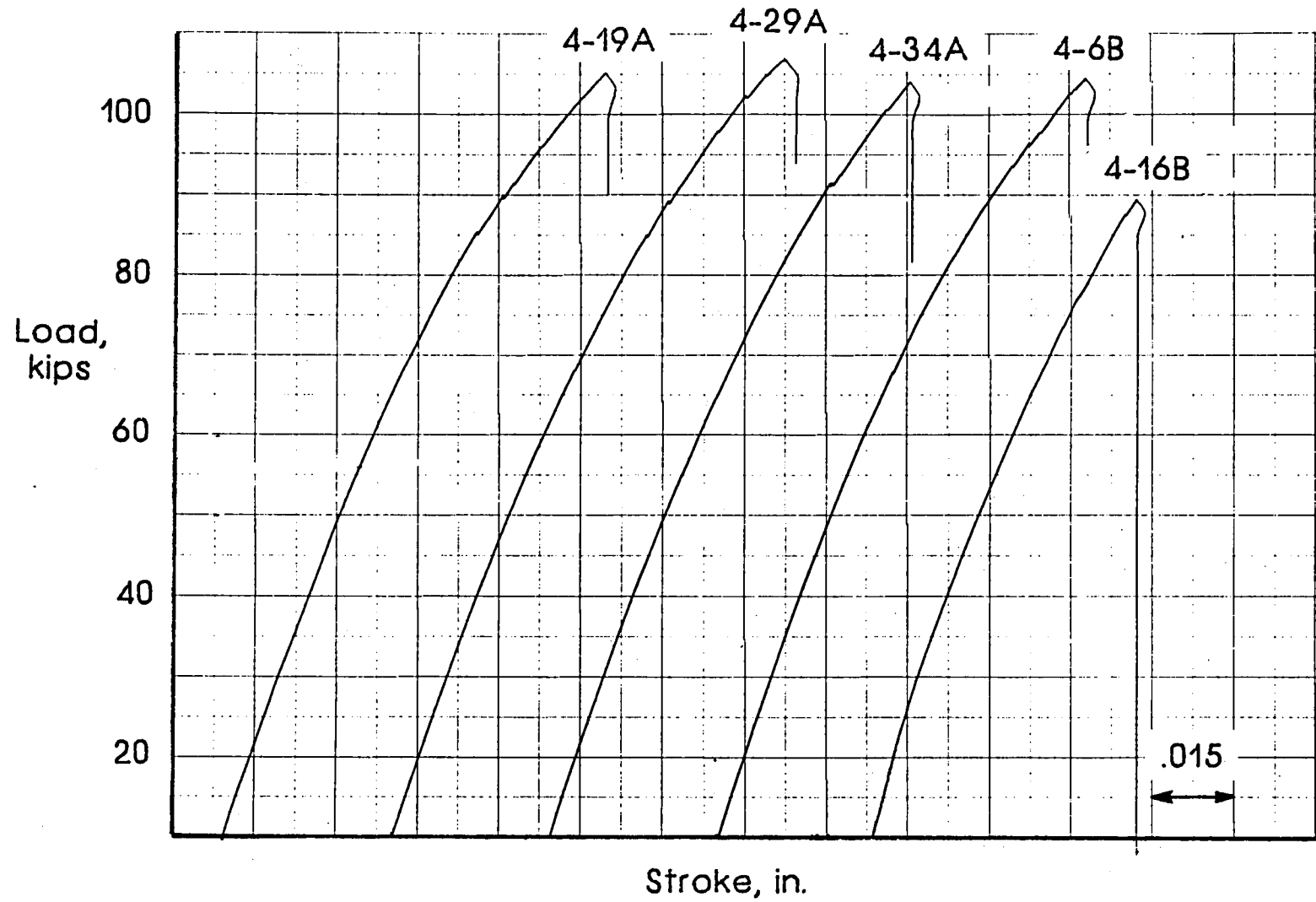
(a) 1.0 inches wide.

Figure 11.- Load stroke records for undamaged specimens.



(b) 1.3 inches wide.

Figure 11.- Continued.



(c) 1.5 inches wide.

Figure 11.- Concluded.

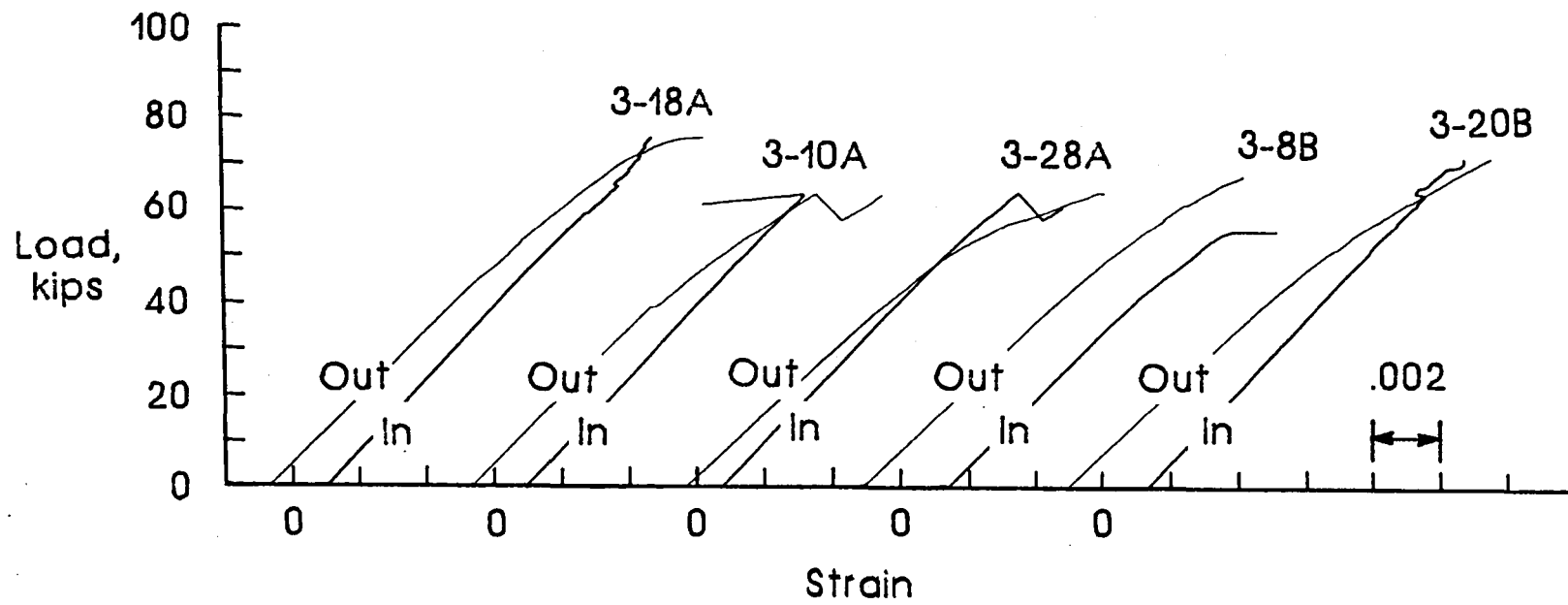
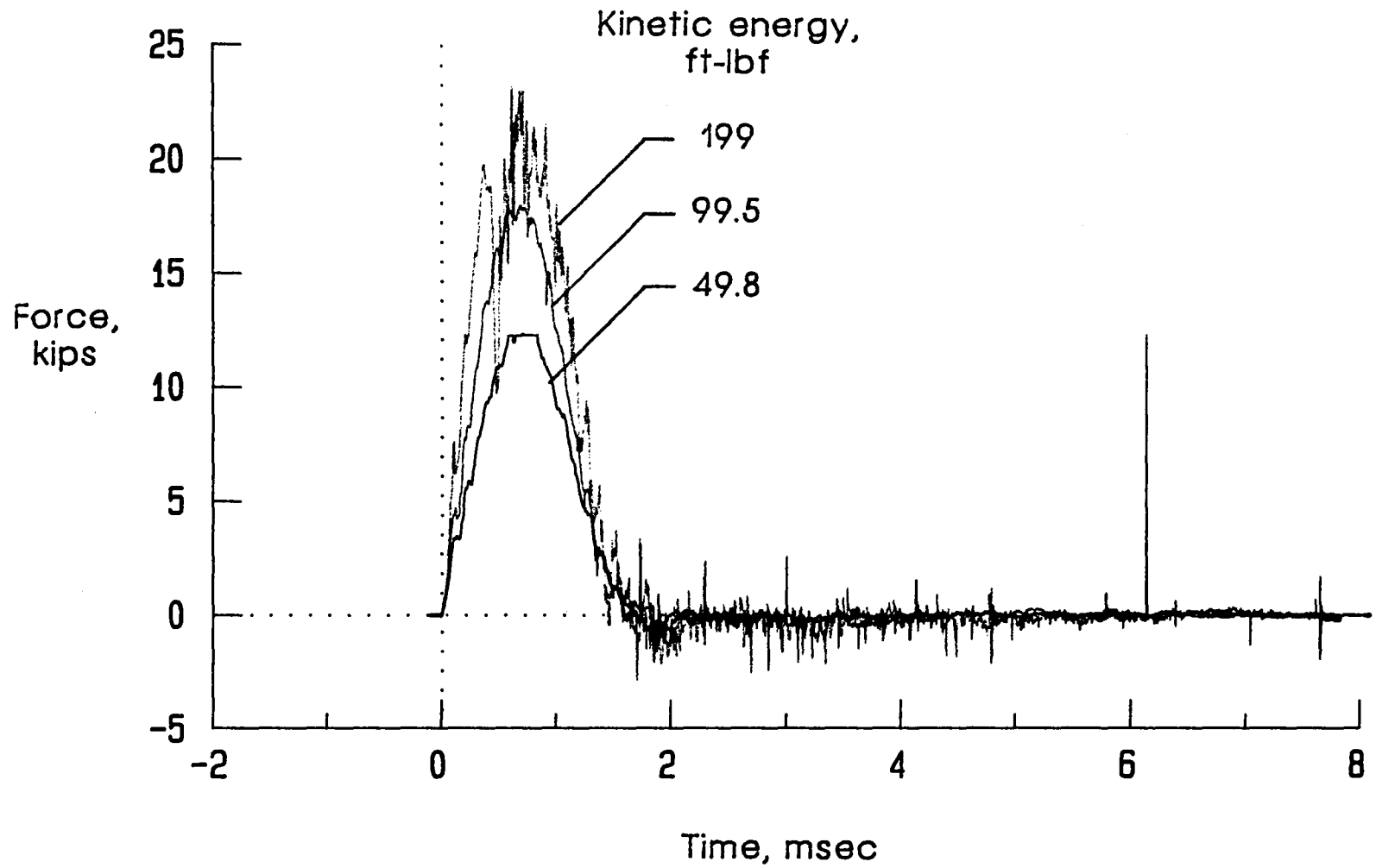
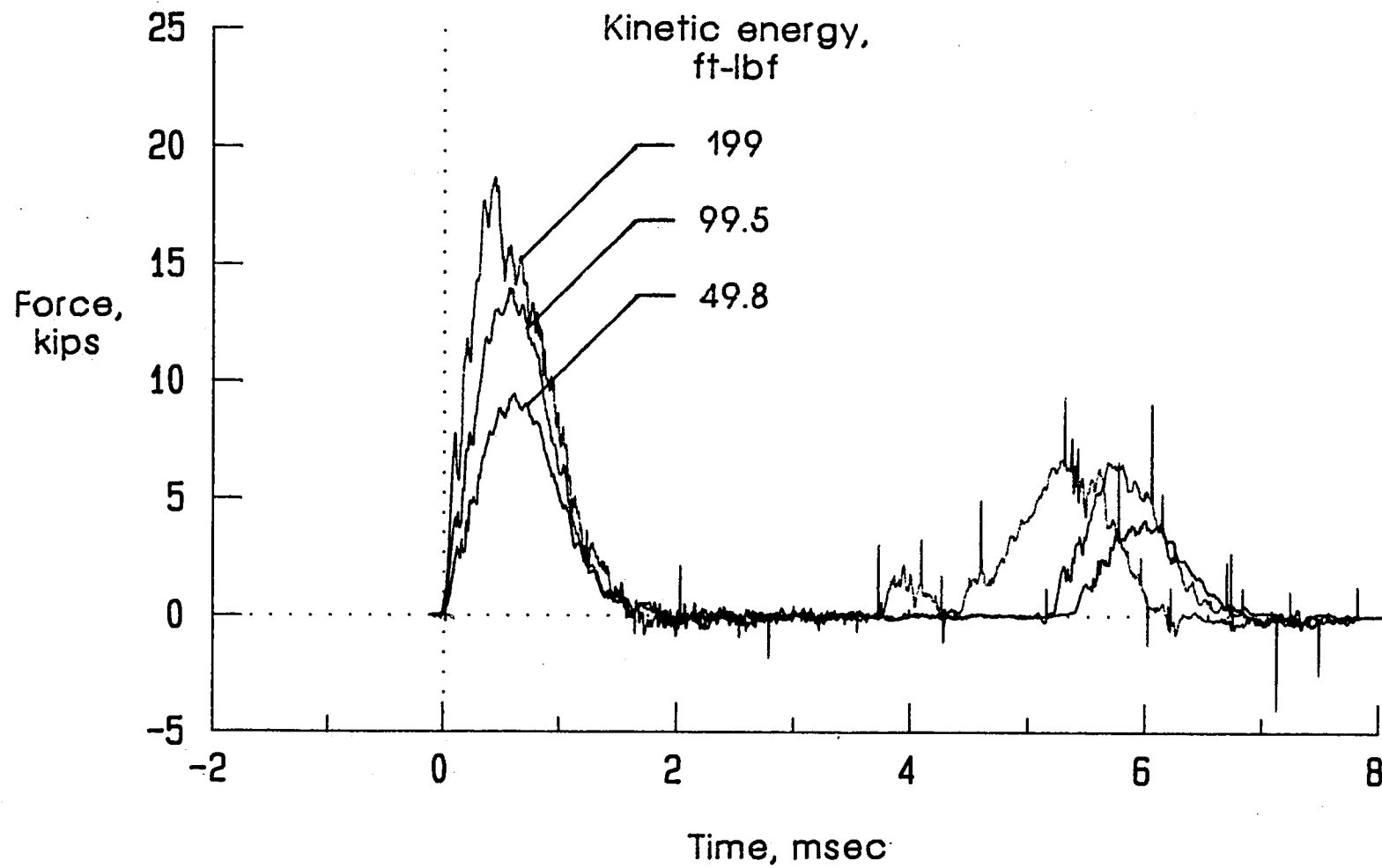


Figure 12.- Load versus strain for 1-inch-wide undamaged specimens.



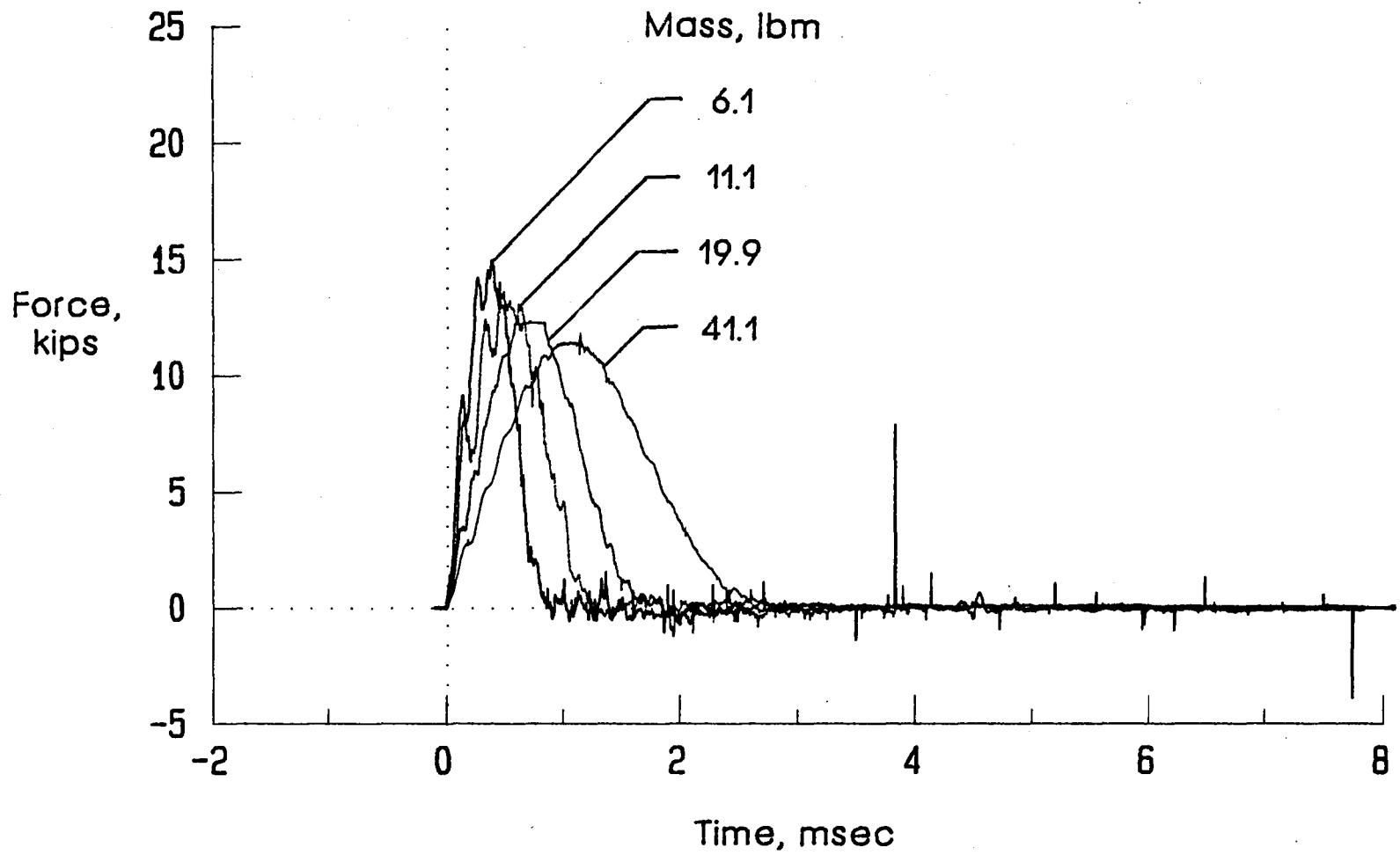
(a) Filled ring.

Figure 13.- Effect of kinetic energy on impact force versus time for 19.9-lbm impactor.



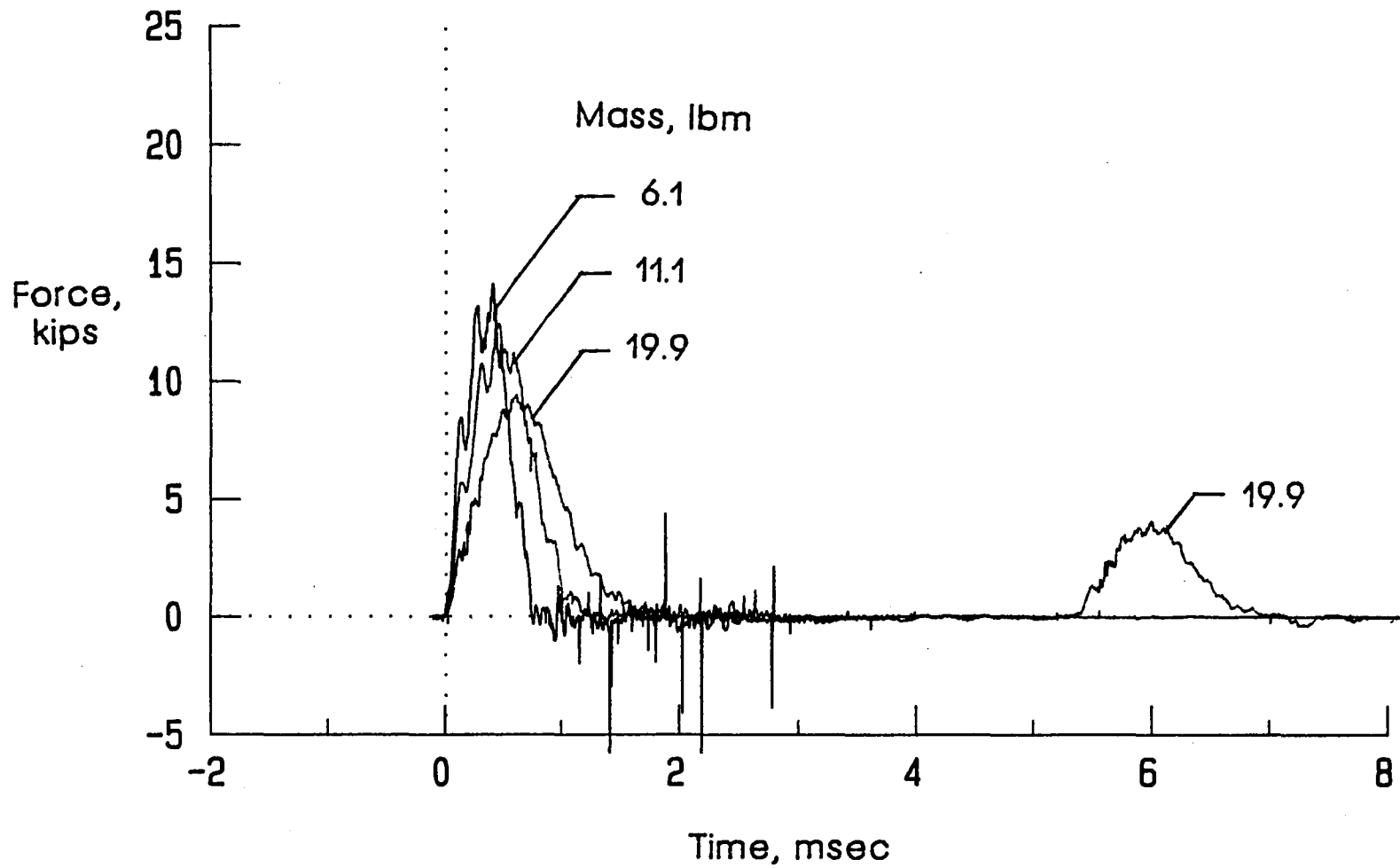
(b) Empty ring.

Figure 13.- Concluded.



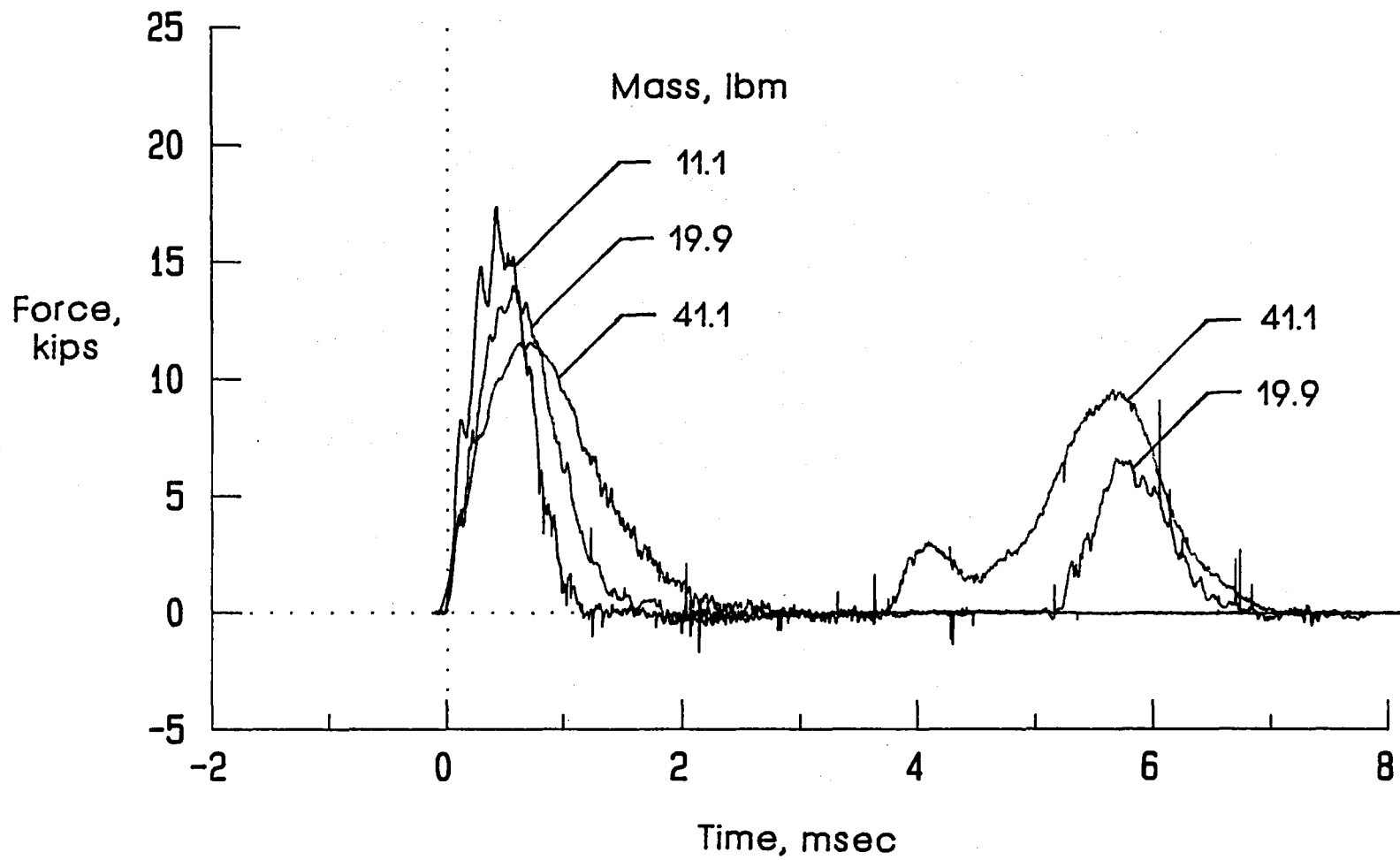
(a) Filled ring, KE = 50 ft-lbf.

Figure 14.- Effect of impact mass on impact force versus time.



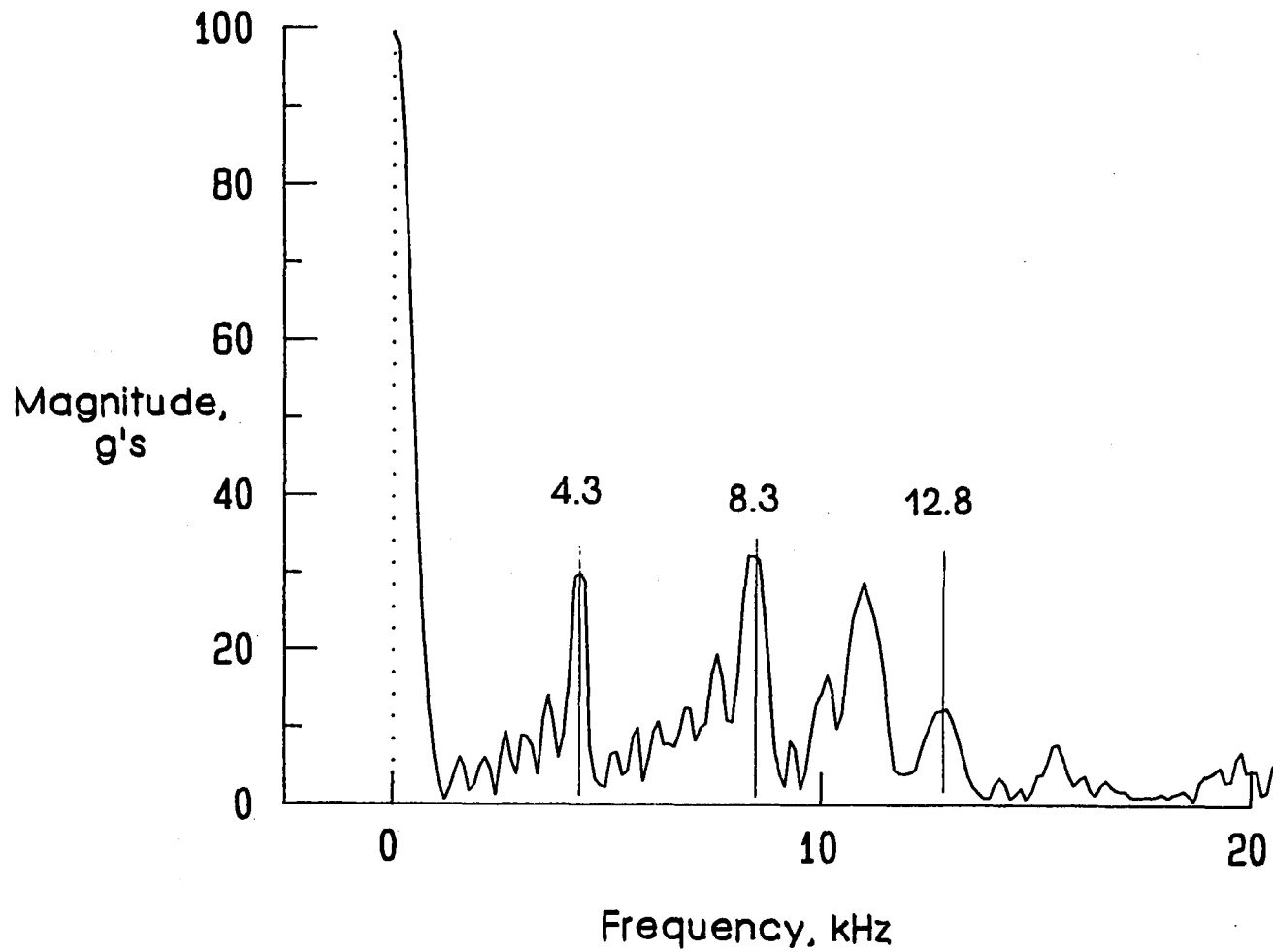
(b) Empty ring, KE = 50 ft-lbf.

Figure 14.- Continued.



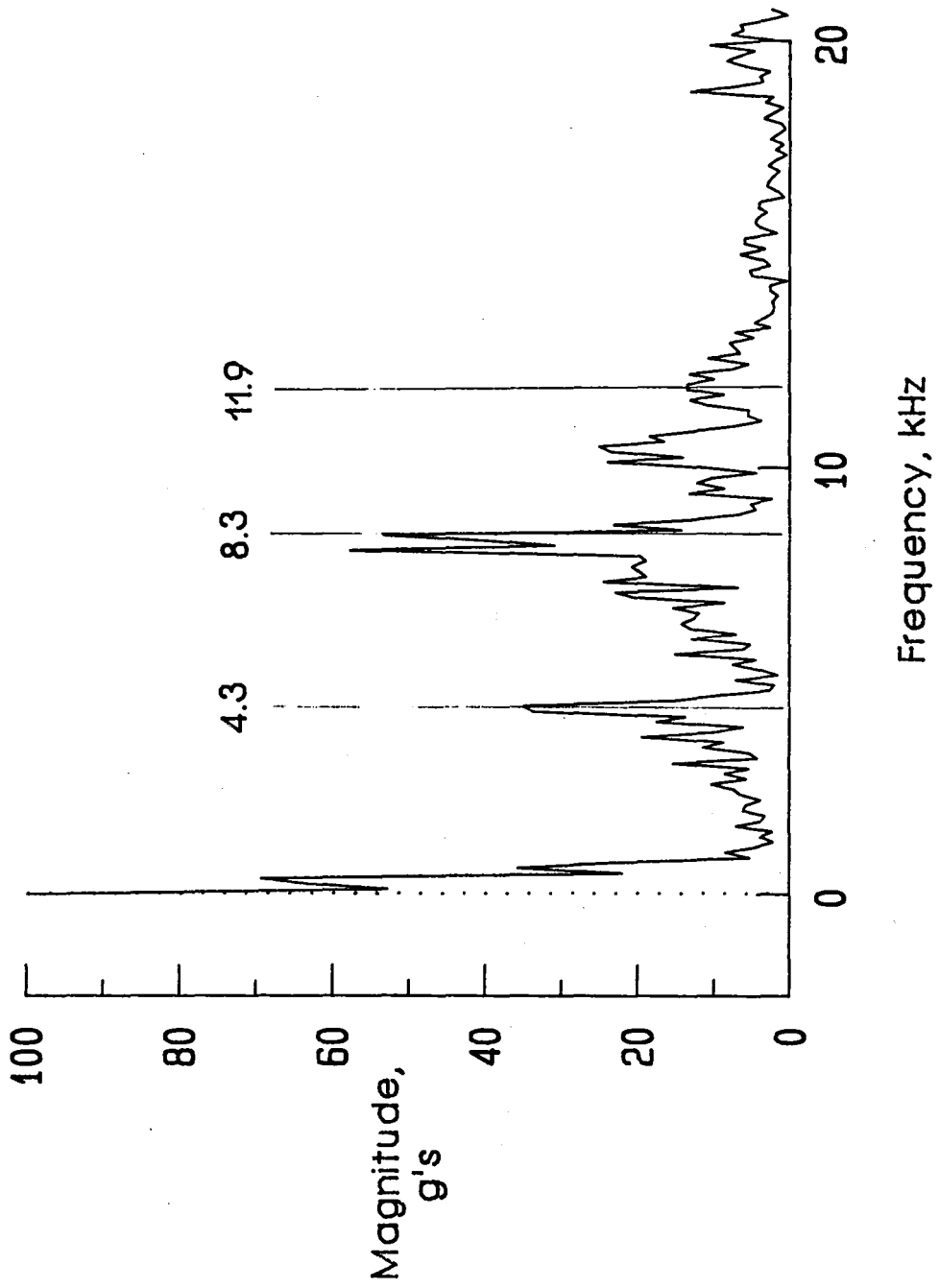
(c) Empty ring, KE = 100 ft-lbf.

Figure 14,- Concluded.



(a) Filled ring.

Figure 15.- Fourier coefficients of accelerometer signal for 19.9 lbm impactor and 99.5 ft-lbf kinetic energy.



(b) Empty ring.

Figure 15.- Concluded.

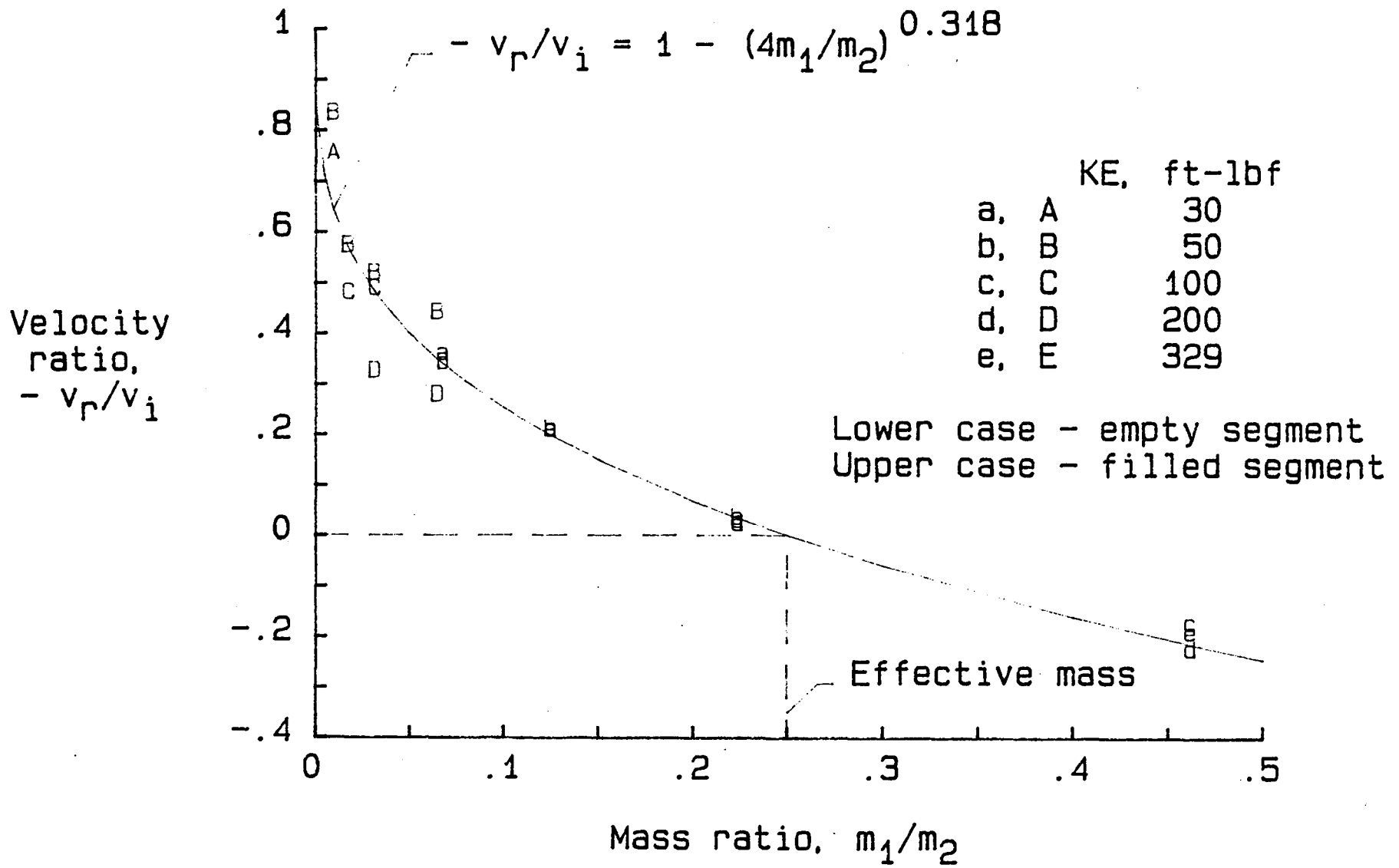
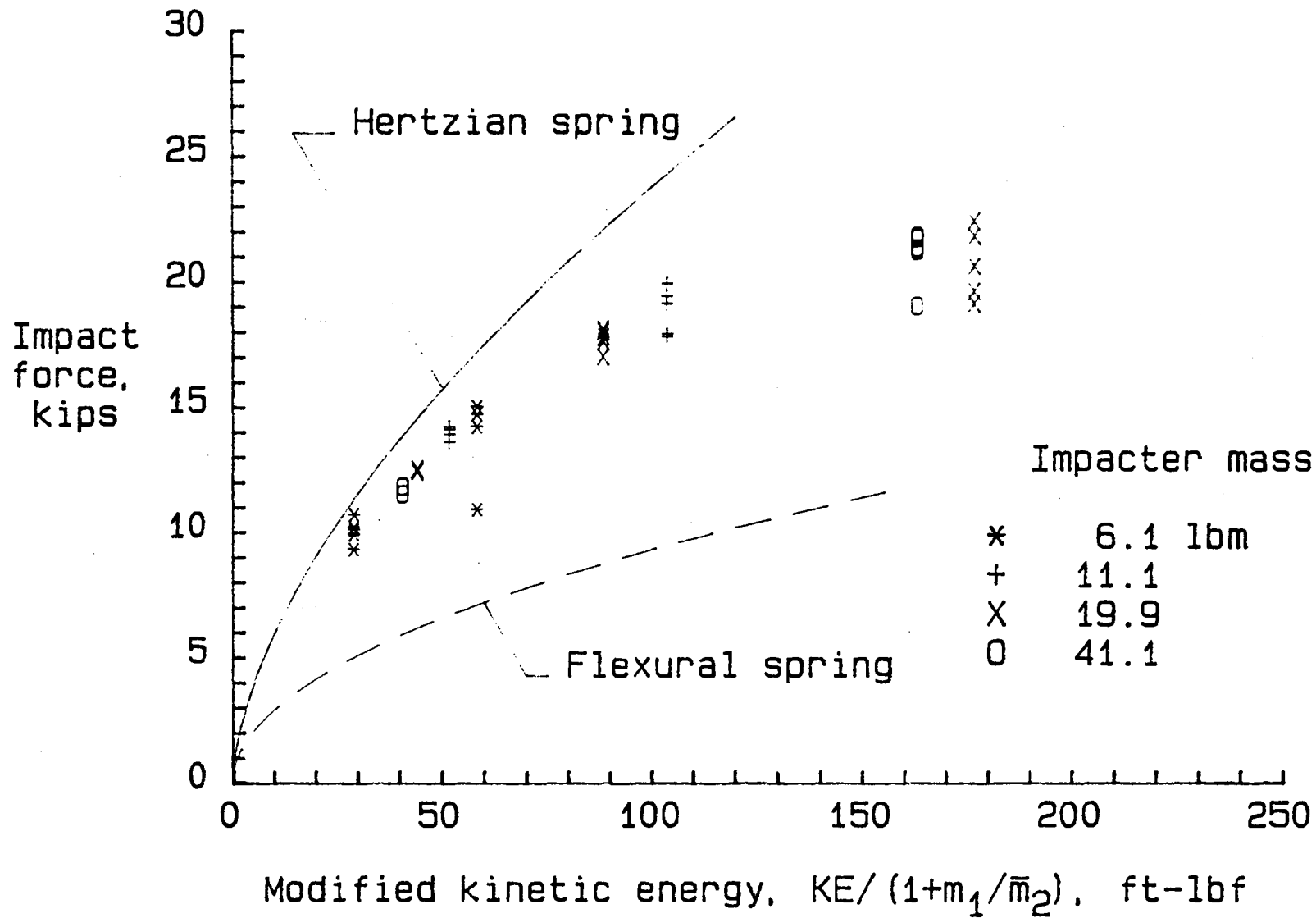
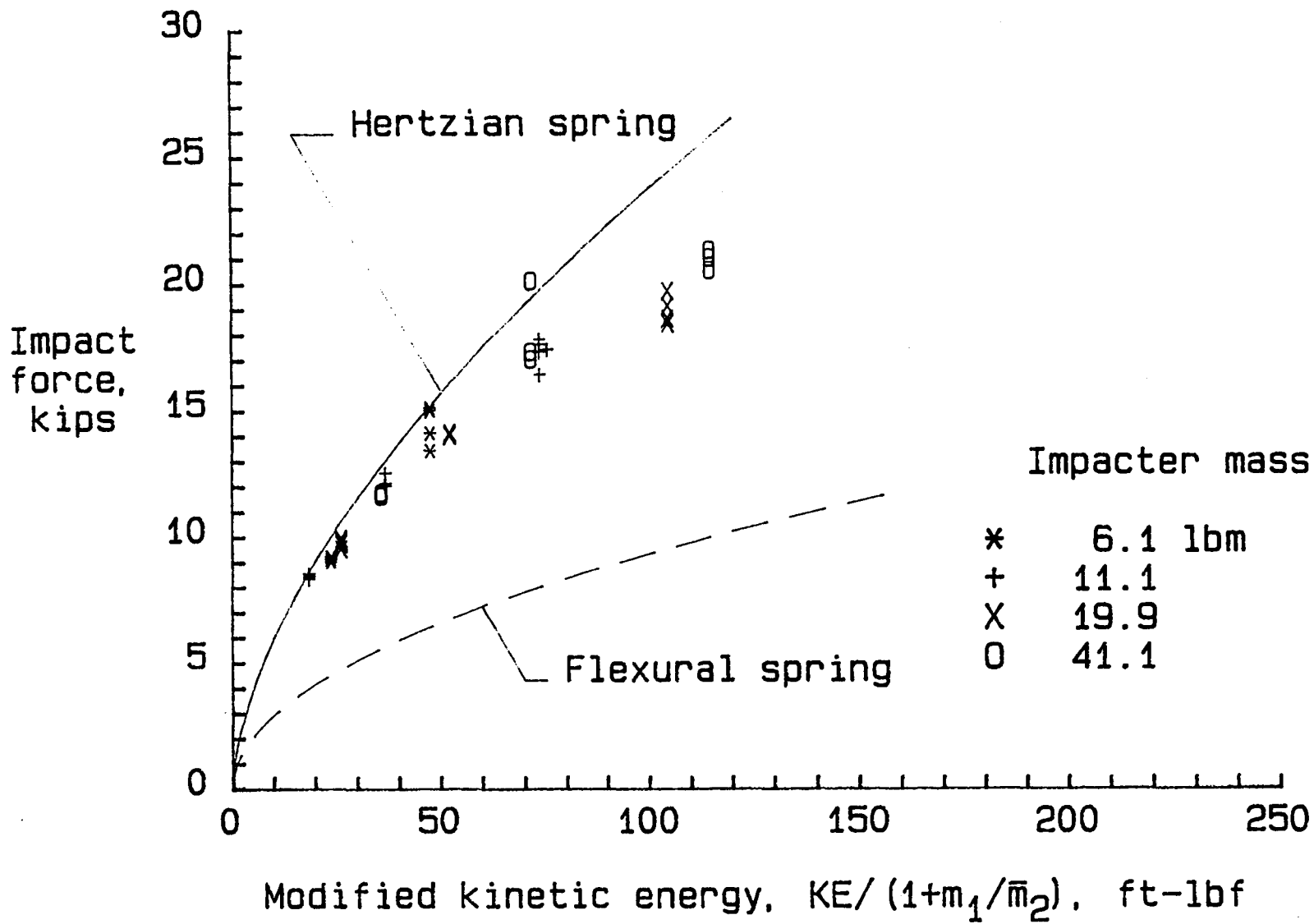


Figure 16.- Velocity ratio versus mass ratio.



(a) Filled segment, $\bar{m}_2 = 159$ lbm.

Figure 17.- Impacter force versus impacter energy.



(b) Empty segment, $\bar{m}_2 = 22$ lbm.

Figure 17.- Concluded.

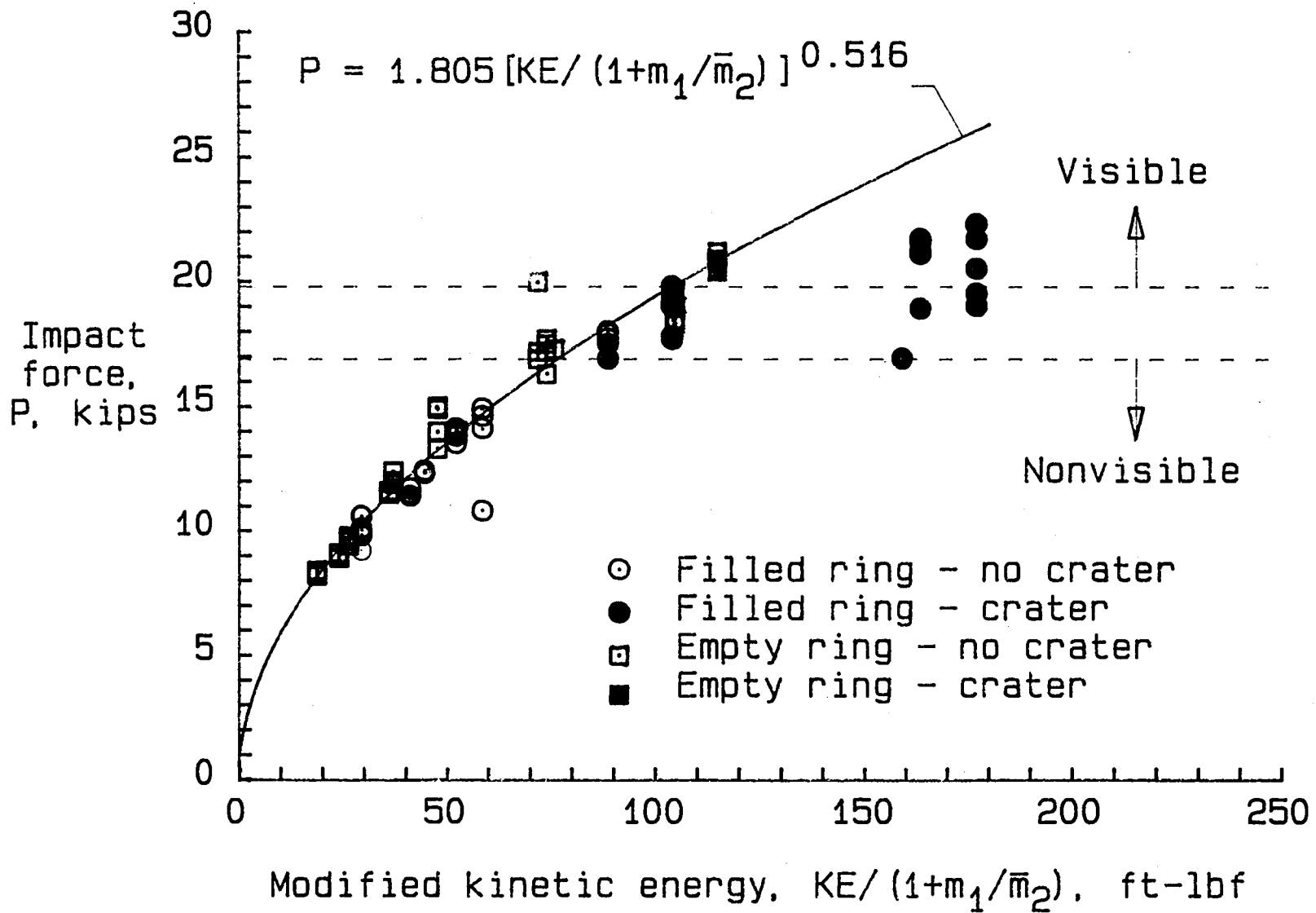


Figure 18.- Impacter force versus impacter energy for filled and empty rings.

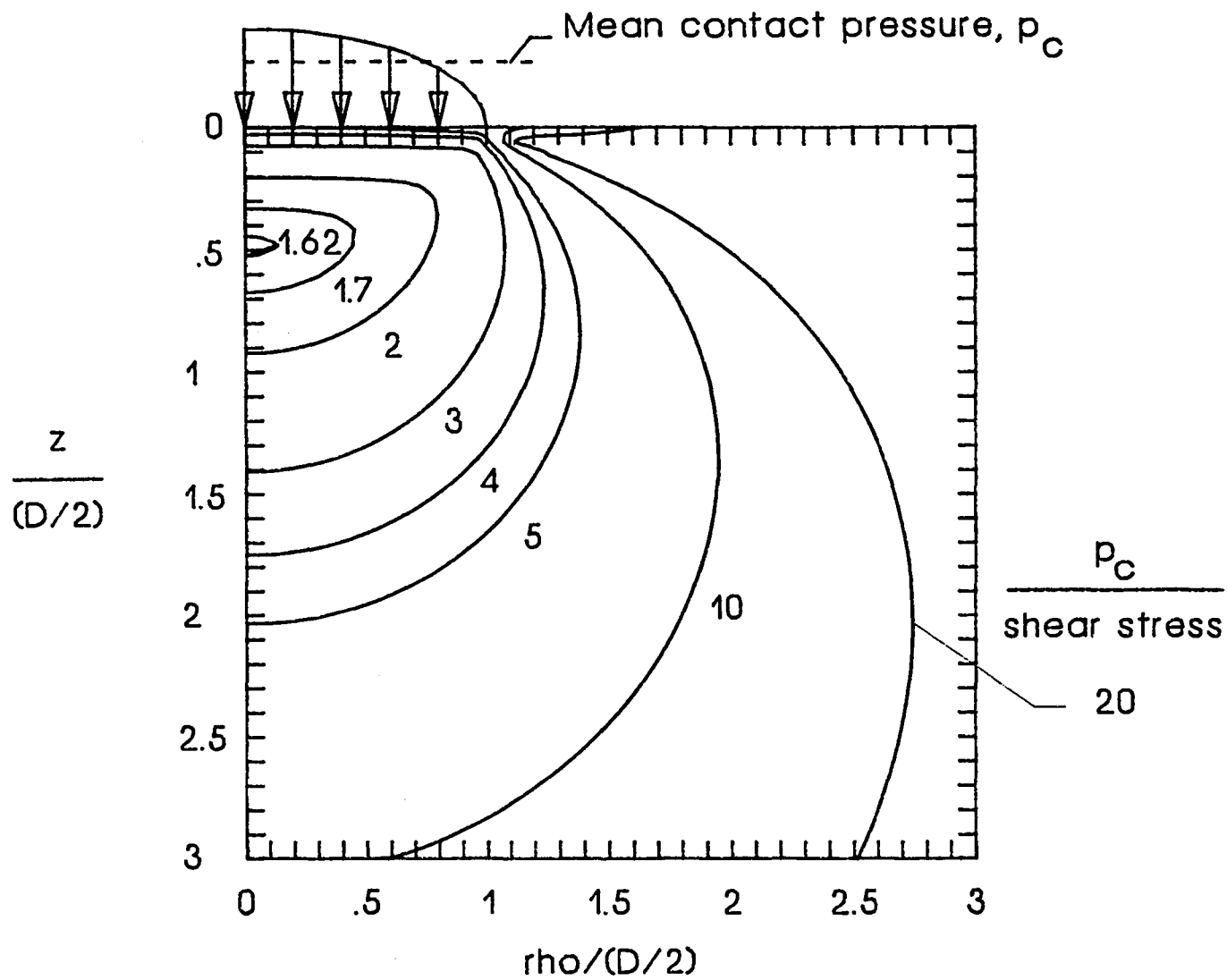


Figure 19.- Principal shear stress contours from Love's solution for hemispherical contact pressure.

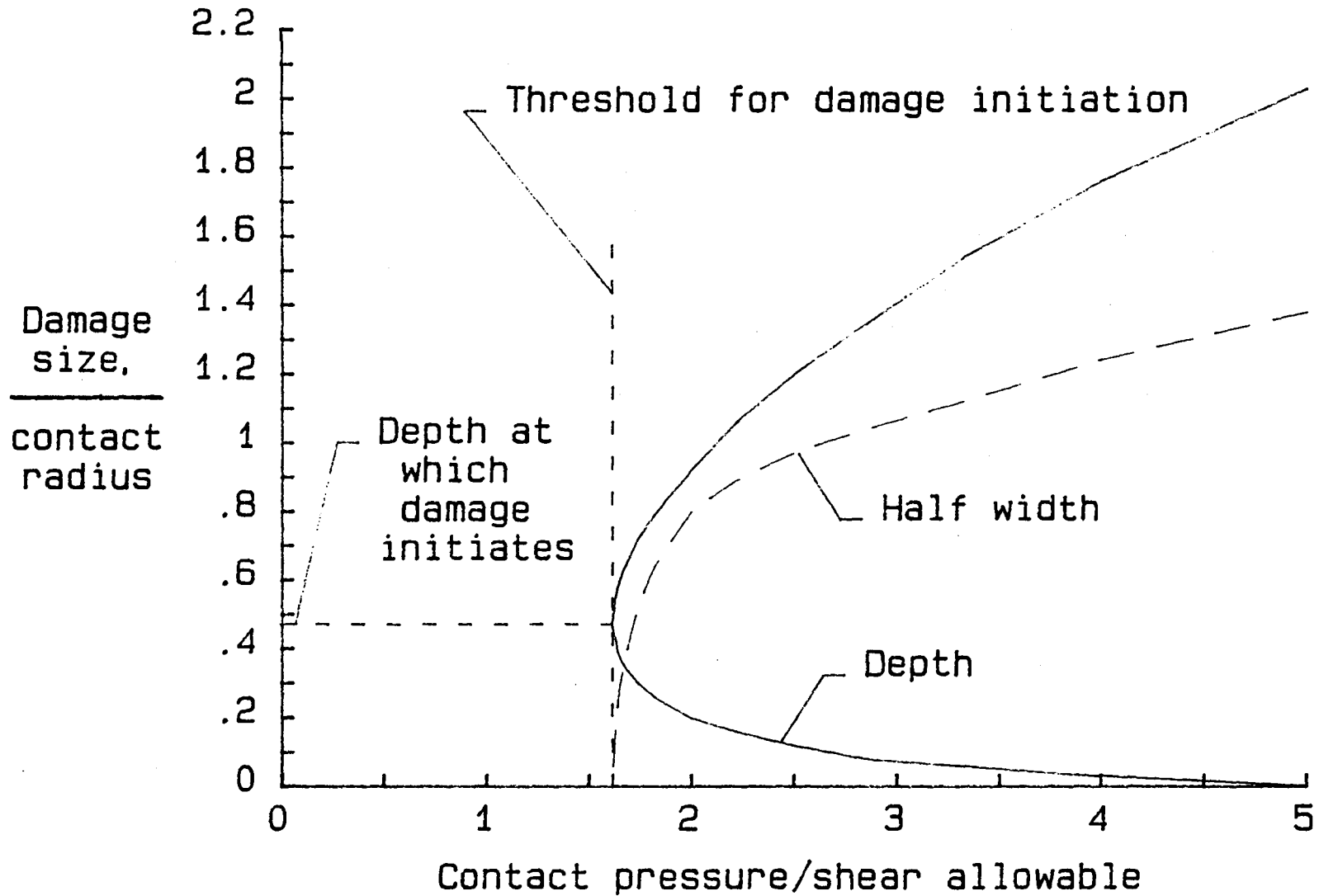


Figure 20.- Damage size versus contact pressure according to Love's solution and principal shear criterion for failure.

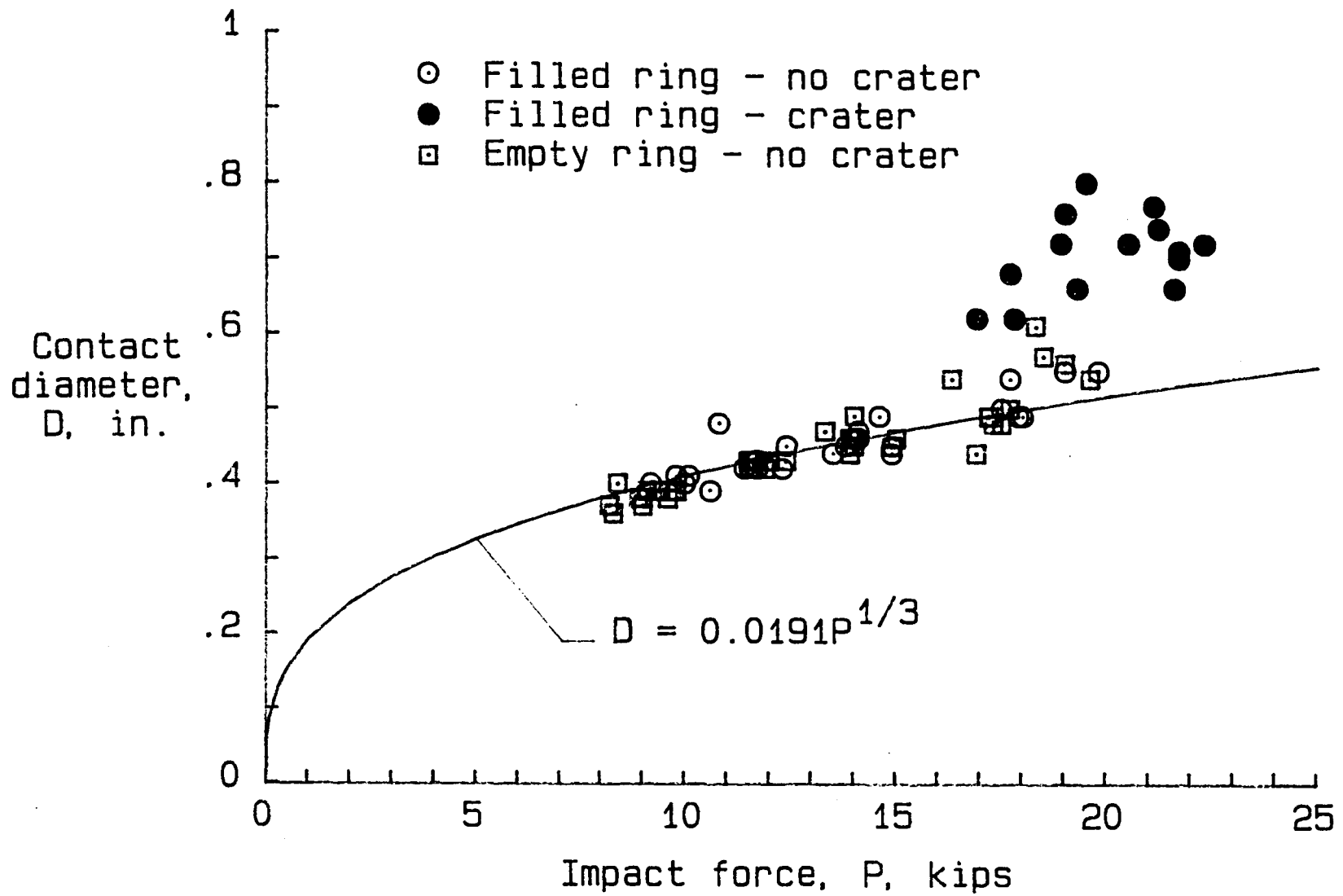


Figure 21.- Contact diameter versus impact force.

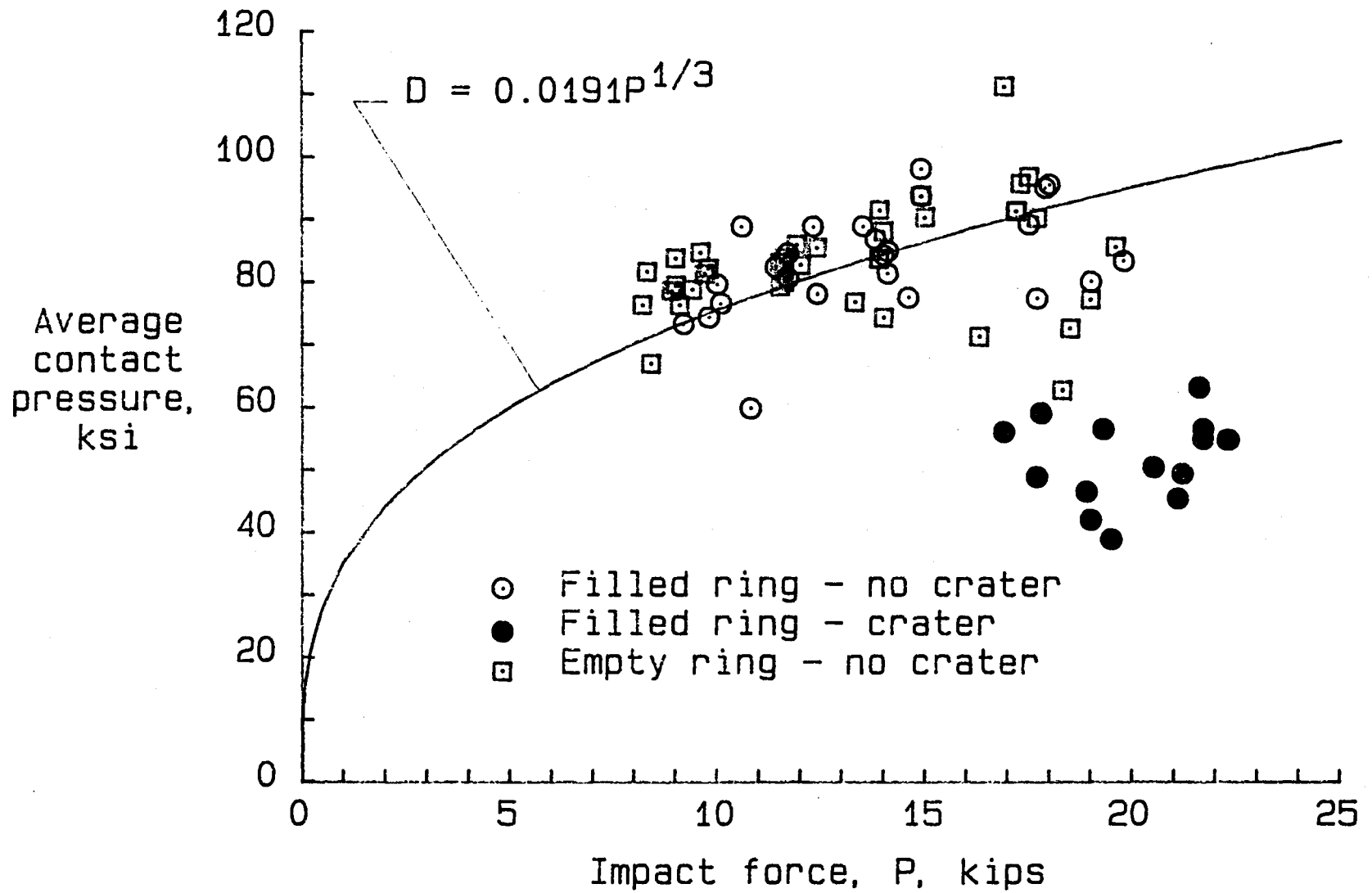
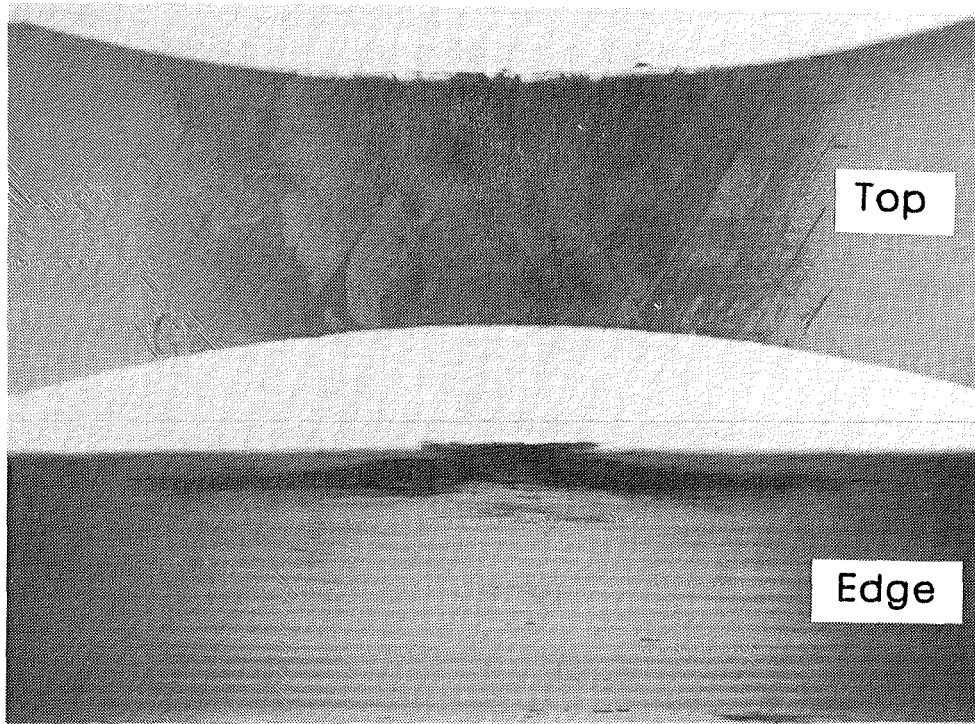
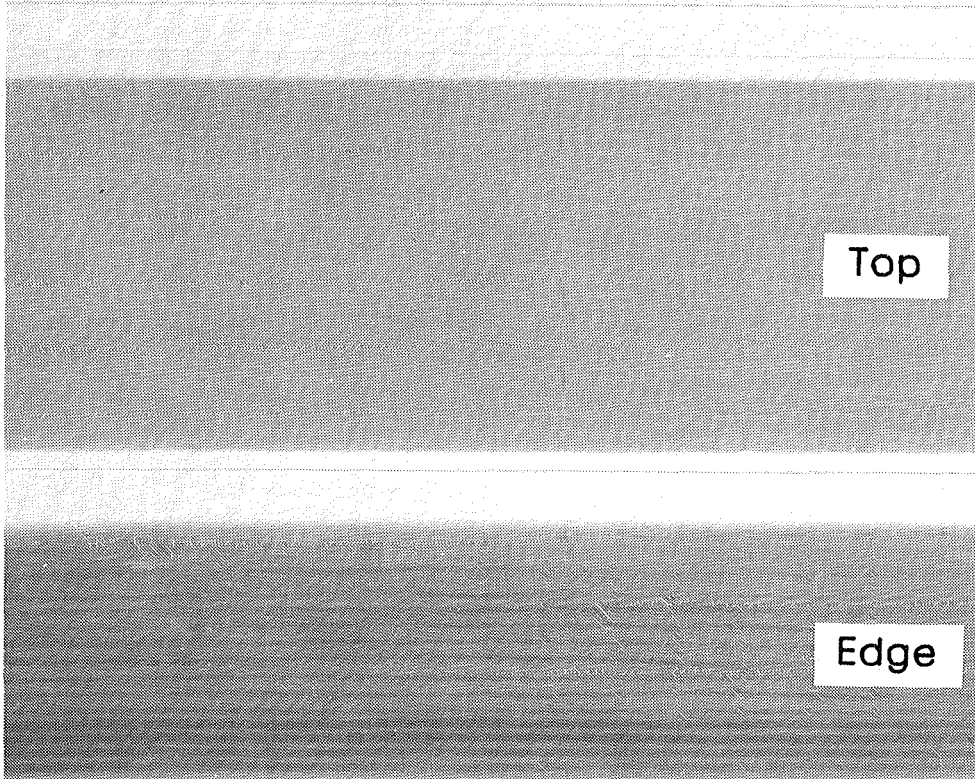


Figure 22.- Average contact pressure versus impact force.



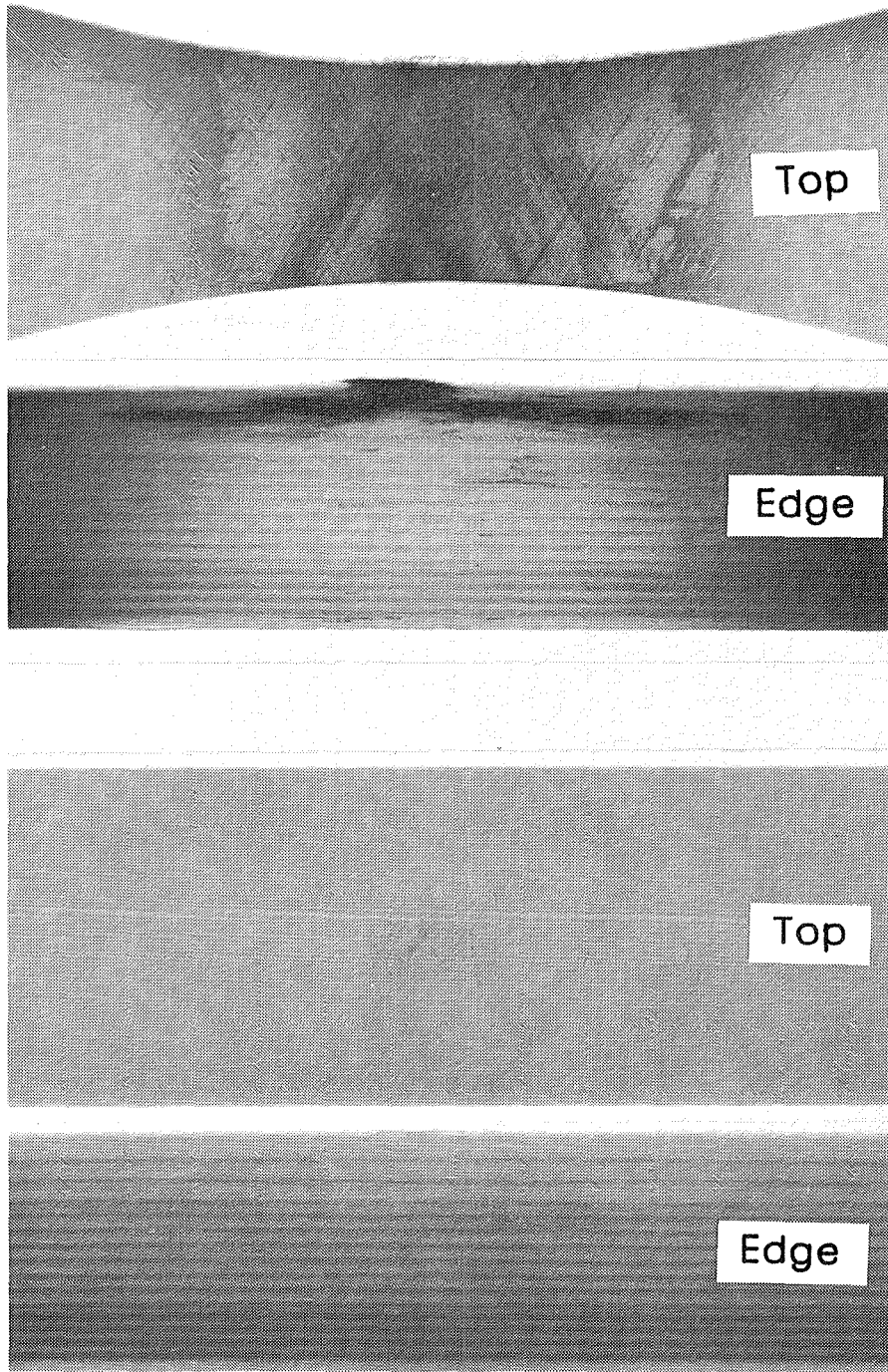
After
loading
to
1st-
ligament
failure



Before
loading

(a) Specimen 7-6 (P = 9.2 kips).

Figure 24.- Radiographs of first-ligament failure - filled ring.

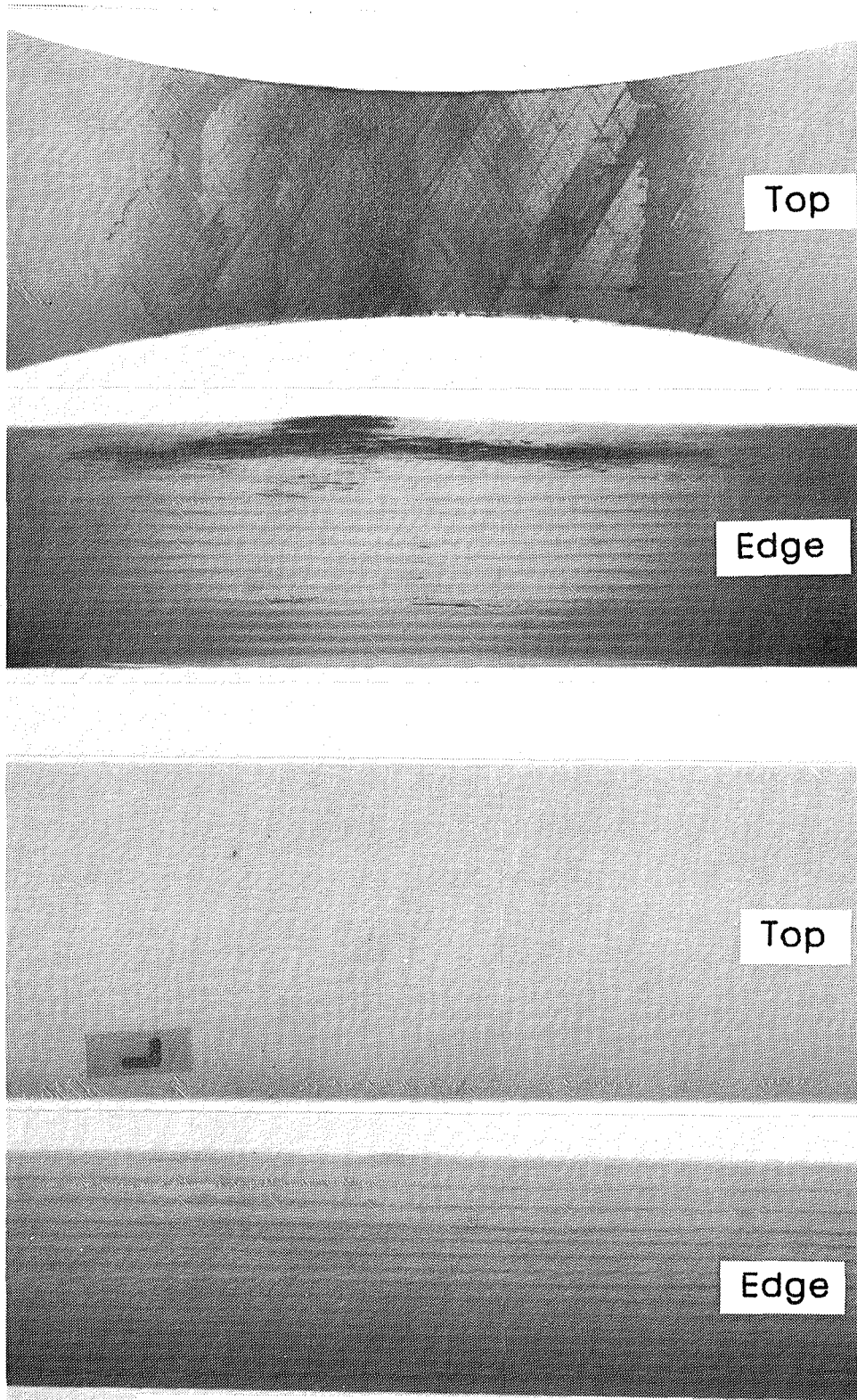


After
loading
to
1st-
ligament
failure

Before
loading

(b) Specimen 7-27 (P = 14.6 kips).

Figure 24.- Continued.

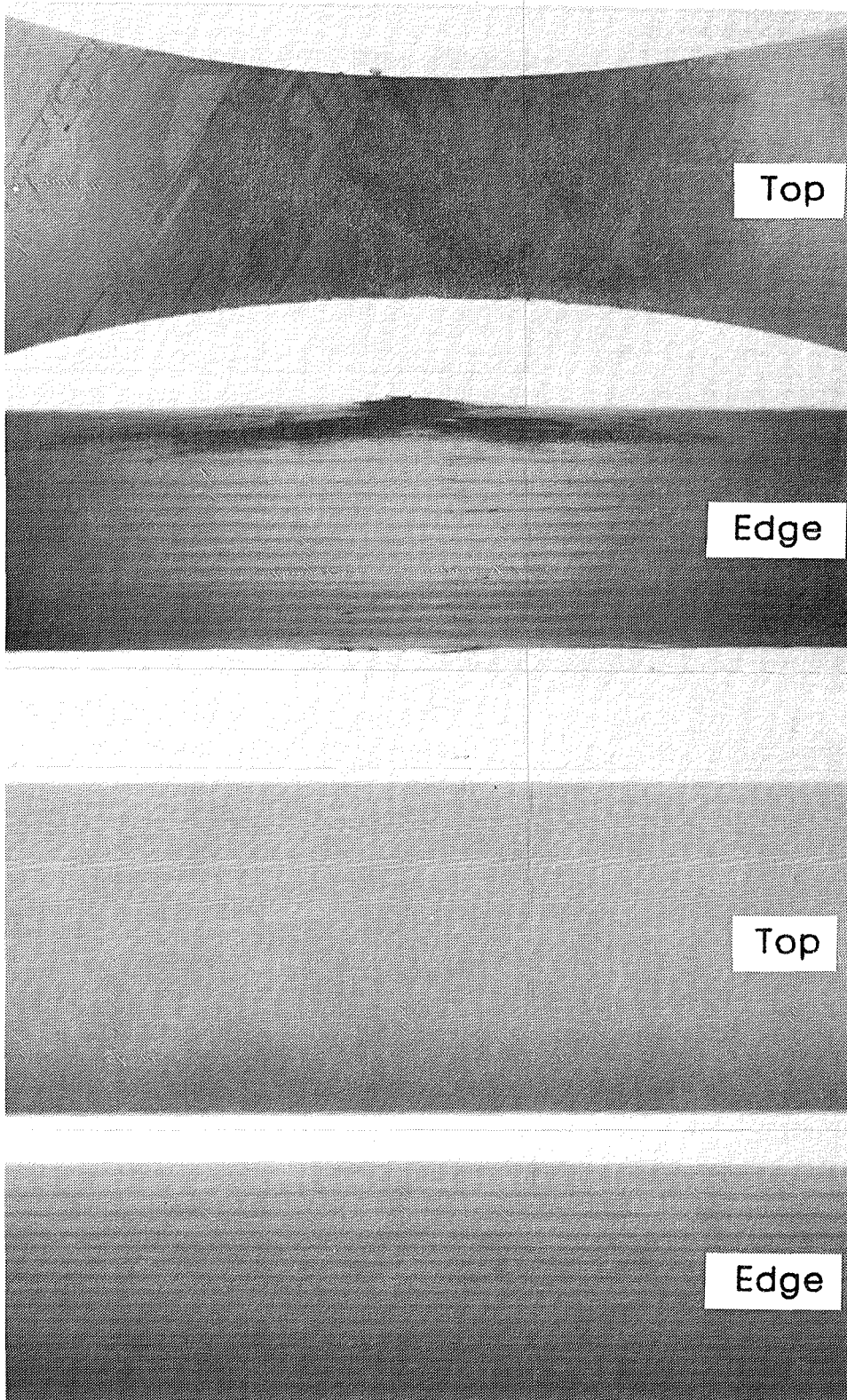


After
loading
to
1st-
ligament
failure

Before
loading

(c) Specimen 7-7 (P = 13.5 kips).

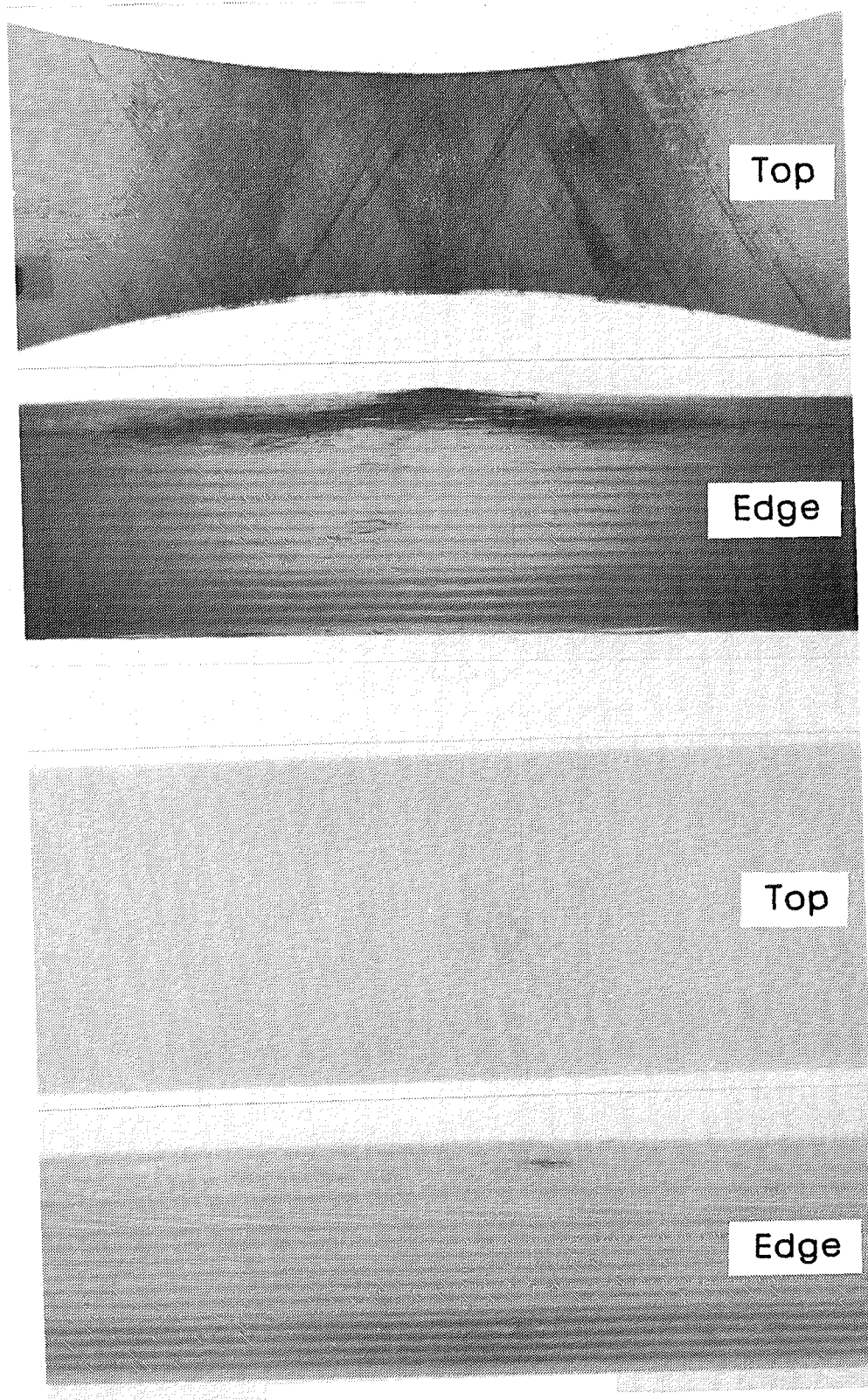
Figure 24.- Continued.



After
loading
to
1st-
ligament
failure

Before
loading

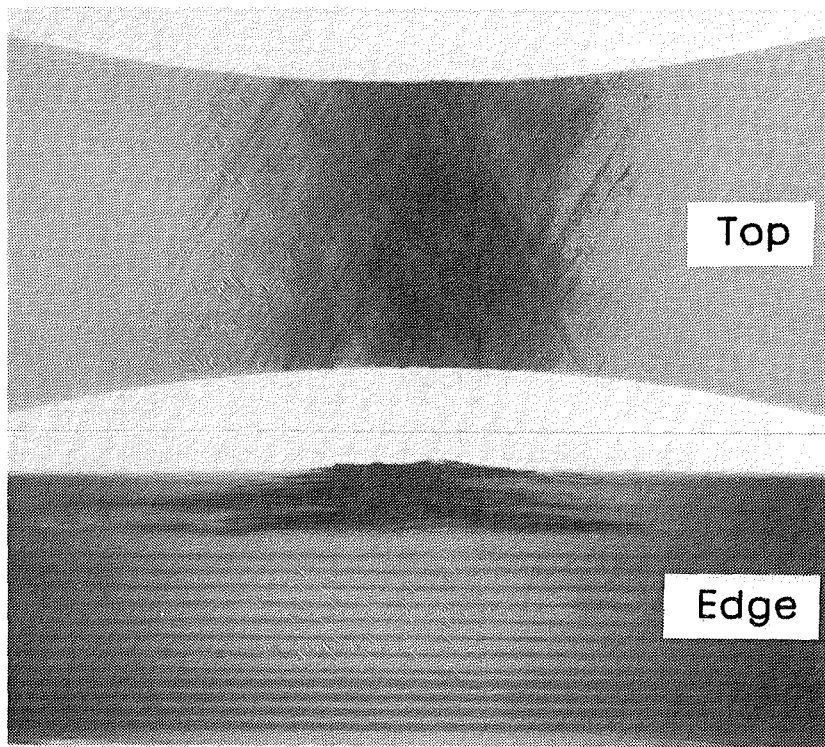
(d) Specimen 7-1.



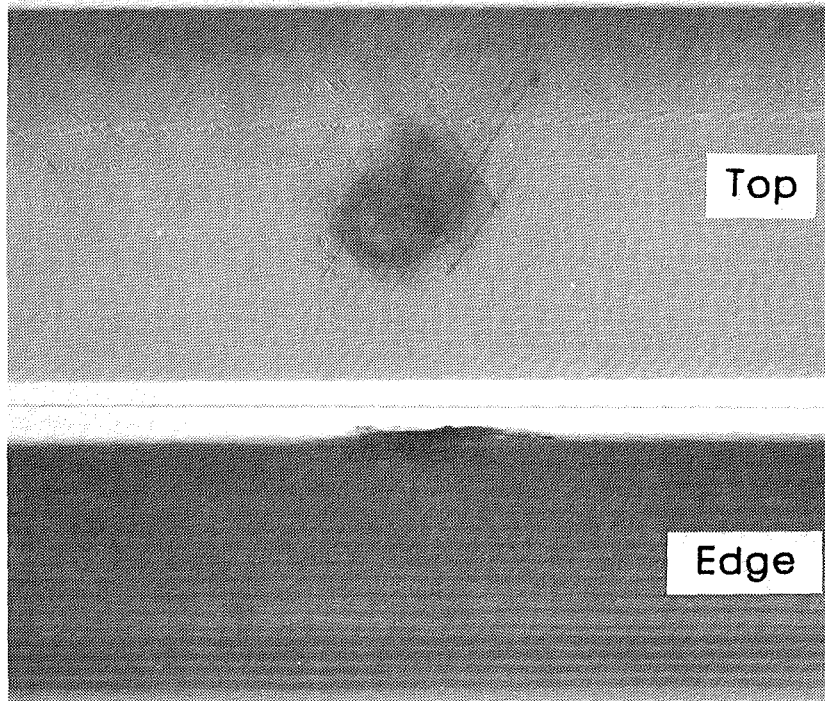
After loading to 1st-ligament failure

Before loading

(e) Specimen 7-13.



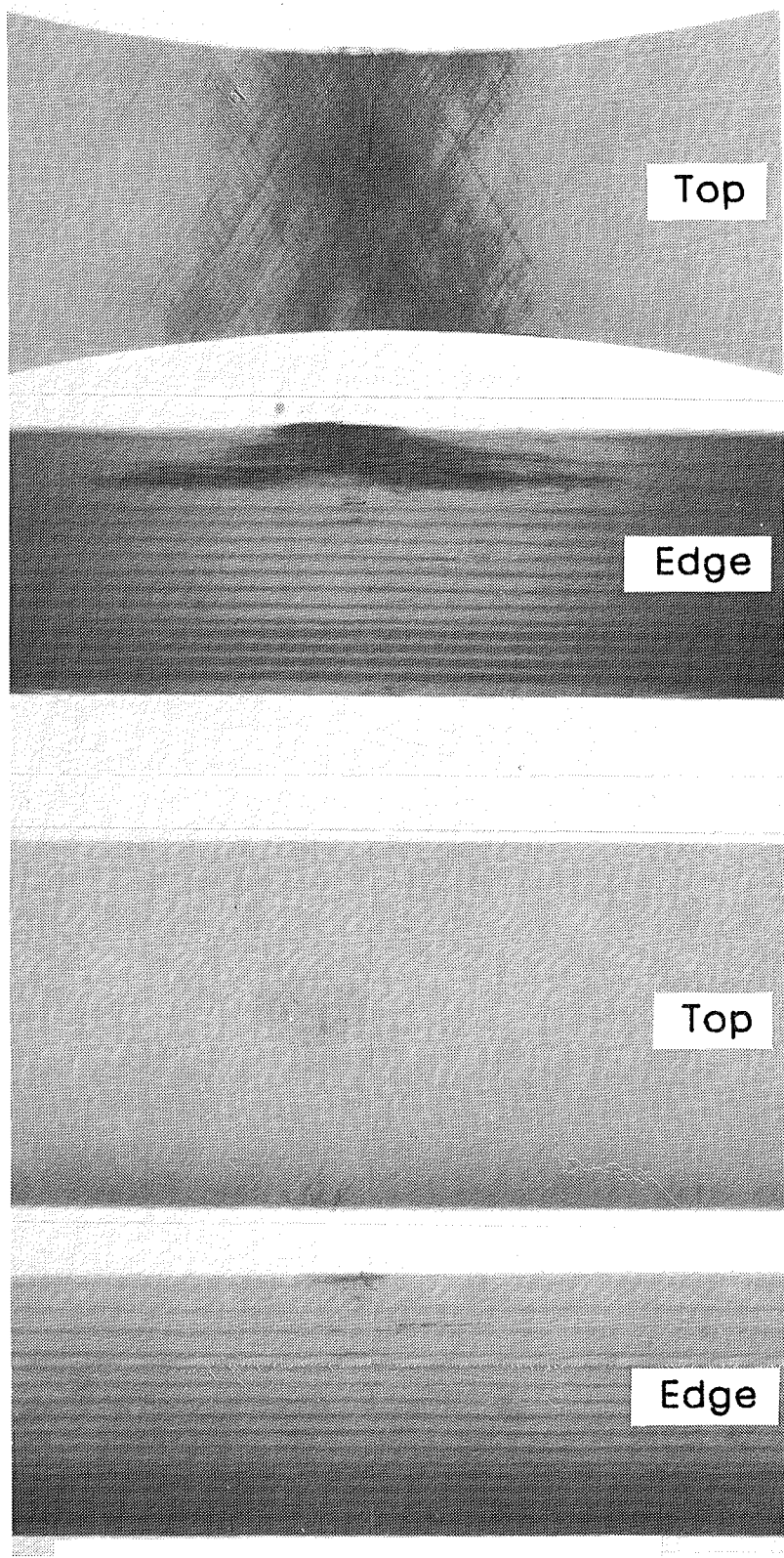
After
loading
to
1st-
ligament
failure



Before
loading

(f) Specimen 7-8 (P = 17.8 kips).

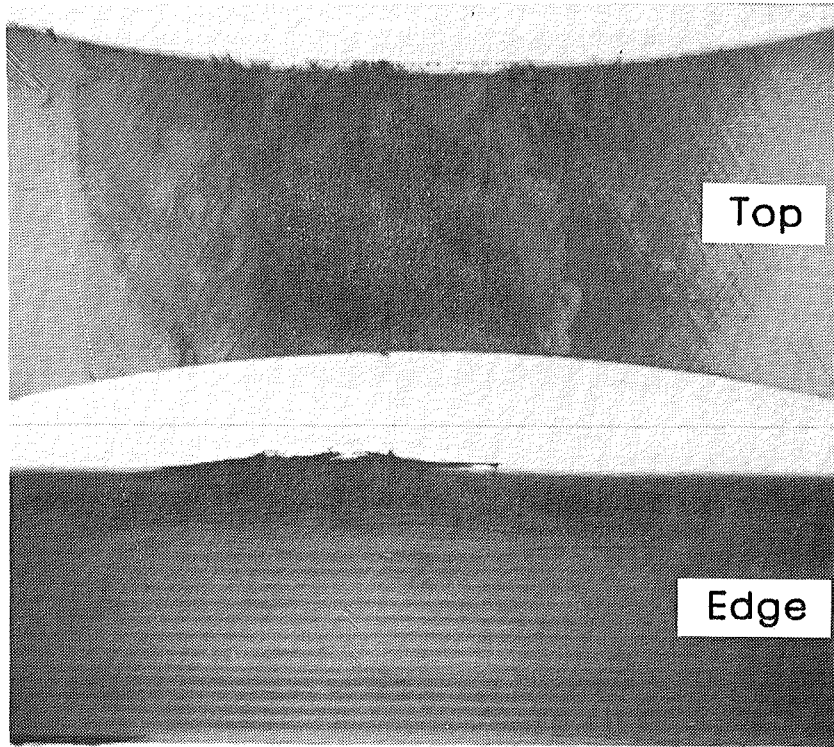
Figure 24.- Continued.



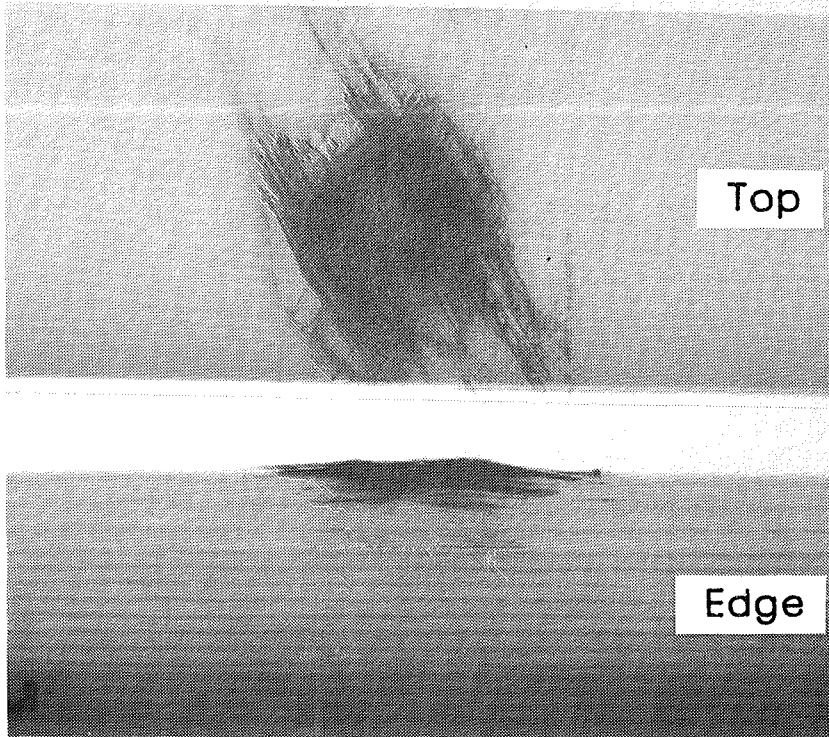
After loading to 1st-ligament failure

Before loading

(g) Specimen 7-2 (P = 17.9 kips).

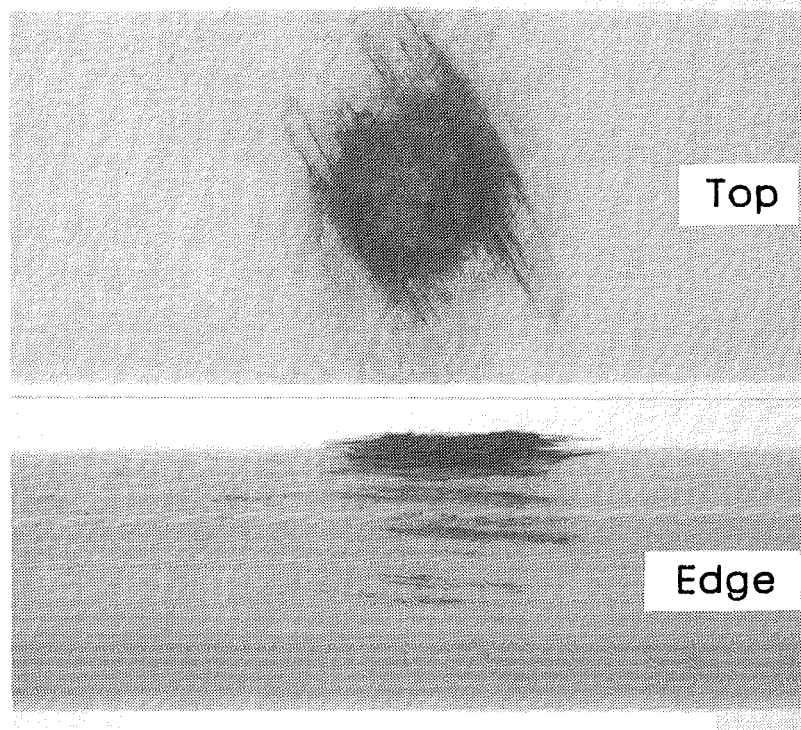
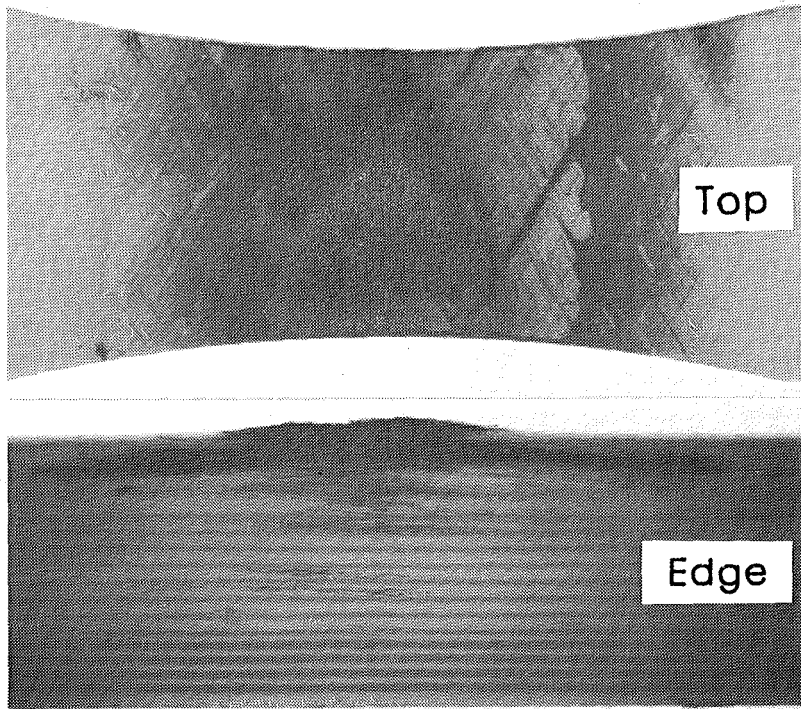


After
loading
to
1st-
ligament
failure



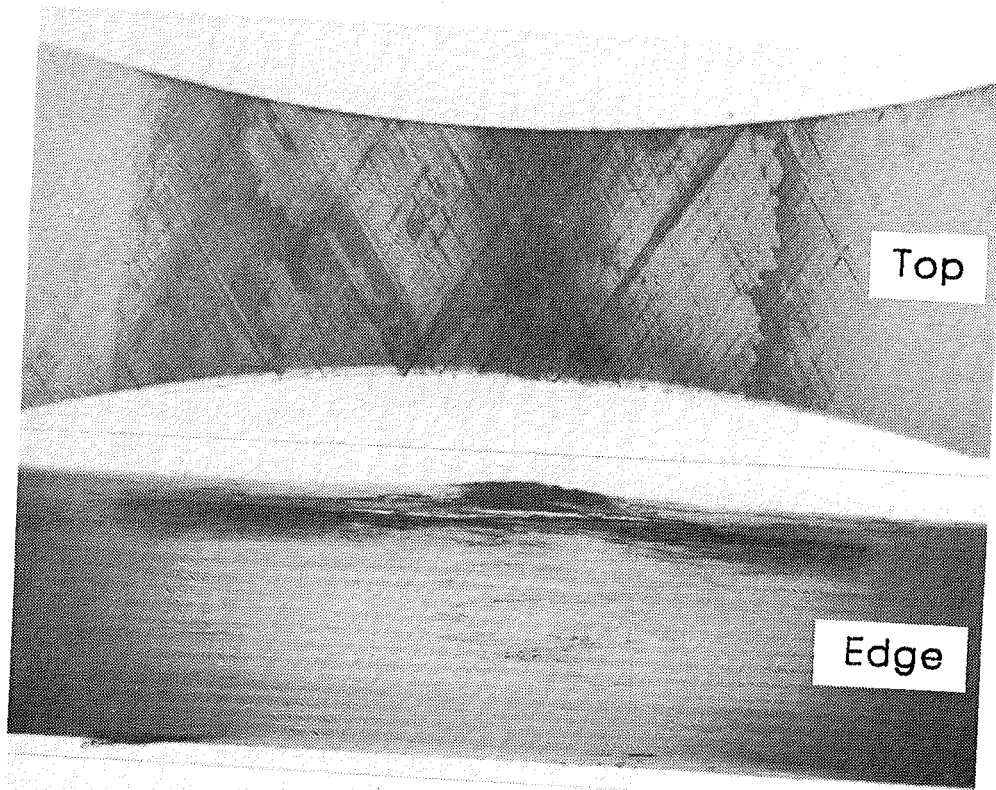
Before
loading

(h) Specimen 7-12 (P = 21.7 kips).

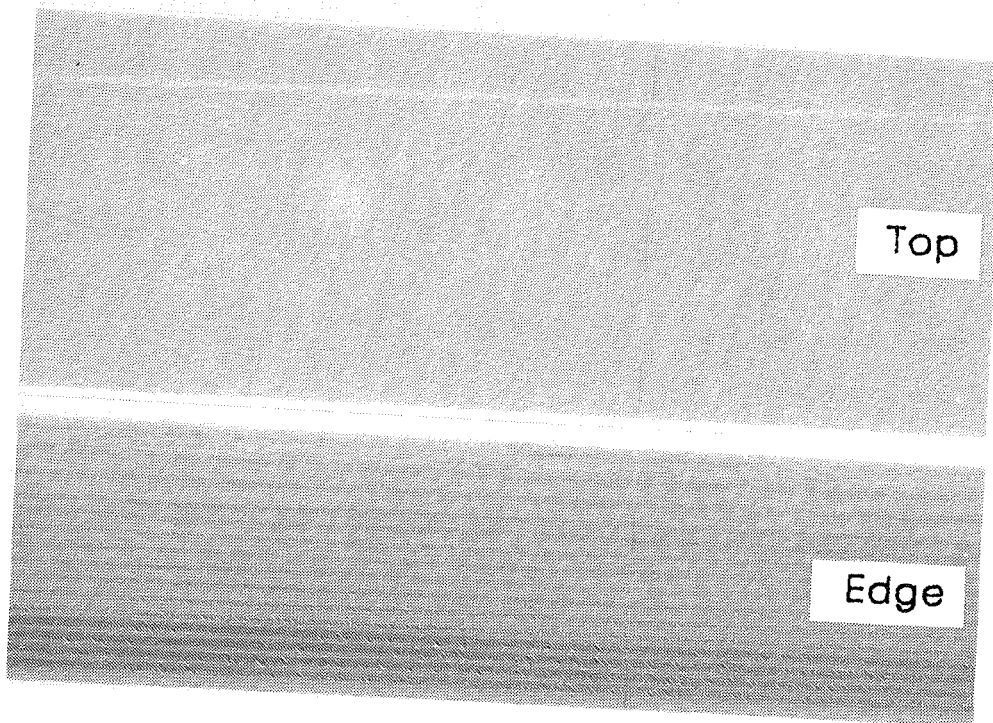


(i) Specimen 7-14 (P = 21.2 kips).

Figure 24.- Concluded.



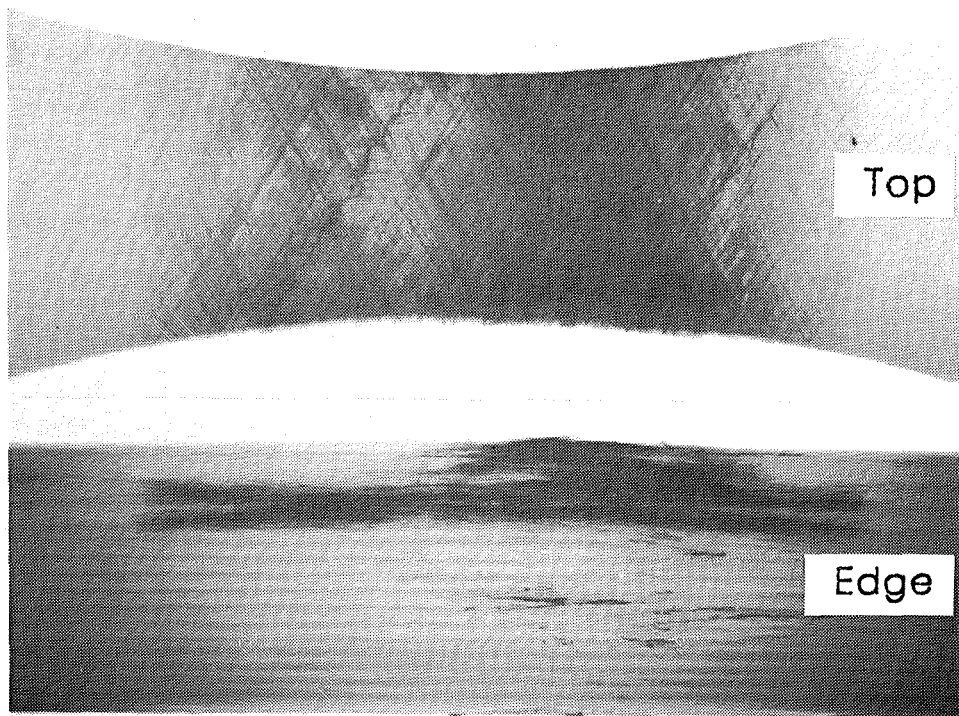
After
loading
to
1st-
ligament
failure



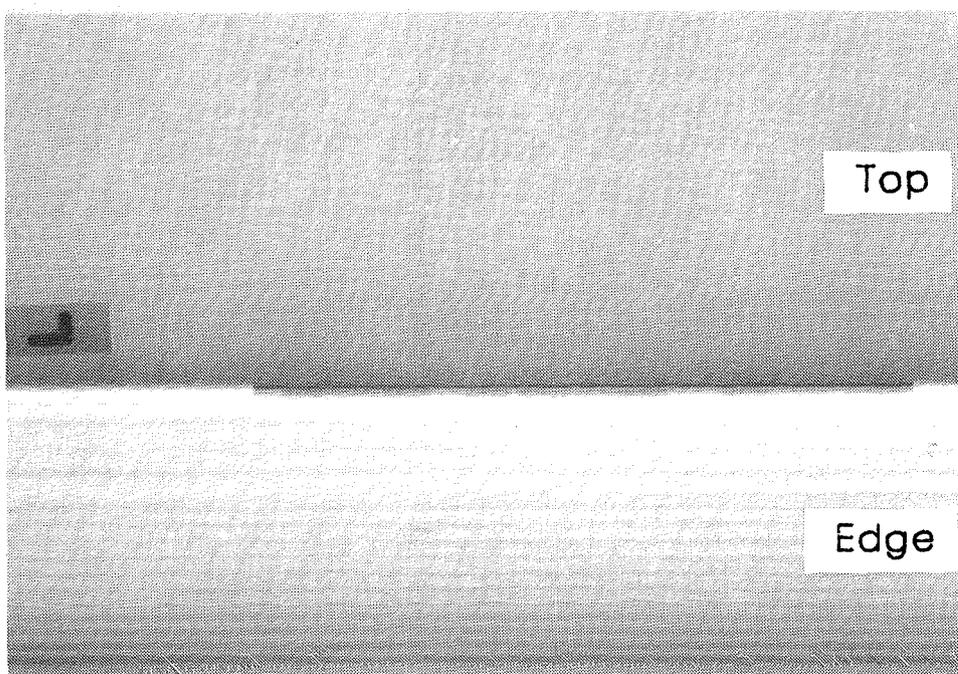
Before
loading

(a) Specimen 5-26 (P = 8.9 kips).

Figure 25.- Radiographs of first-ligament failure - empty ring.

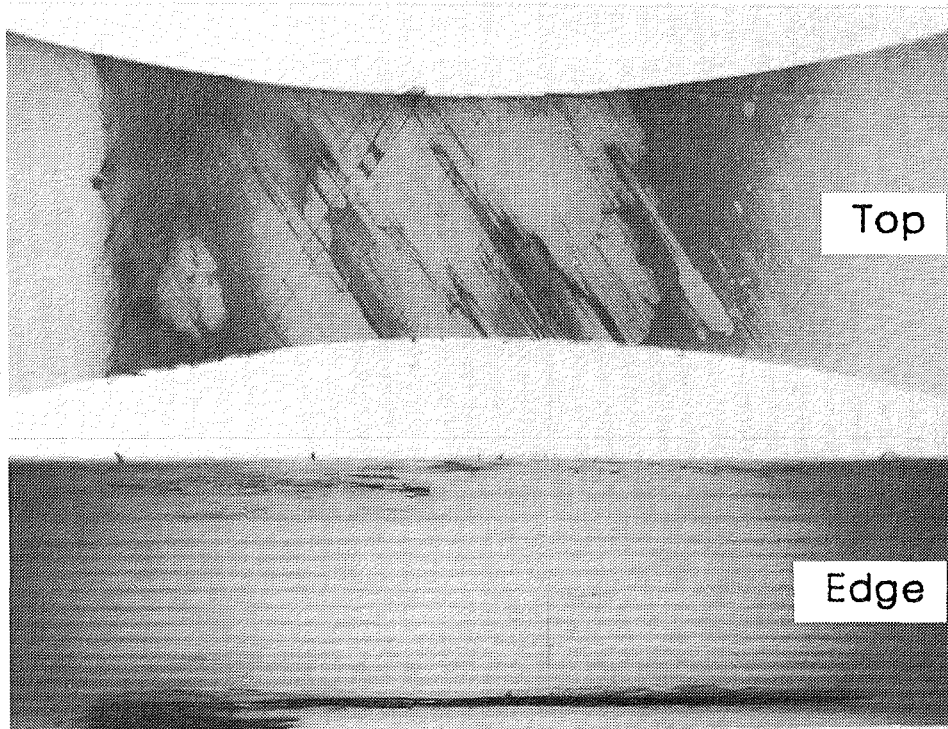


After
loading
to
1st-
ligament
failure



Before
loading

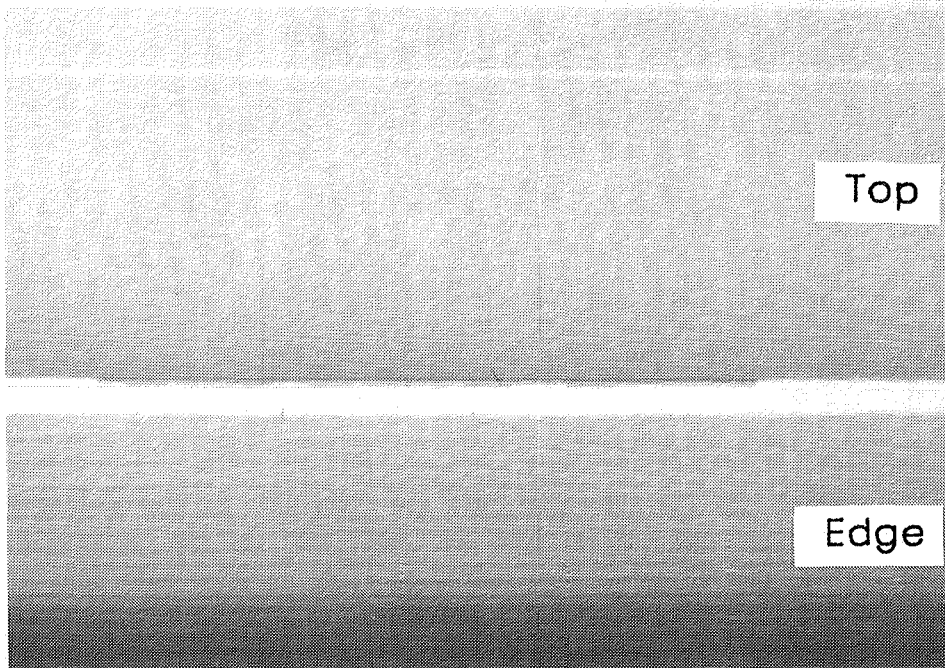
(b) Specimen 5-5 (P = 8.3 kips).



Top

Edge

After
loading
to
1st-
ligament
failure

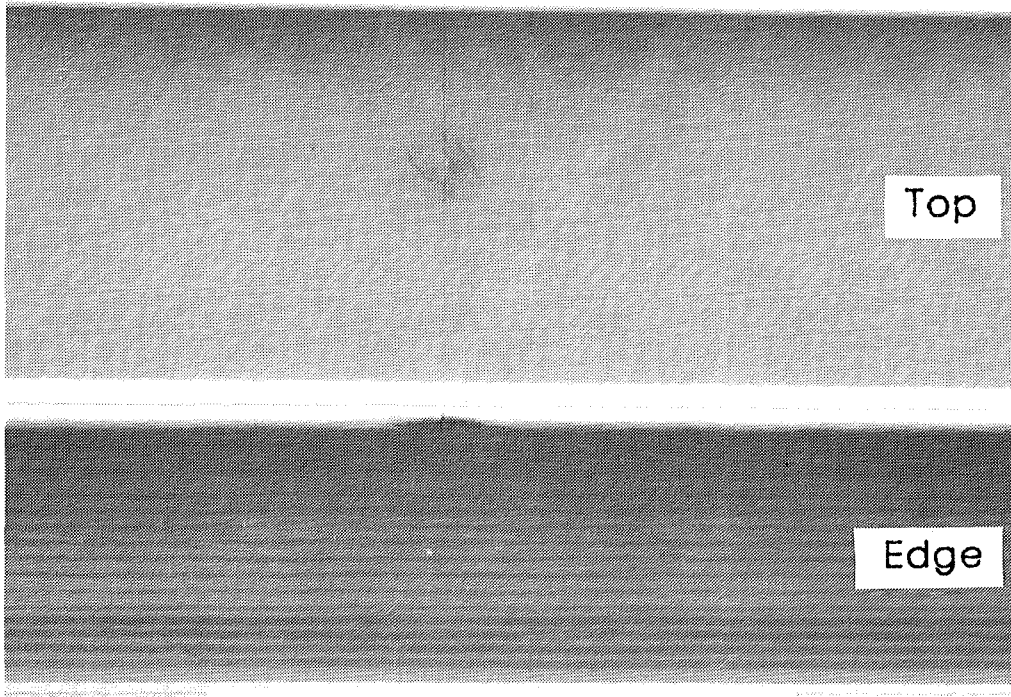
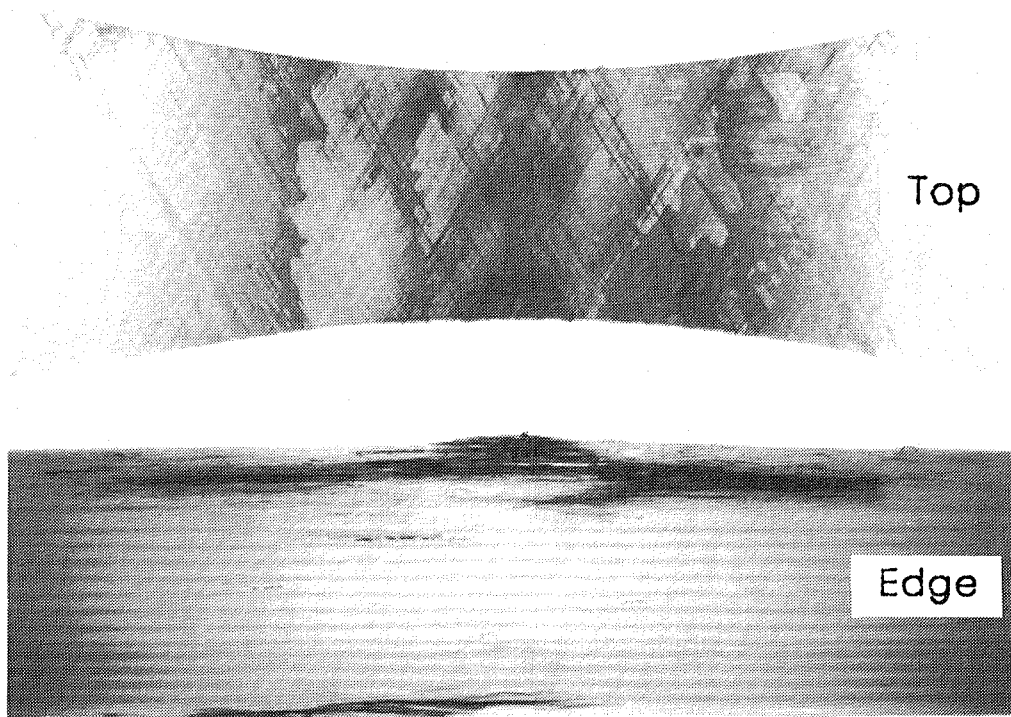


Top

Edge

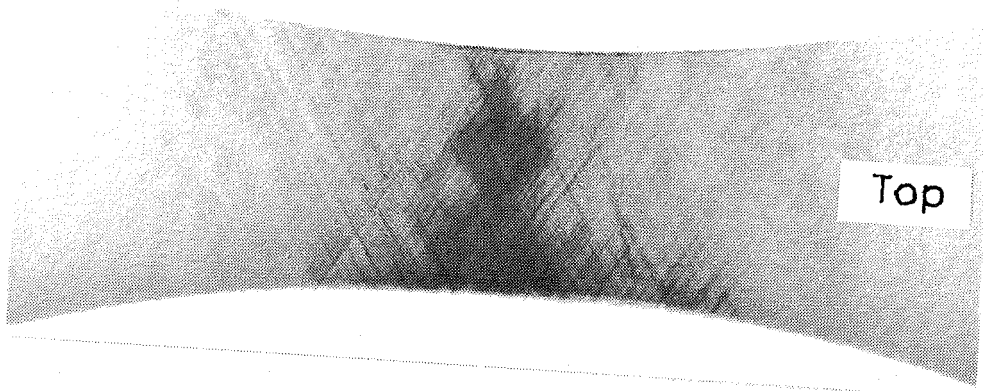
Before
loading

(c) Specimen 5-17 (P = 8.4 kips).

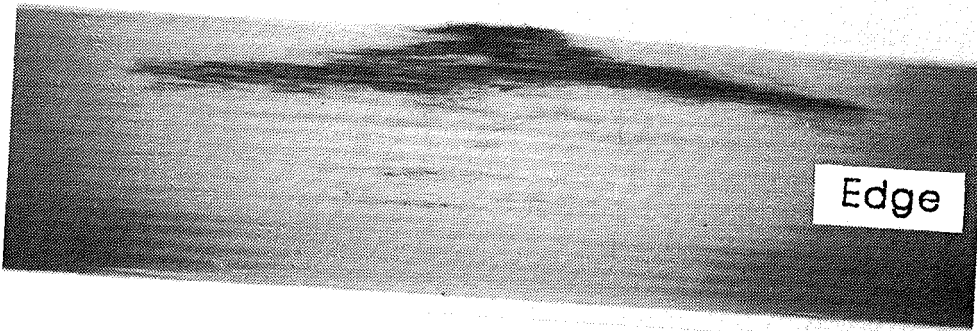


(d) Specimen 5-16 (P = 14.9 kips).

Figure 25.- Continued.



Top

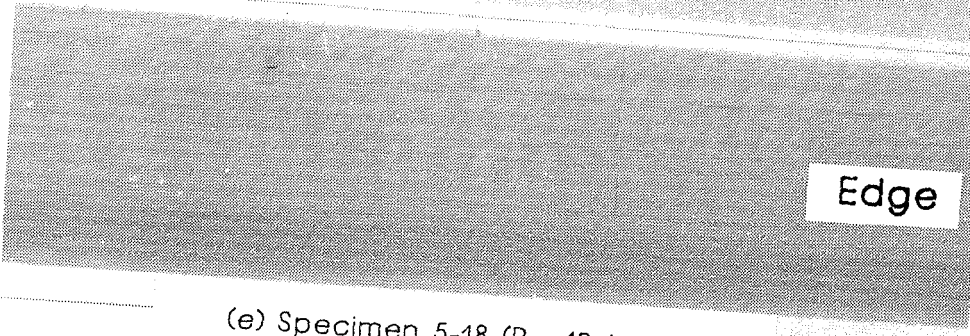


Edge

After
loading
to
1st-
ligament
failure



Top

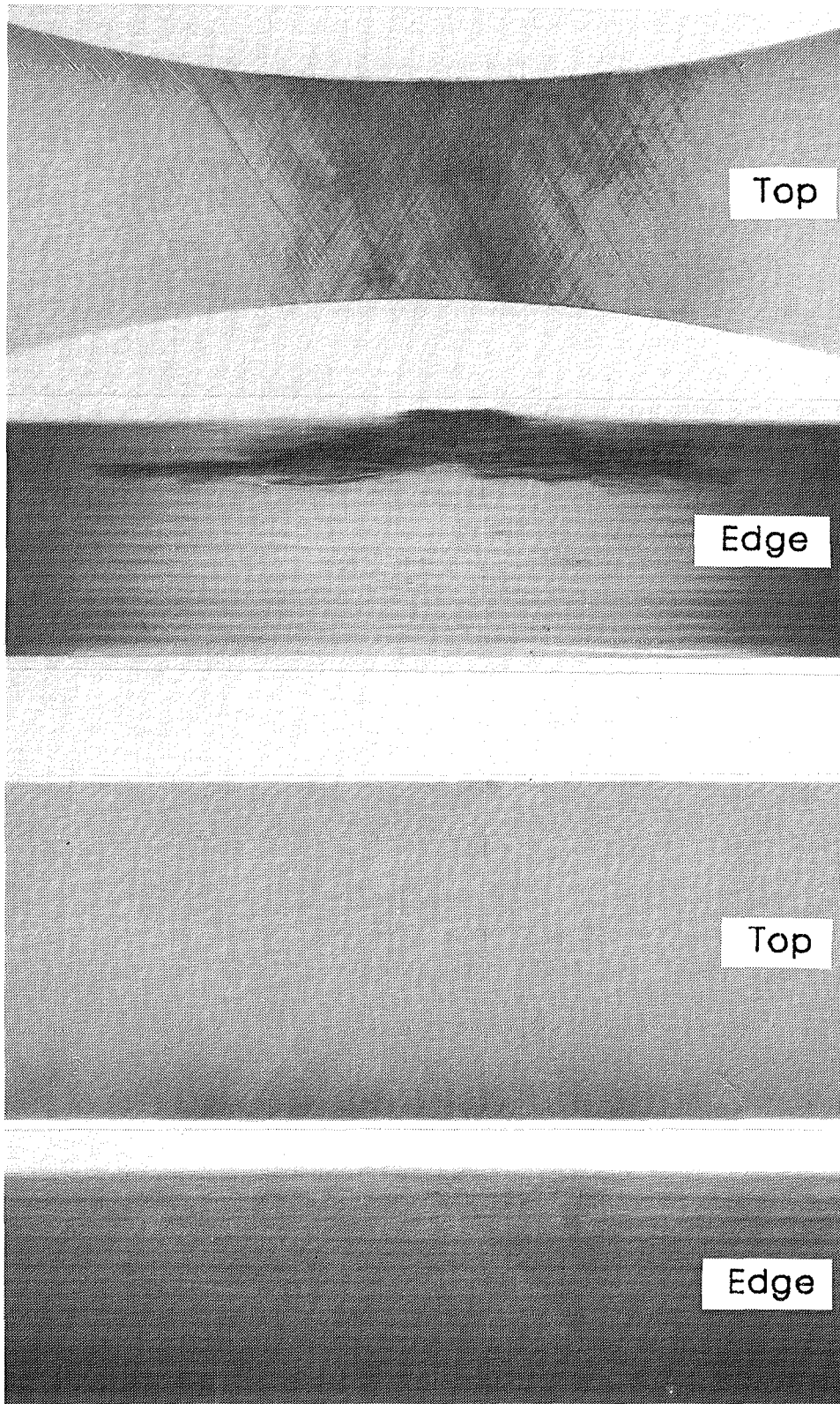


Edge

Before
loading

(e) Specimen 5-18 (P = 12.4 kips).

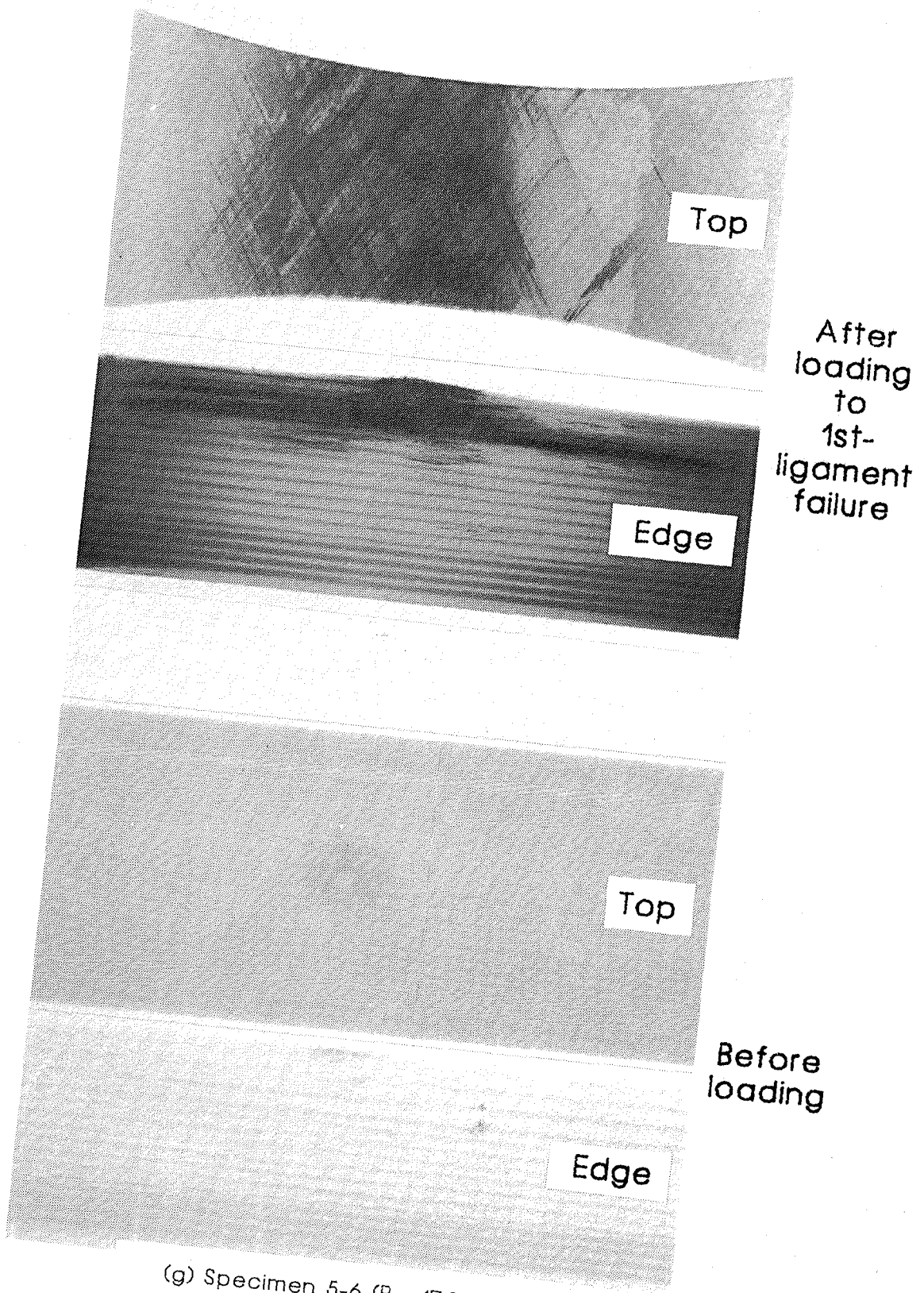
Figure 25.- Continued.



After
loading
to
1st-
ligament
failure

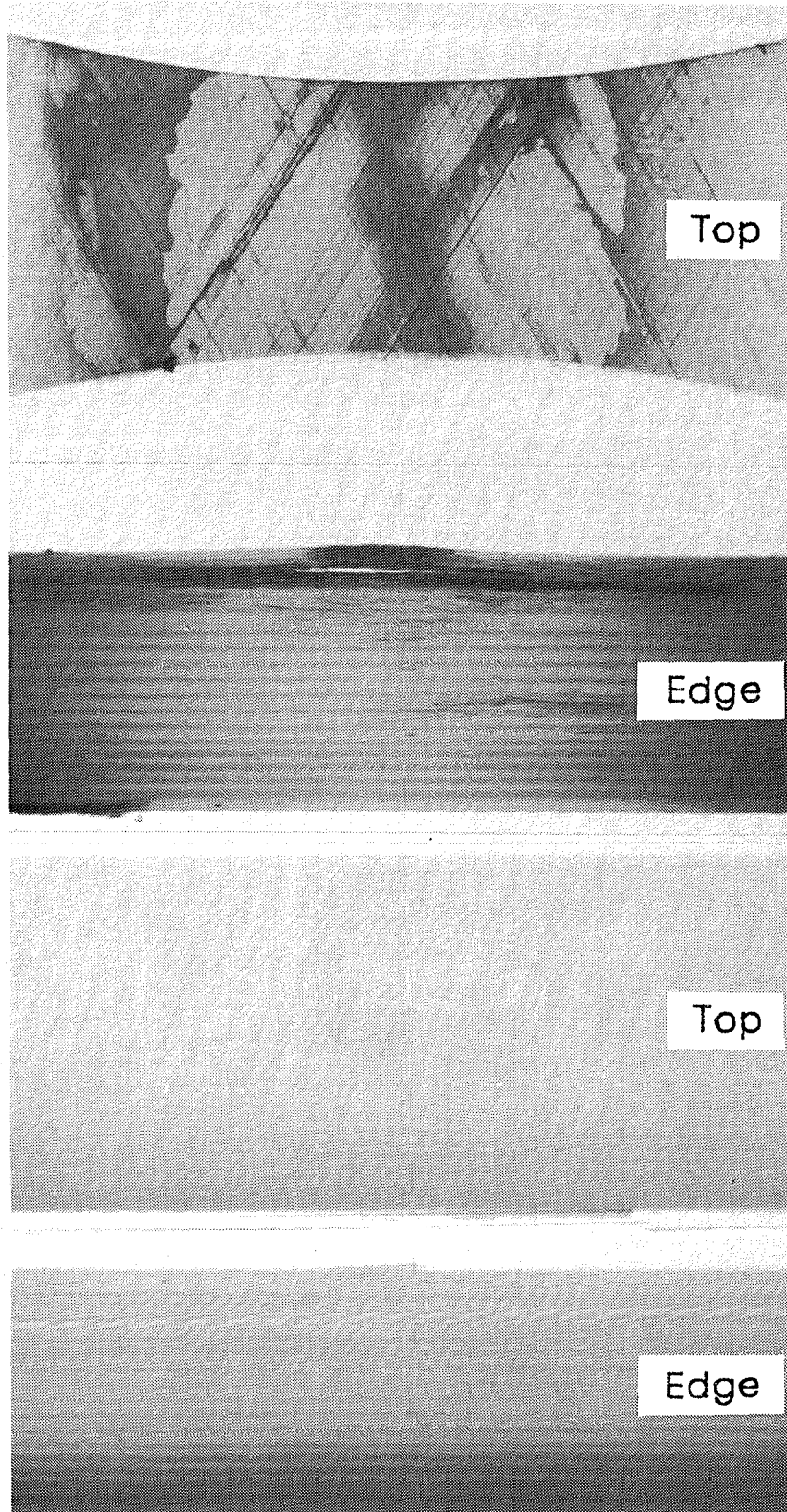
Before
loading

(f) Specimen 5-41 (P = 9.7 kips).



(g) Specimen 5-6 (P = 17.2 kips).

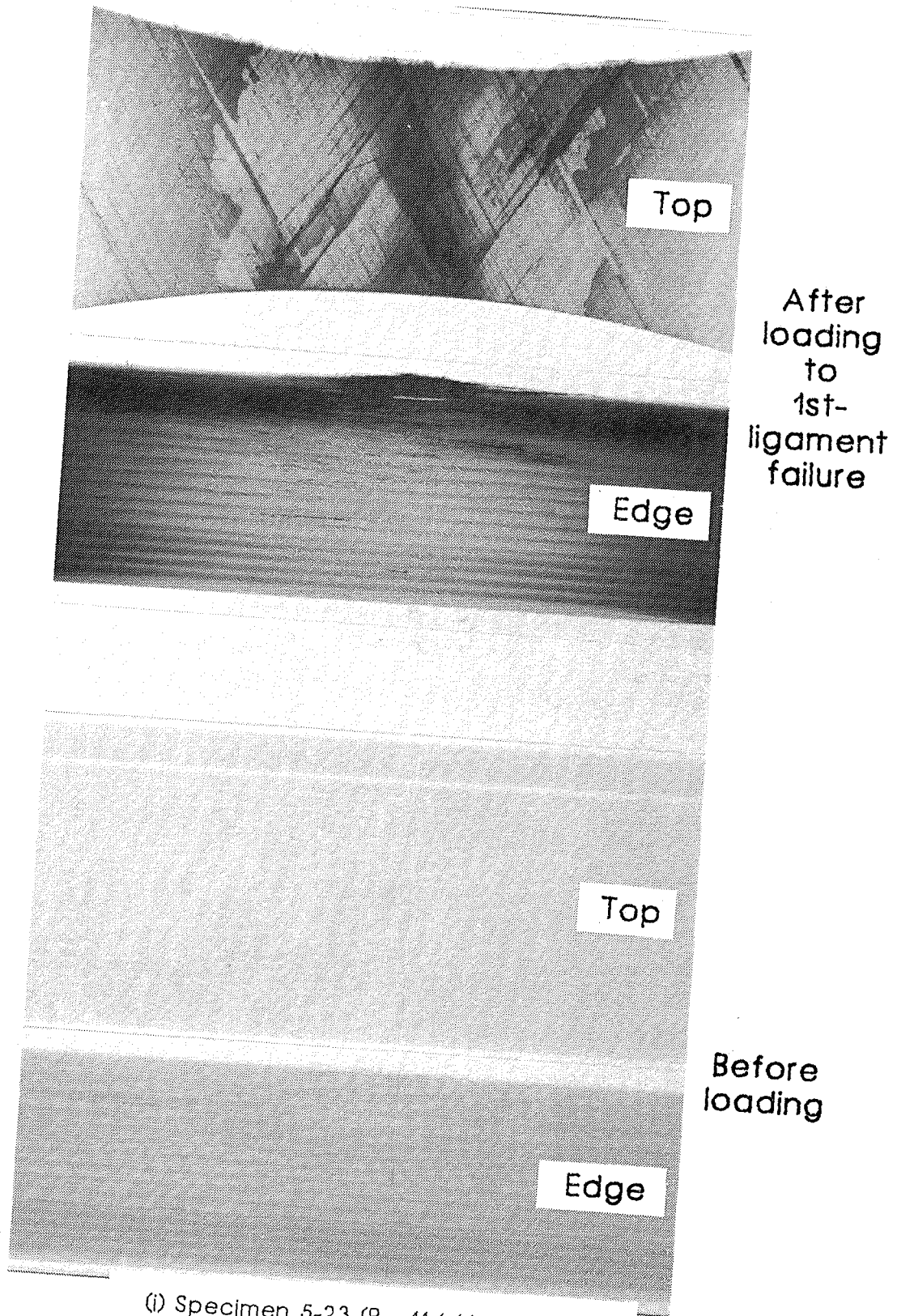
Figure 25.- Continued.



After
loading
to
1st-
ligament
failure

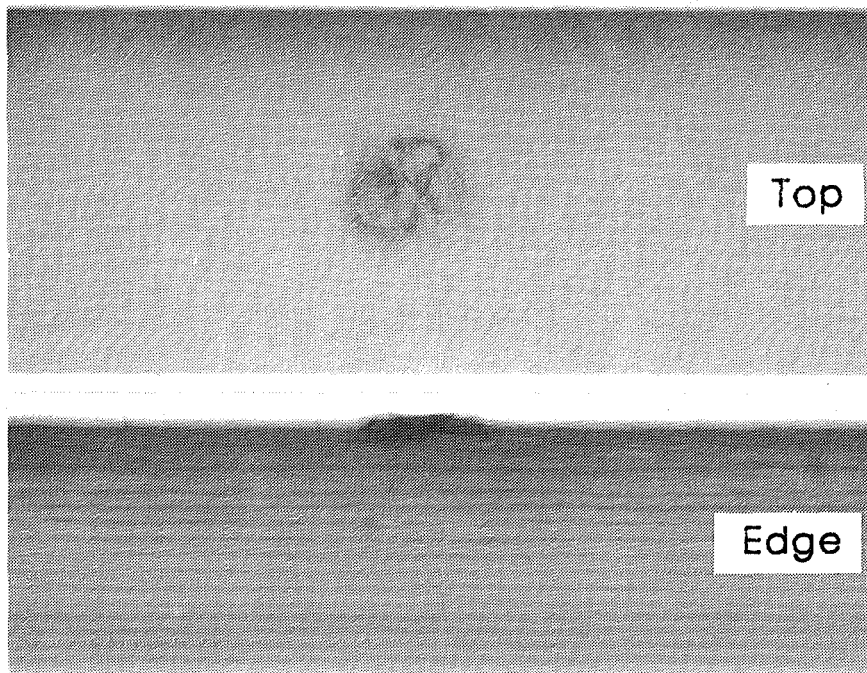
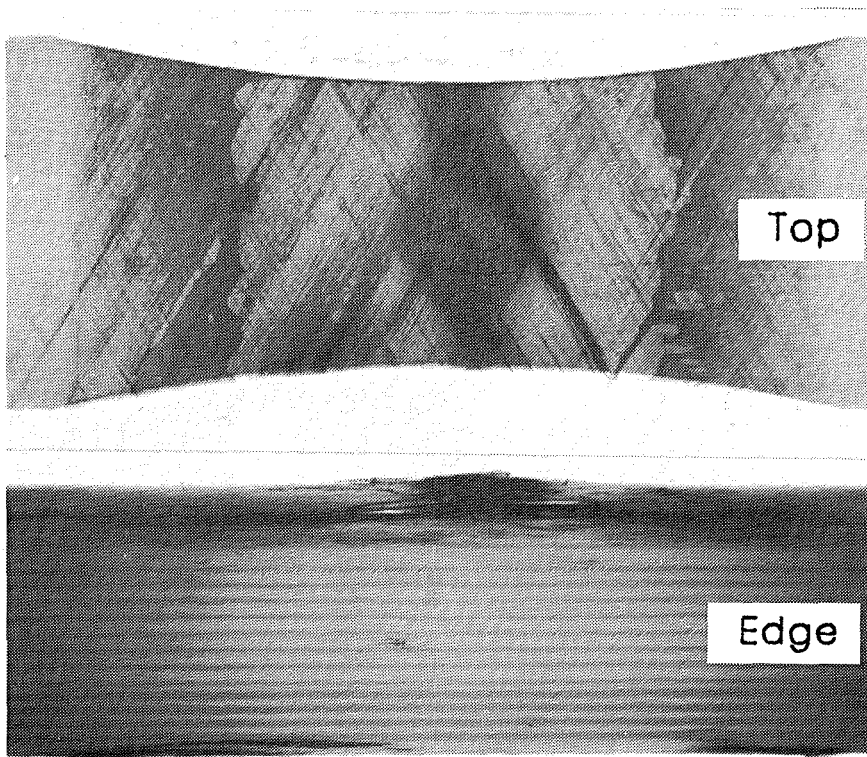
Before
loading

(h) Specimen 5-21 (P = 13.9 kips).



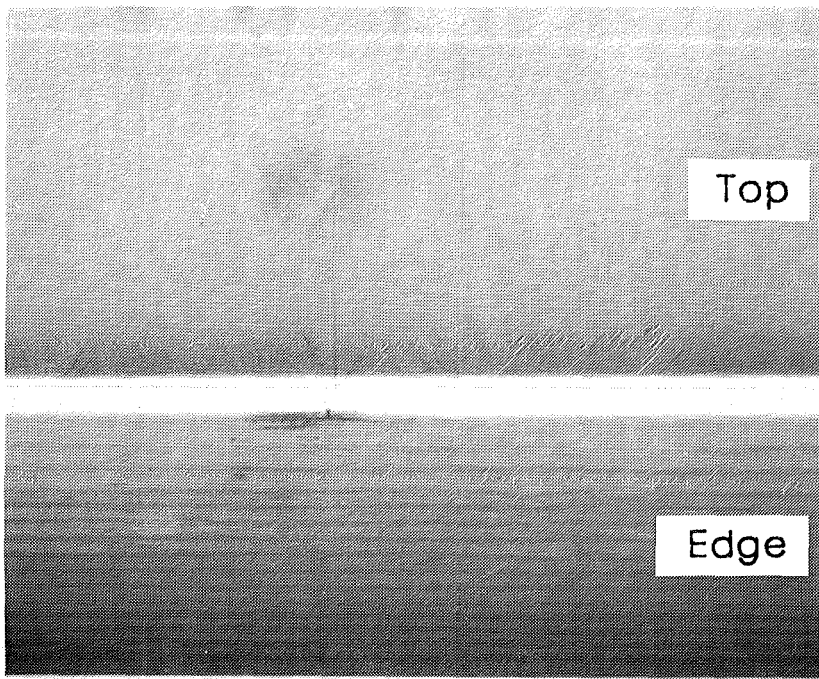
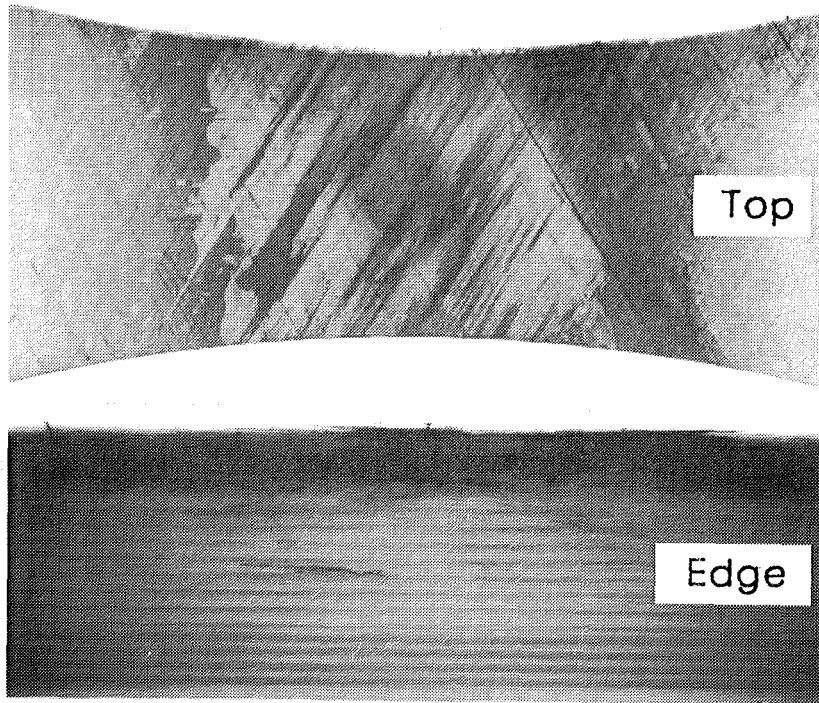
(i) Specimen 5-23 ($P = 11.6$ kips).

Figure 25.- Continued.

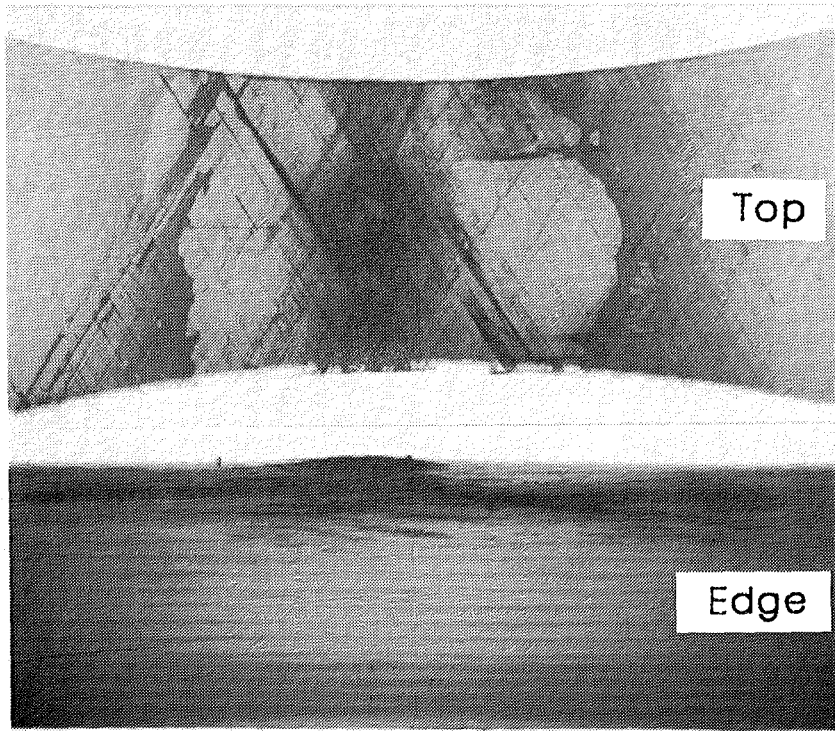


(j) Specimen 5-32 (P = 19.0 kips).

Figure 25.- Continued.



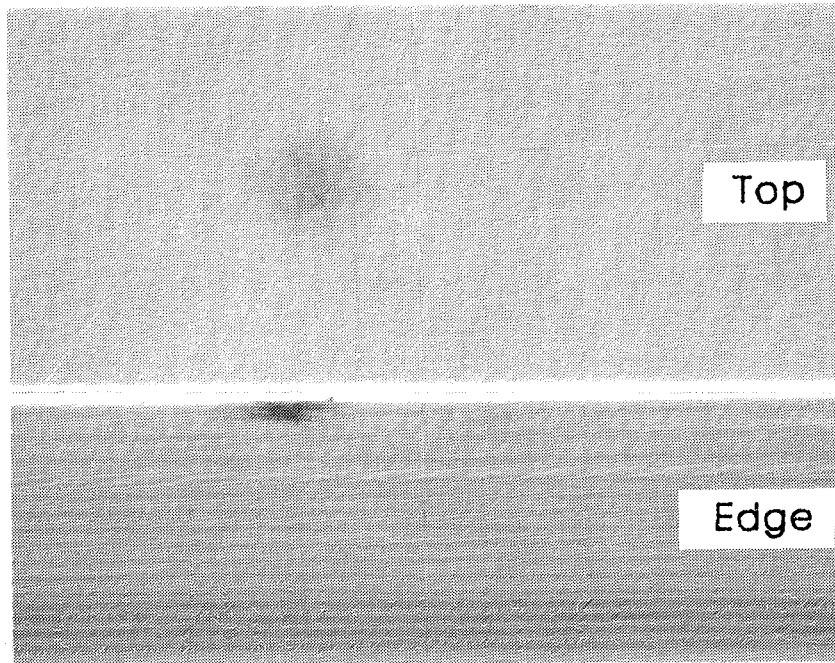
(k) Specimen 5-13.



Top

After
loading
to
1st-
ligament
failure

Edge

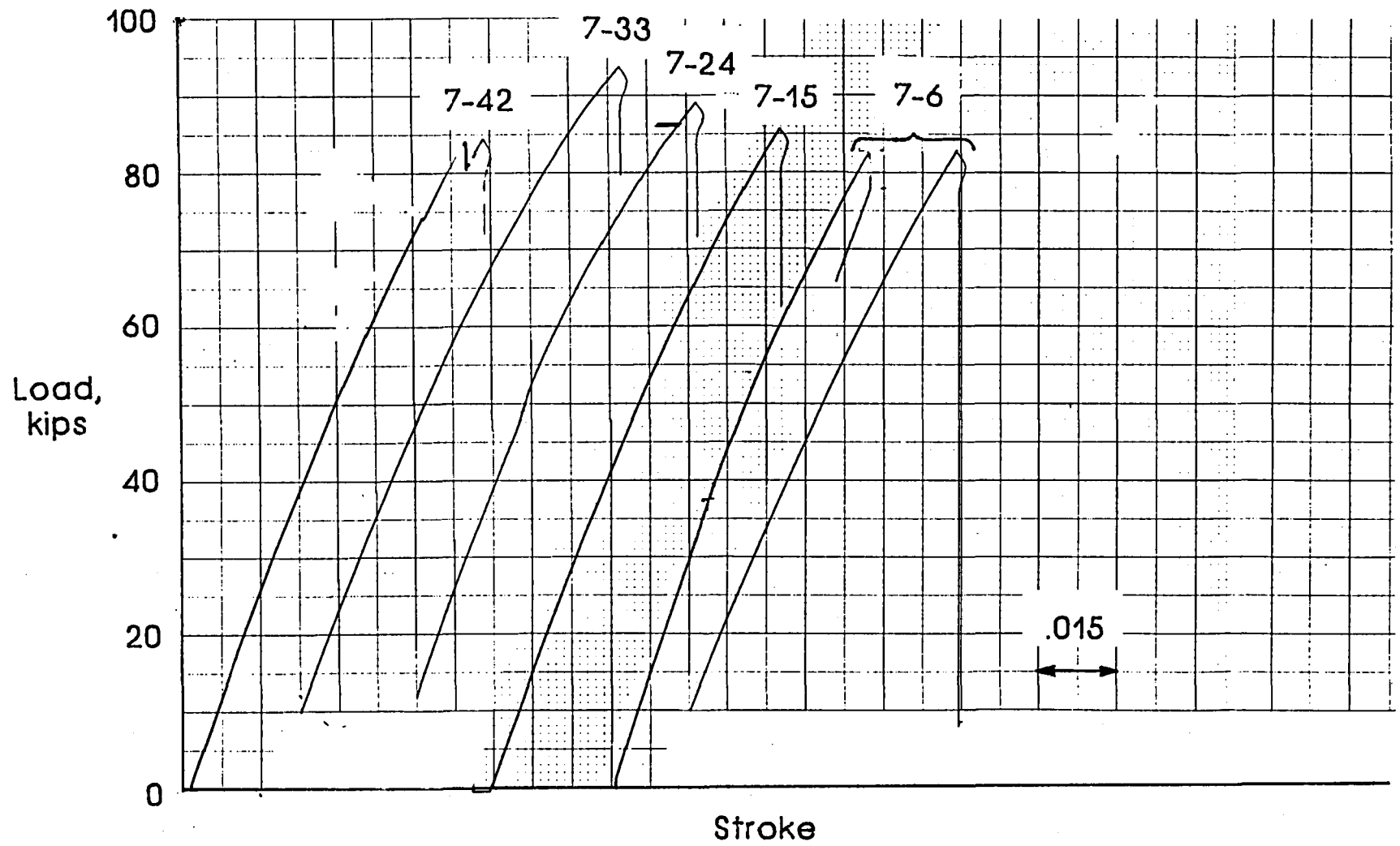


Top

Before
loading

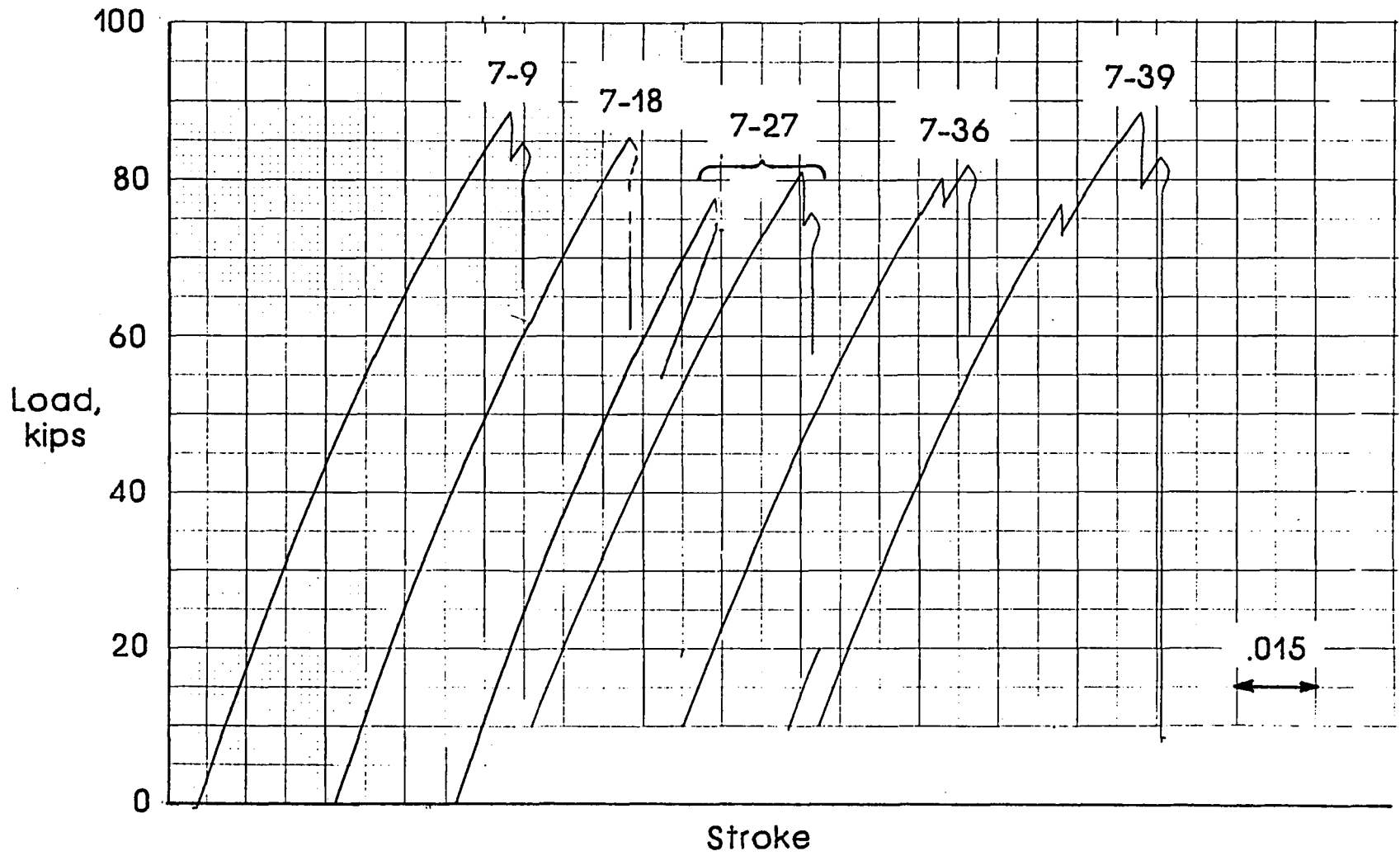
Edge

(I) Specimen 5-14 (P = 20.4 kips).



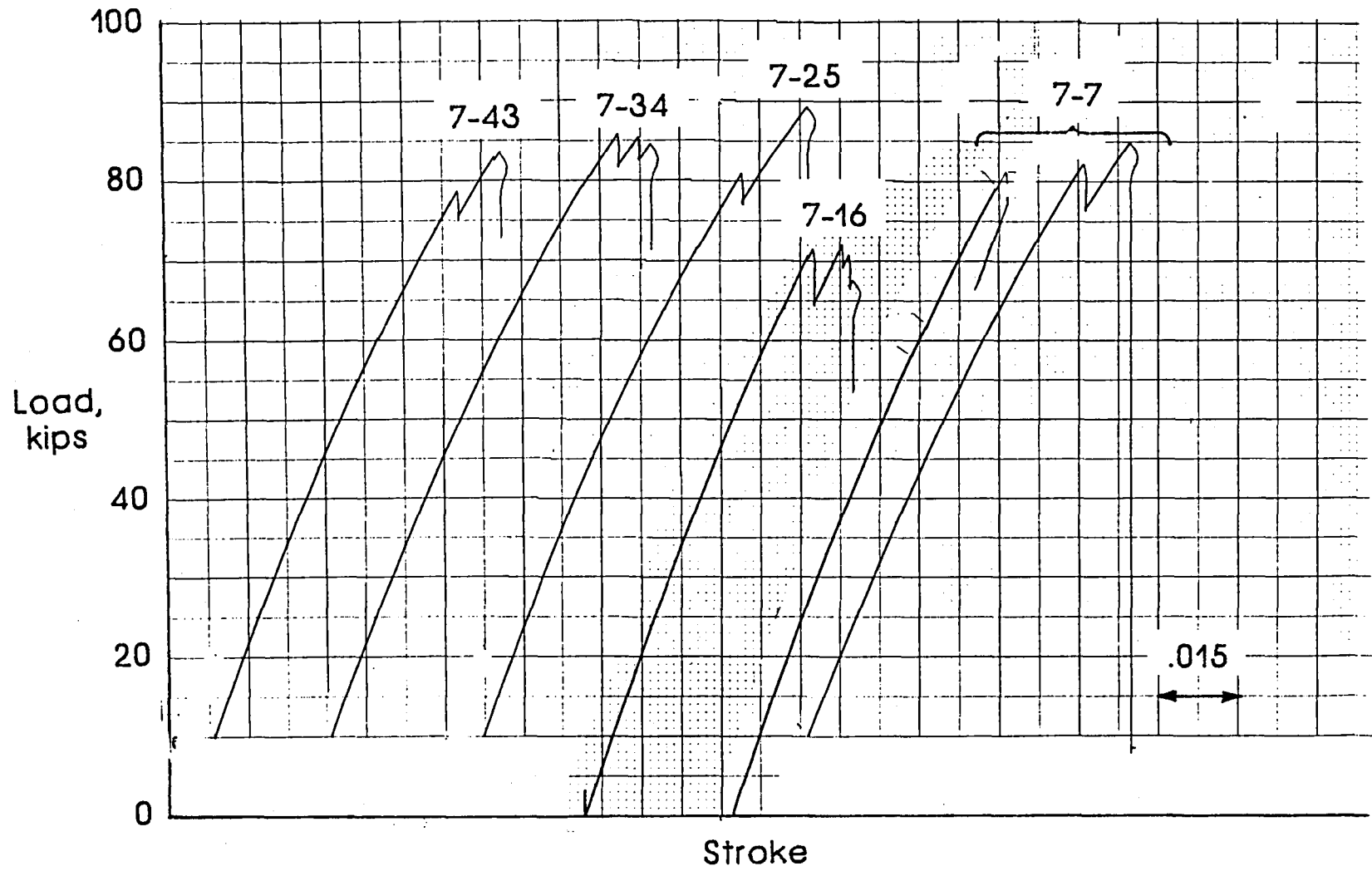
(a) $m_1 = 6.1 \text{ lbm}$ and $KE = 30.3 \text{ ft-lbf}$.

Figure 26.- Load-stroke records for impacted specimens from filled ring.



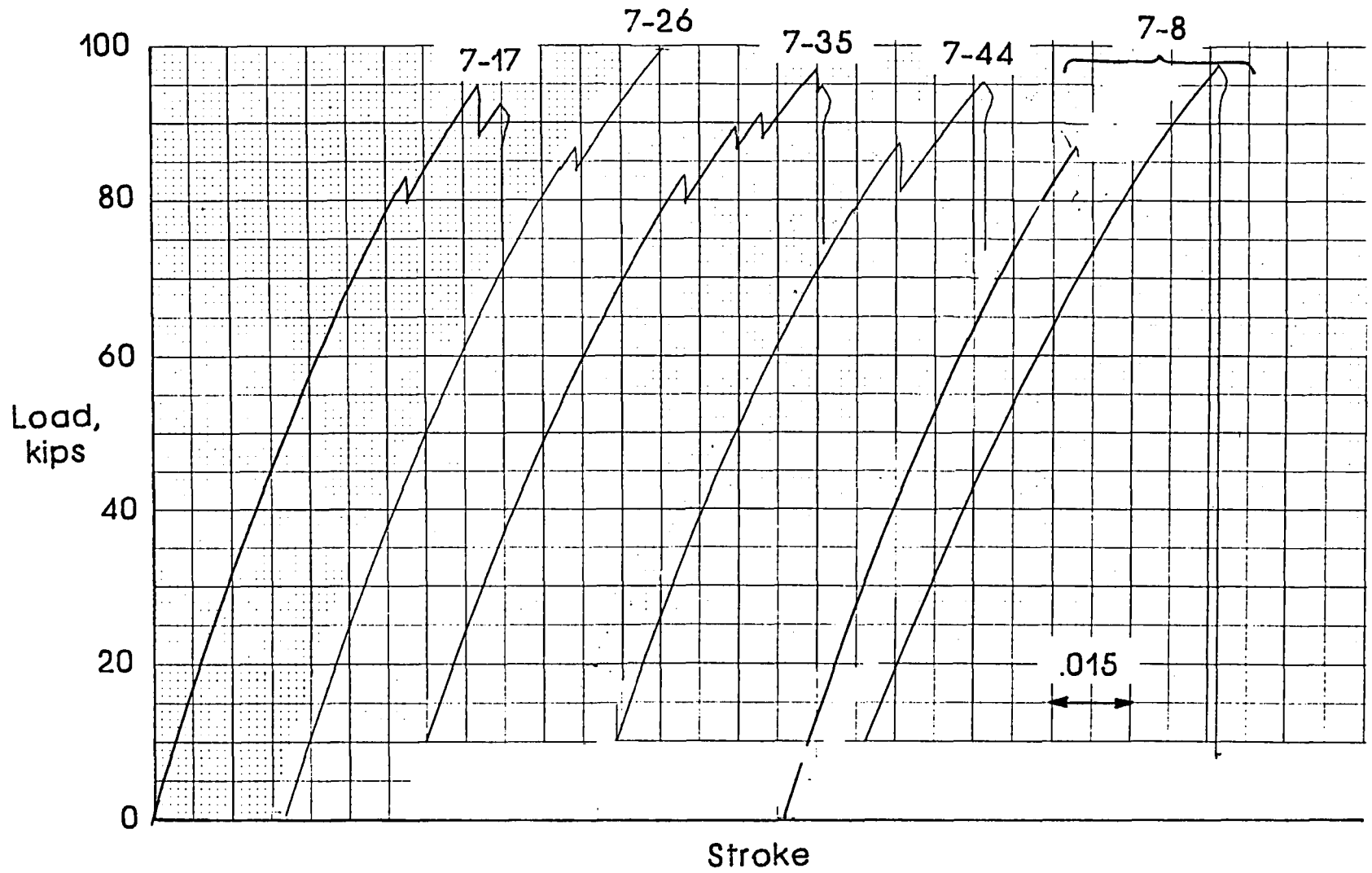
(b) $m_1 = 6.1 \text{ lbm}$ and $KE = 60.6 \text{ ft-lbf}$.

Figure 26.- Continued.



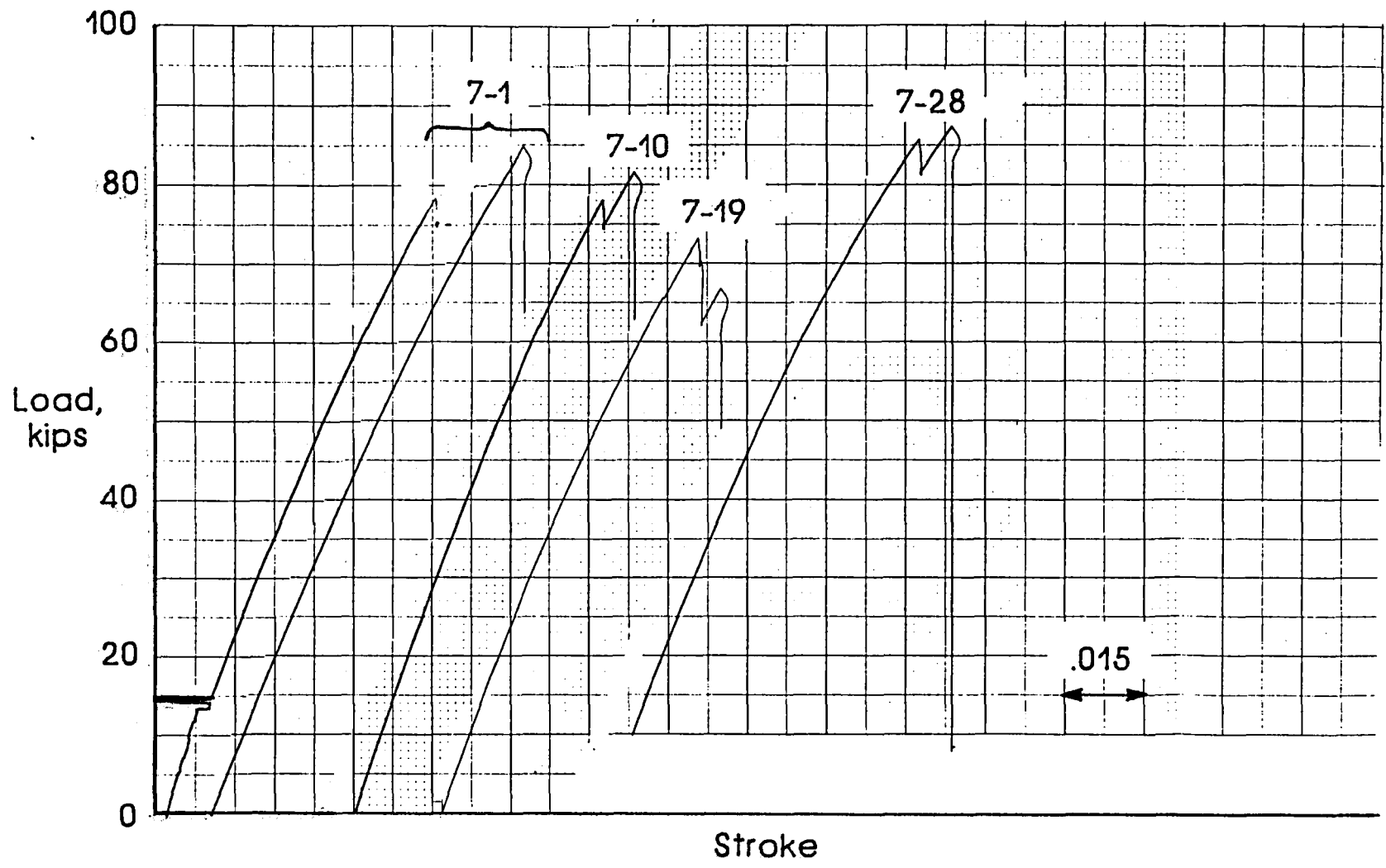
(c) $m_1 = 11.1 \text{ lbm}$ and $\text{KE} = 55.5 \text{ ft-lbf}$.

Figure 26.- Continued.



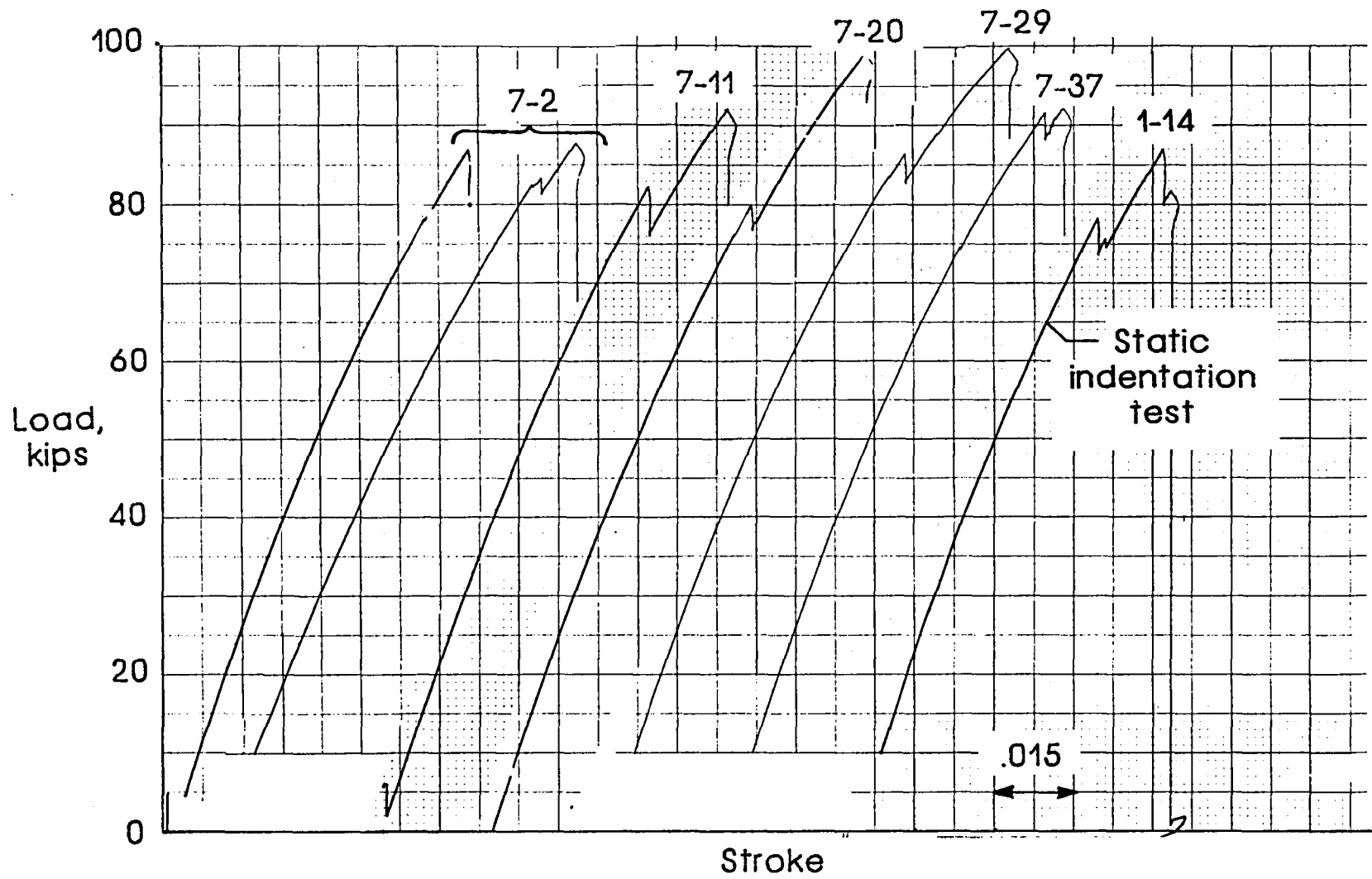
(d) $m_1 = 11.1 \text{ lbm}$ and $\text{KE} = 111. \text{ ft-lbf.}$

Figure 26.- Continued.



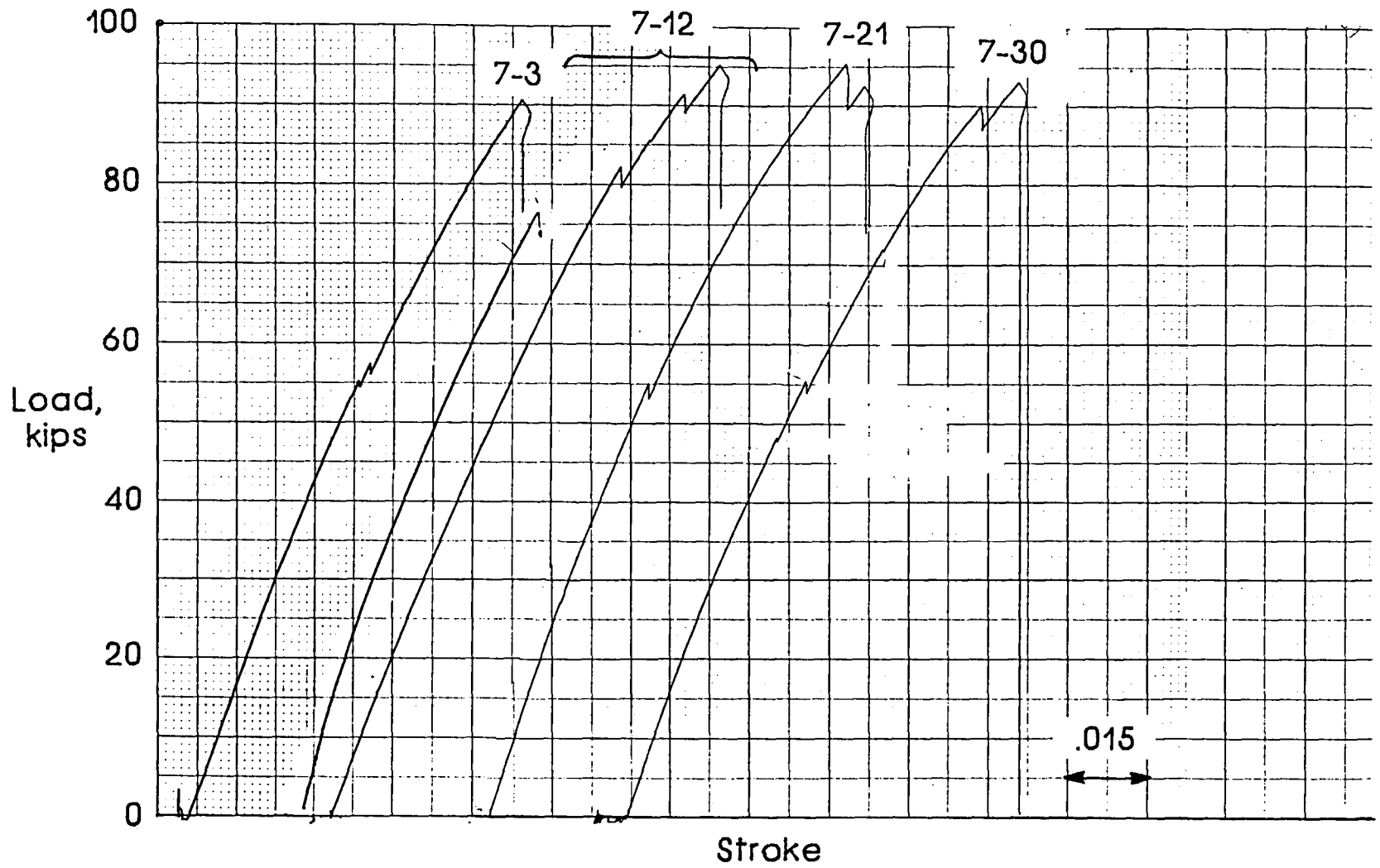
(e) $m_1 = 19.9$ lbm and $KE = 49.8$ ft-lbf.

Figure 26.- Continued.



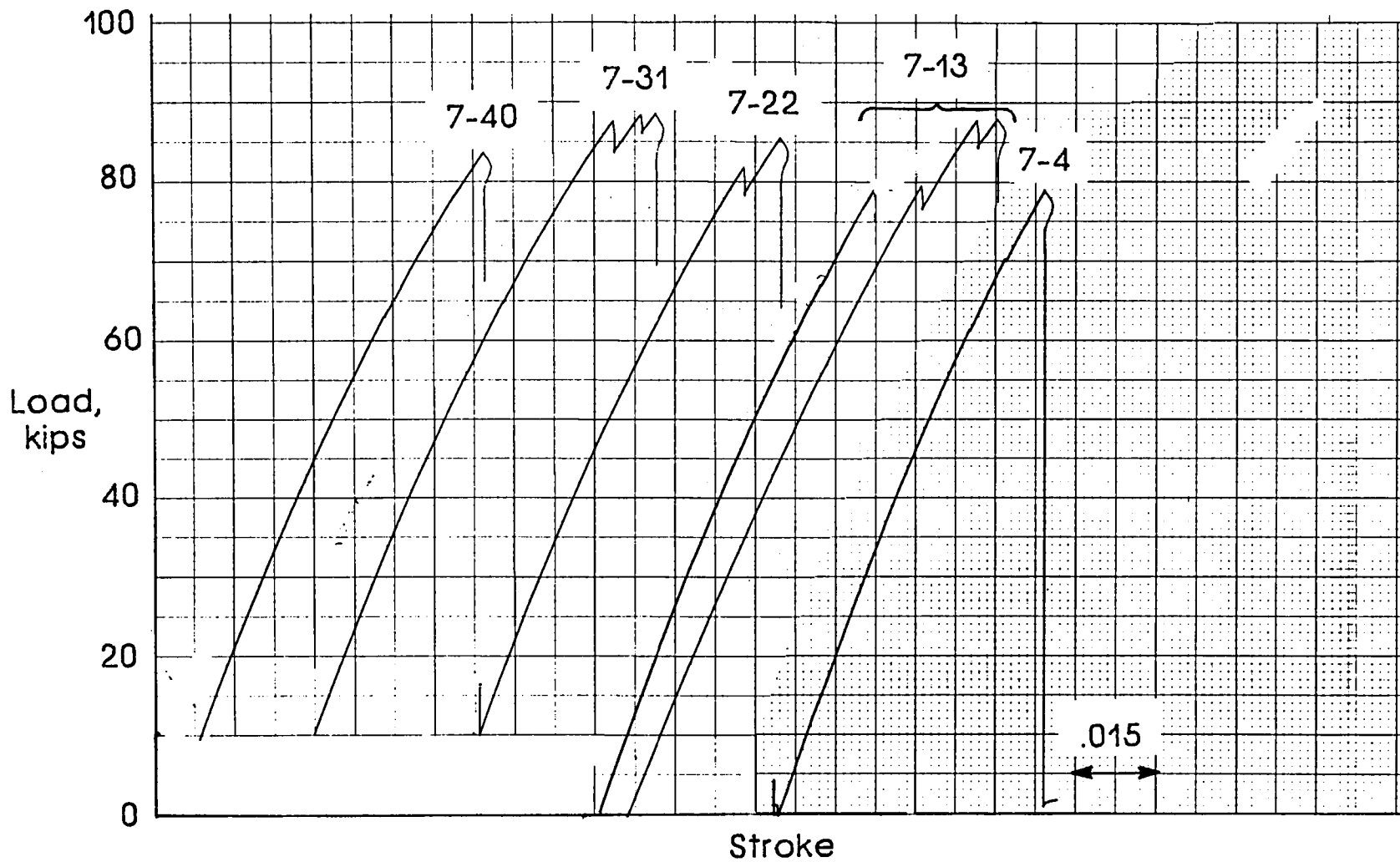
(f) $m_1 = 19.9 \text{ lbm}$ and $KE = 99.5 \text{ ft-lbf}$.

Figure 26.- Continued.



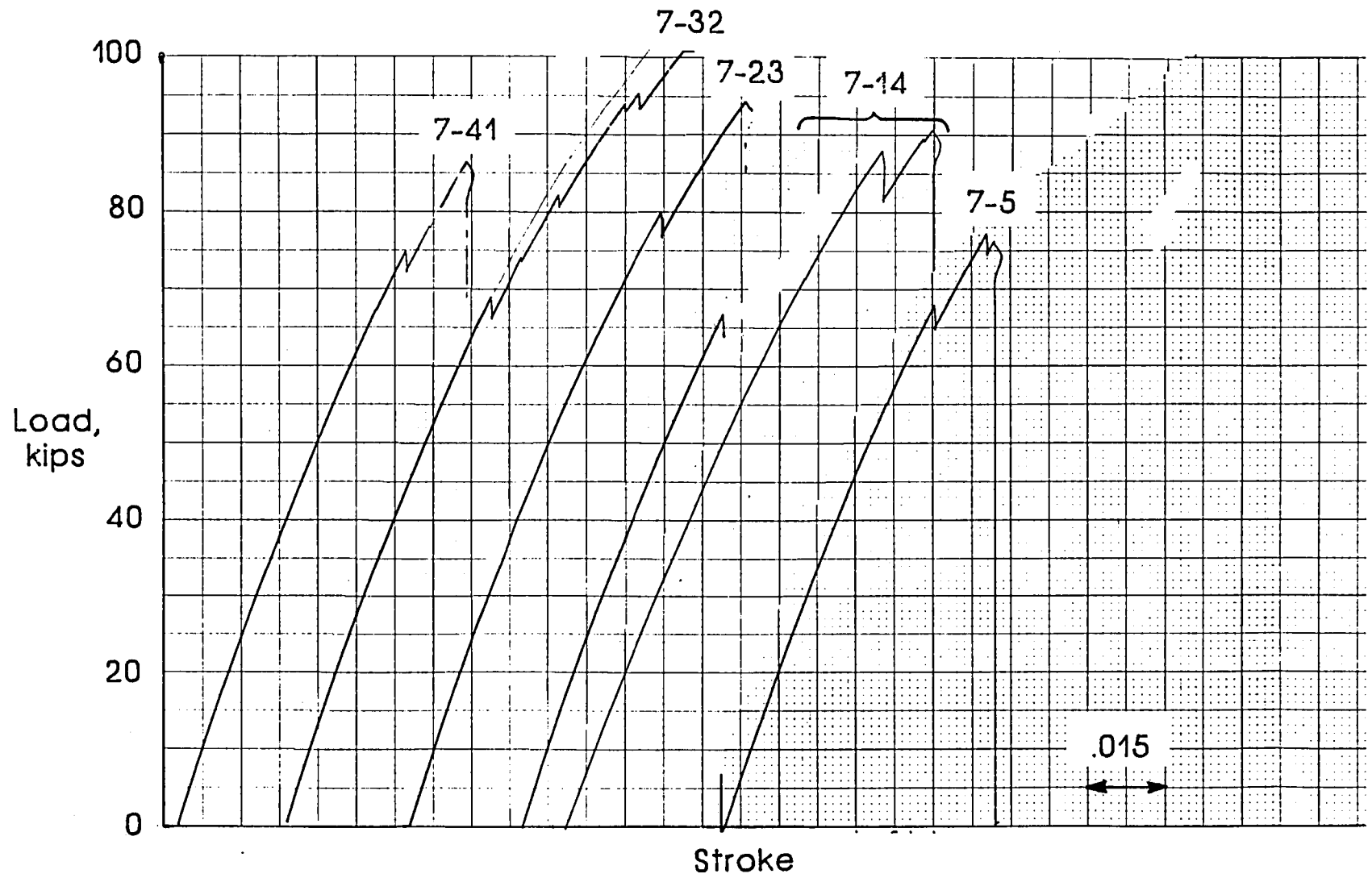
(g) $m_1 = 19.9$ lbm and $KE = 199$ ft-lbf.

Figure 26.- Continued.



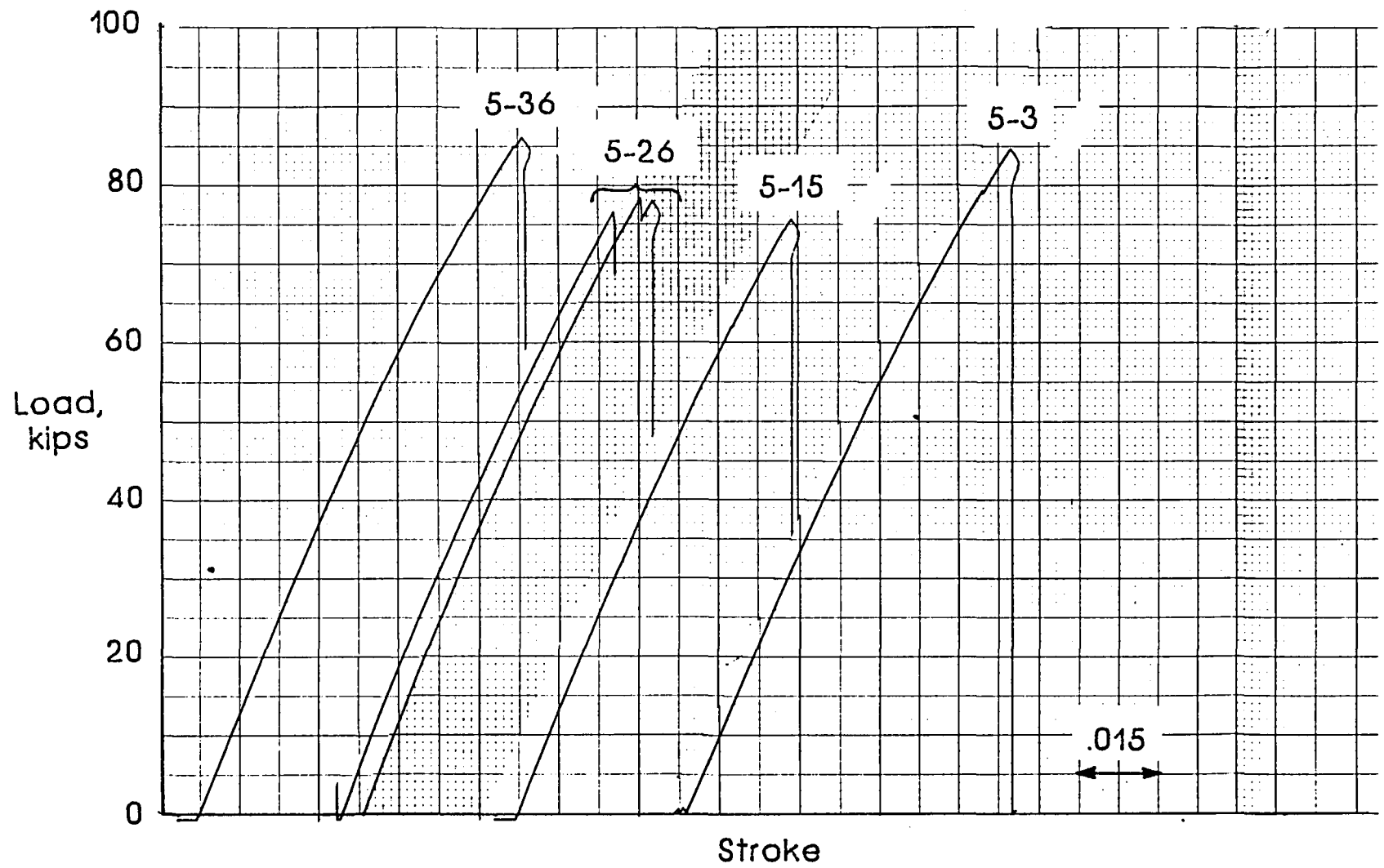
(h) $m_1 = 41.1 \text{ lbm}$ and $KE = 51.4 \text{ ft-lbf}$.

Figure 26.- Continued.



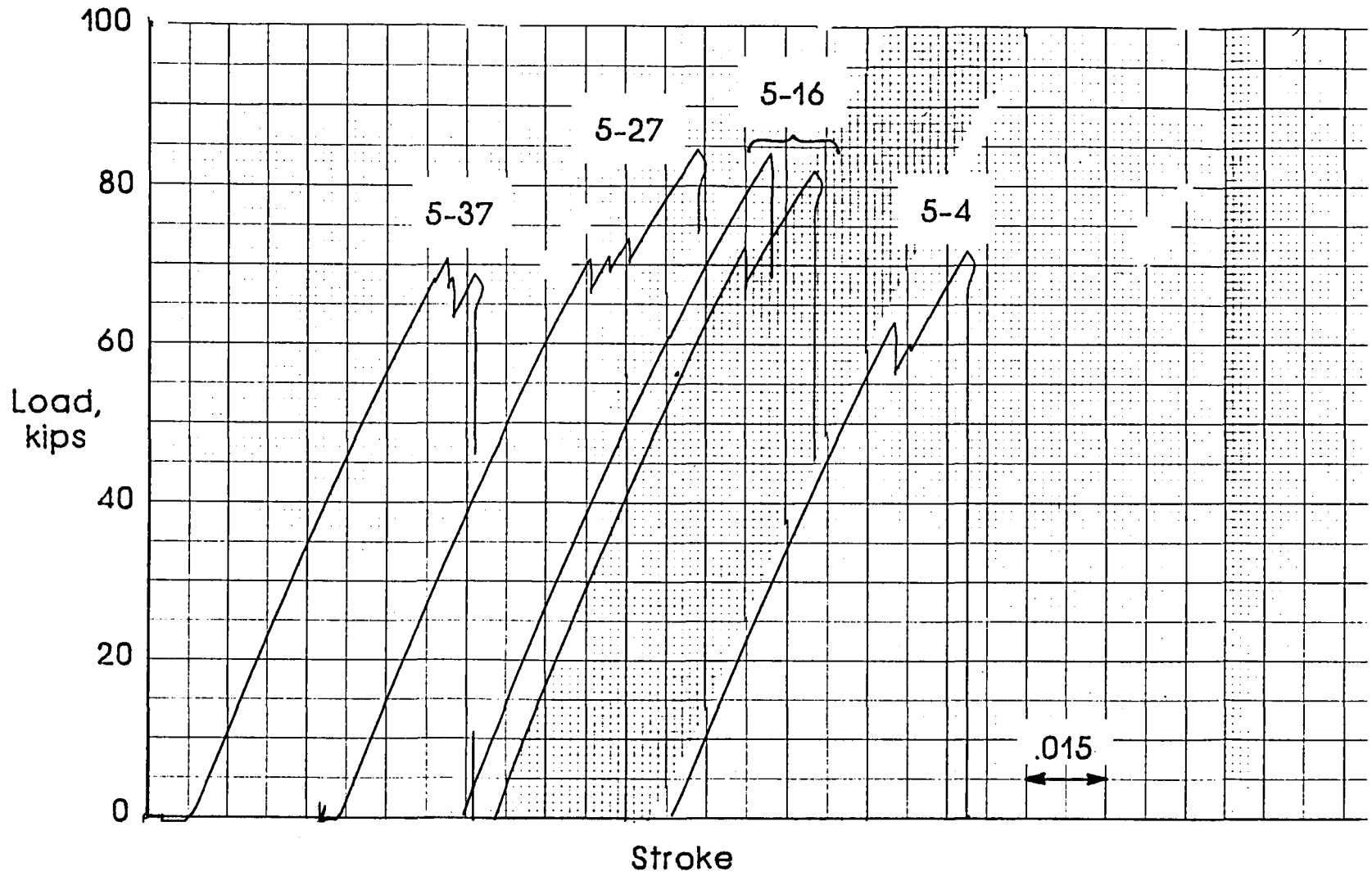
(i) $m_1 = 41.1 \text{ lbm}$ and $\text{KE} = 206. \text{ ft-lbf.}$

Figure 26.- Concluded.



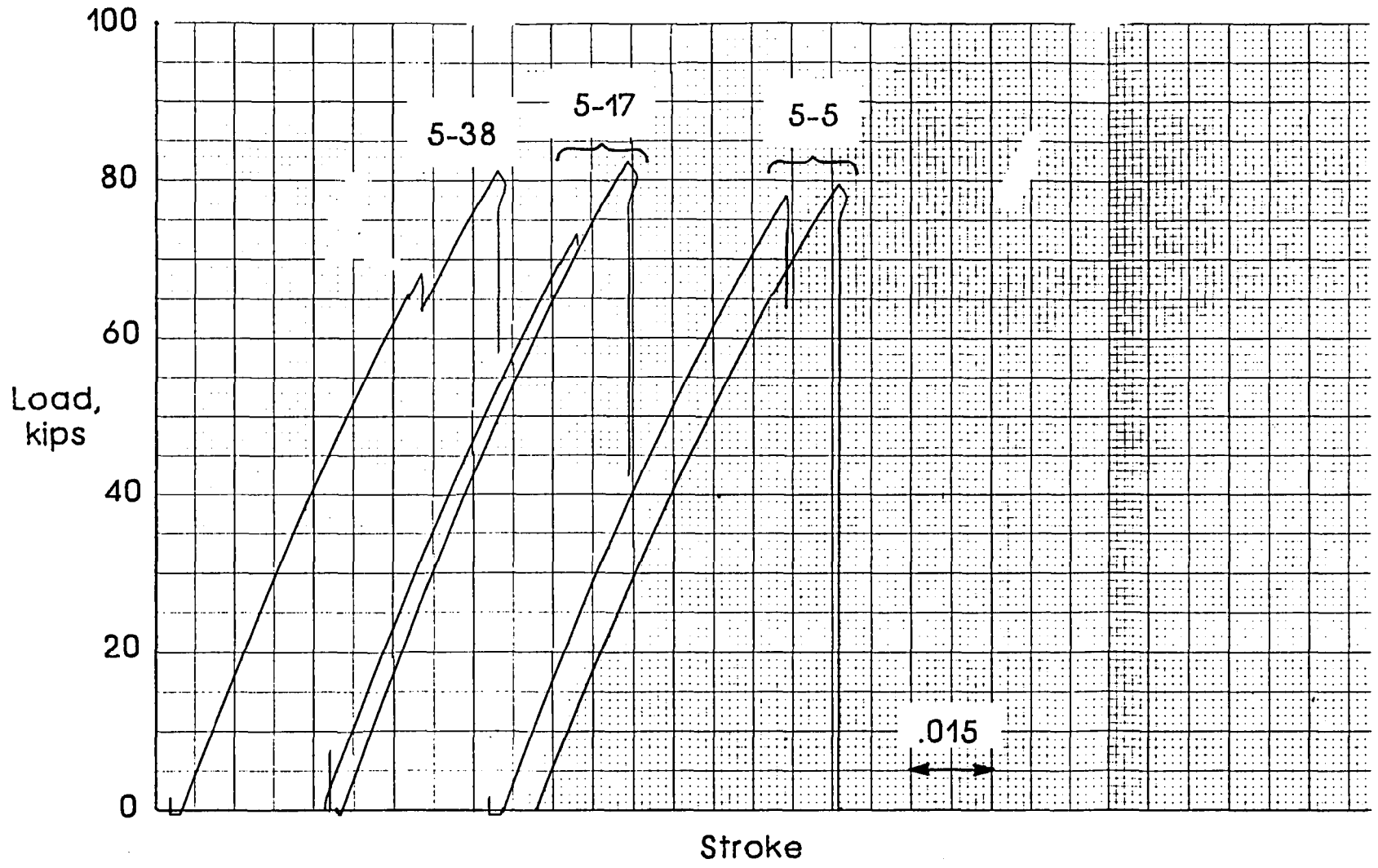
(a) $m_1 = 6.1 \text{ lbm}$ and $KE = 30.3 \text{ ft-lbf}$.

Figure 27.- Load-stroke records for impacted specimens from empty ring.



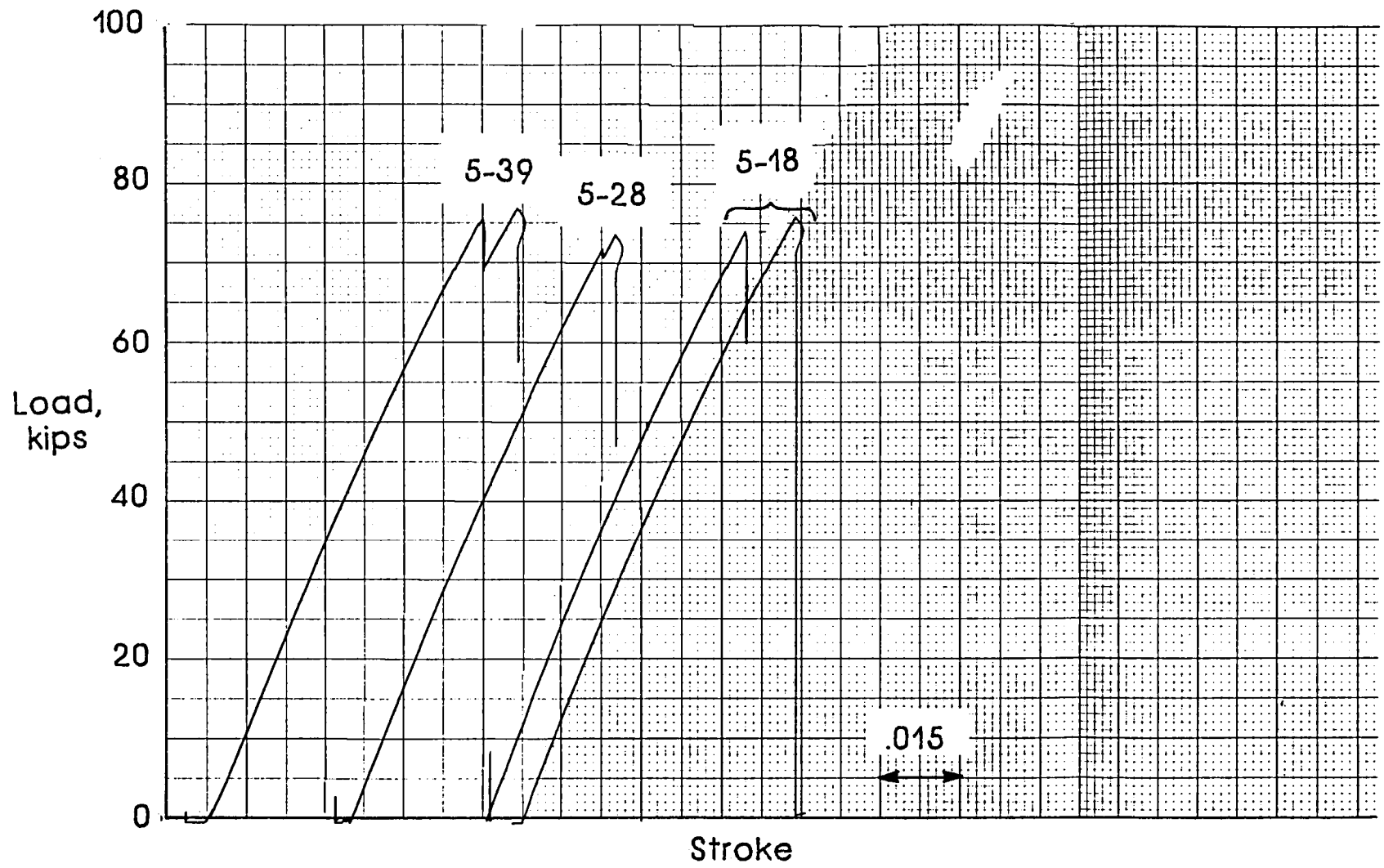
(b) $m_1 = 6.1 \text{ lbm}$ and $\text{KE} = 60.6 \text{ ft-lbf}$.

Figure 27.- Continued.



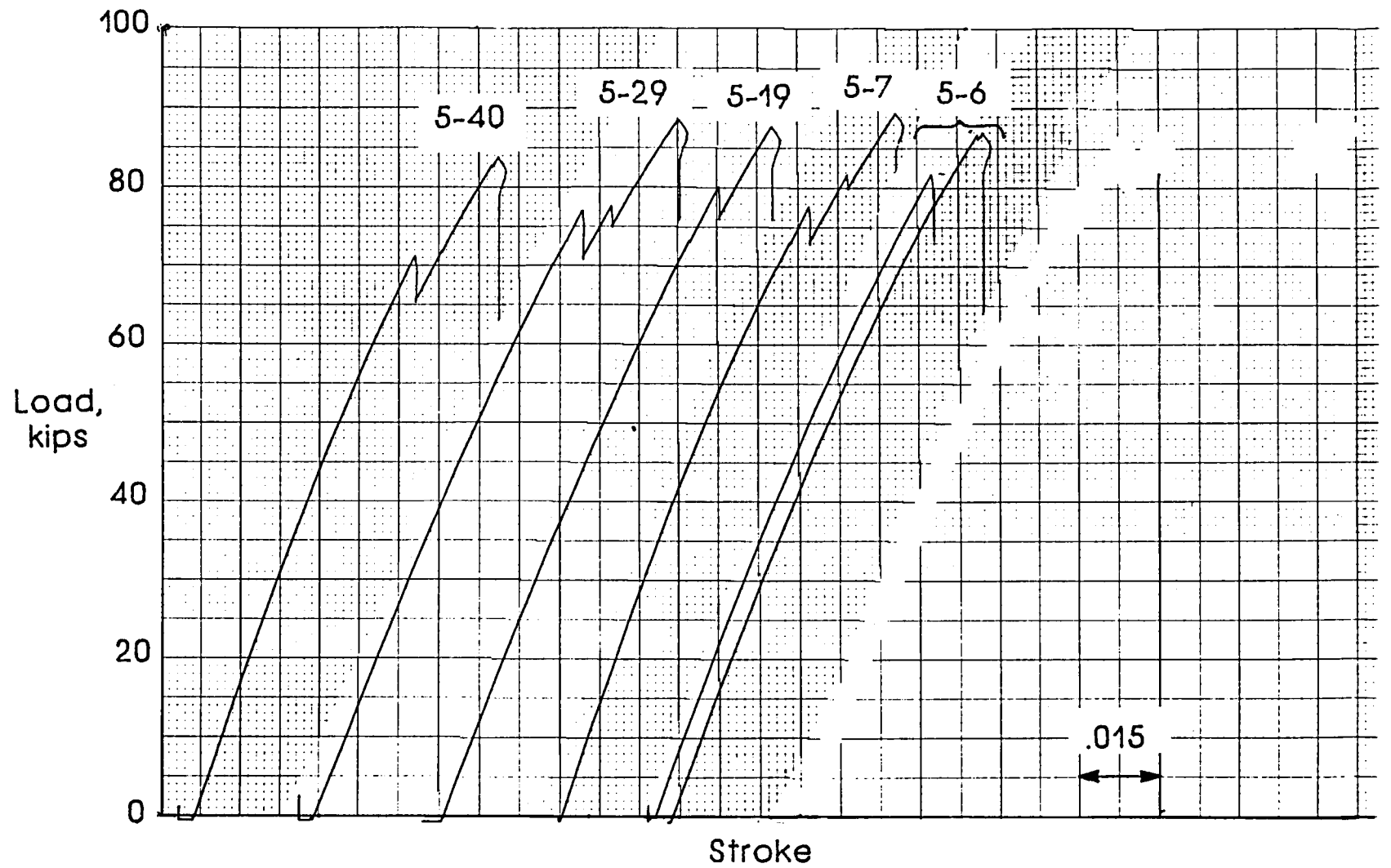
(c) $m_1 = 11.1 \text{ lbm}$ and $\text{KE} = 27.8 \text{ ft-lbf}$.

Figure 27.- Continued.



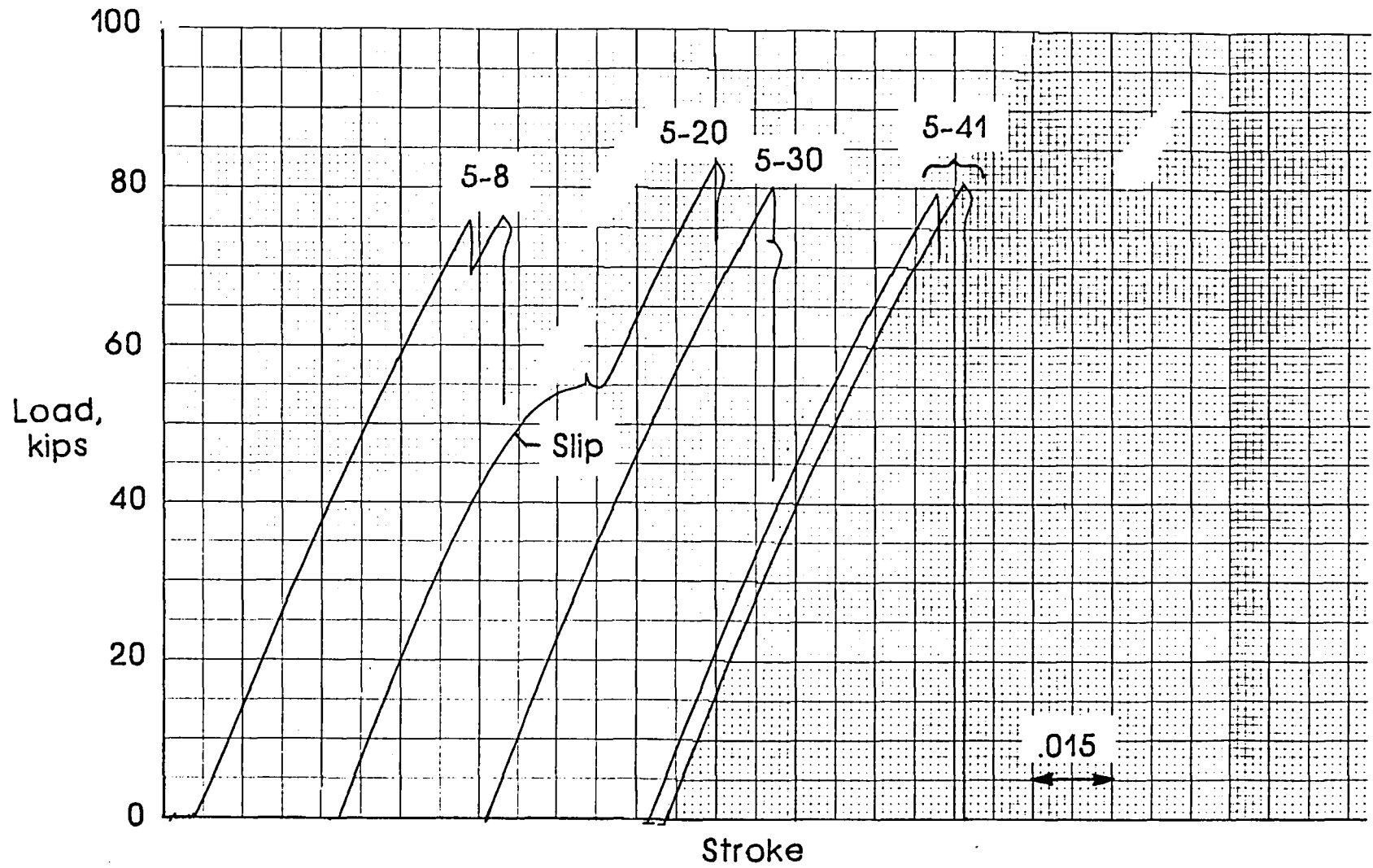
(d) $m_1 = 11.1 \text{ lbm}$ and $\text{KE} = 55.5 \text{ ft-lbf}$.

Figure 27.- Continued.



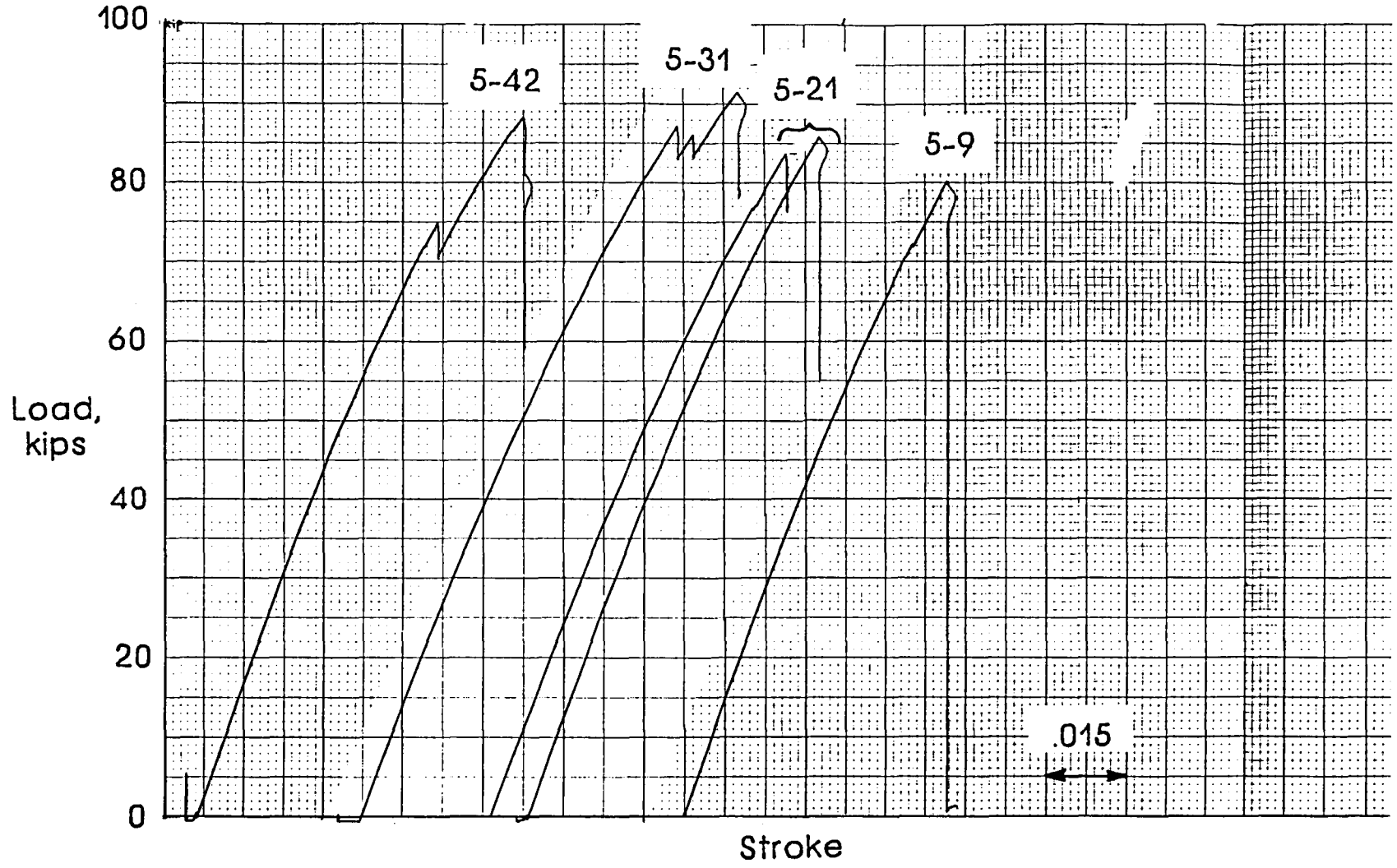
(e) $m_1 = 11.1 \text{ lbm}$ and $KE = 111. \text{ ft-lbf}$.

Figure 27.- Continued.



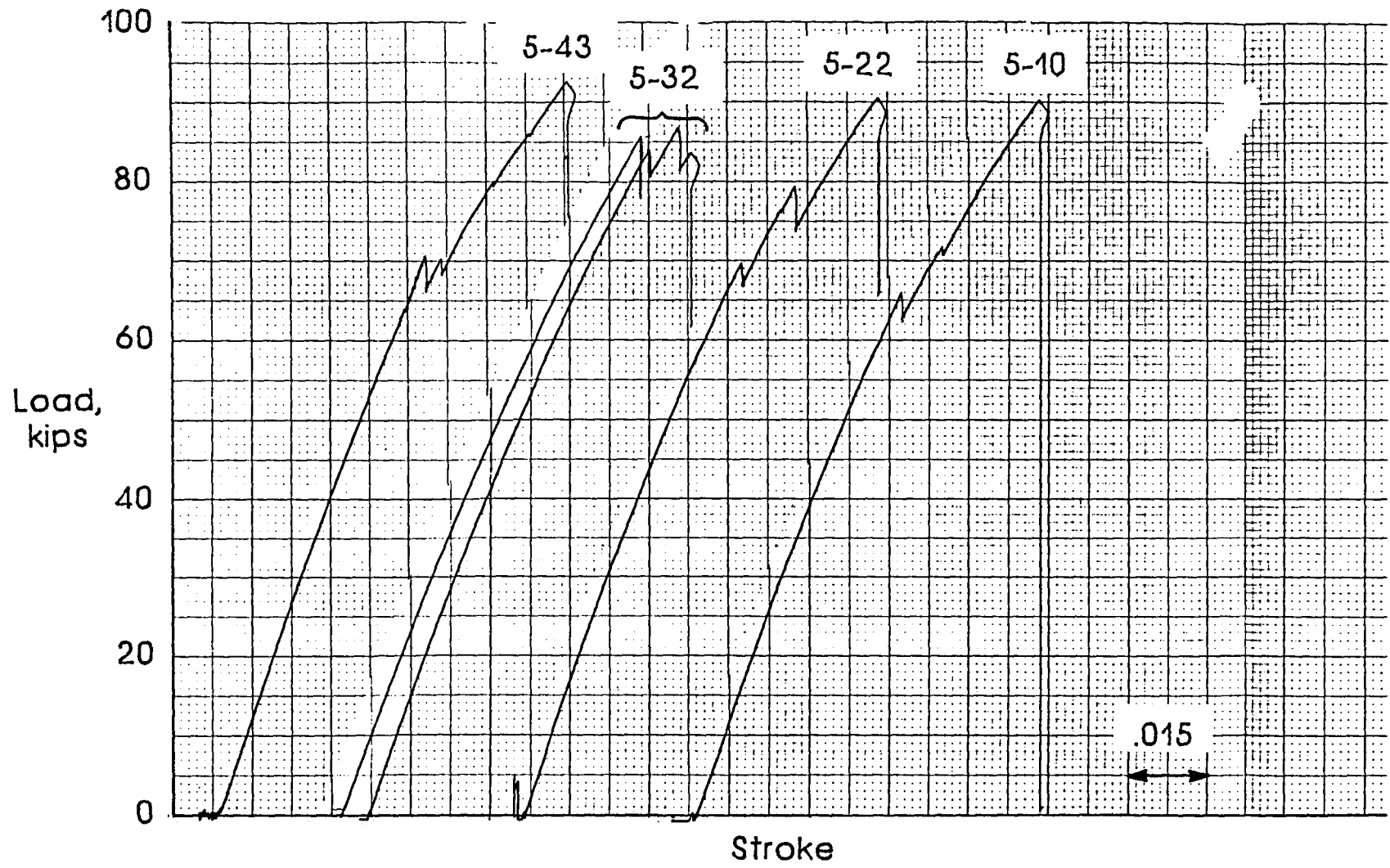
(f) $m_1 = 19.9 \text{ lbm}$ and $\text{KE} = 49.8 \text{ ft-lbf}$.

Figure 27.- Continued.



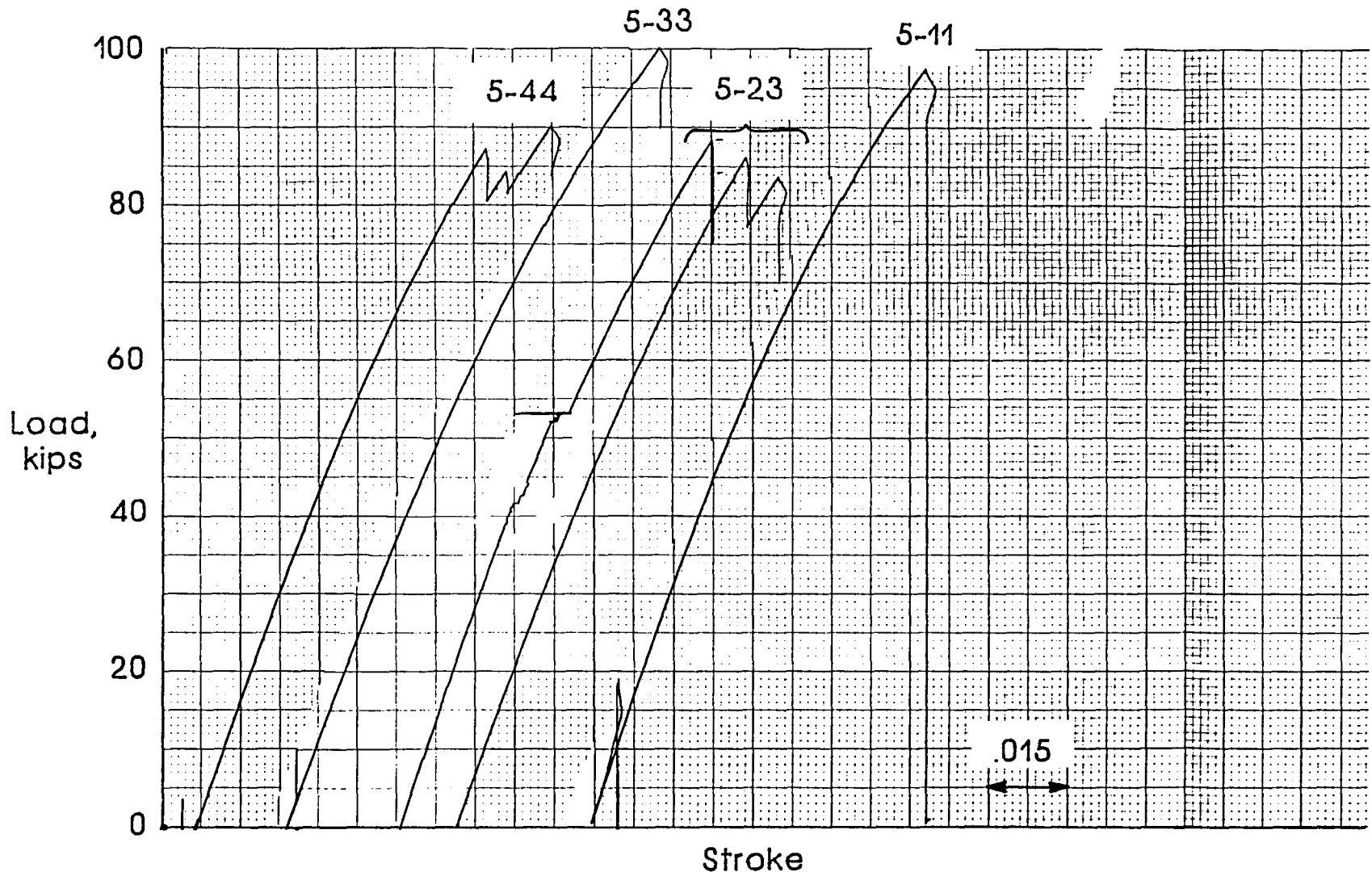
(g) $m_1 = 19.9 \text{ lbm}$ and $\text{KE} = 99.5 \text{ ft-lbf}$.

Figure 27.- Continued.



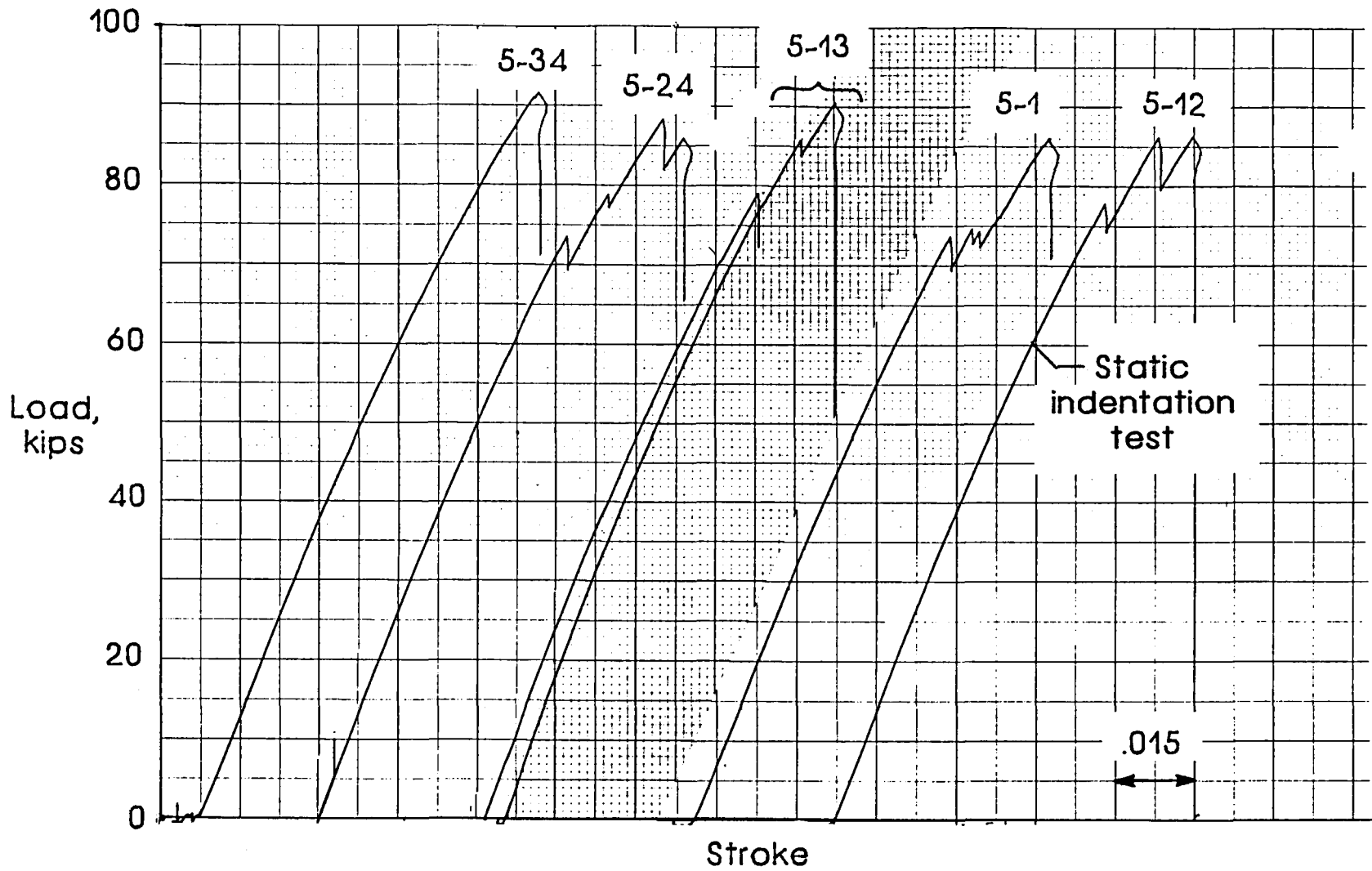
(h) $m_1 = 19.9 \text{ lbm}$ and $KE = 199. \text{ ft-lbf}$.

Figure 27.- Continued.



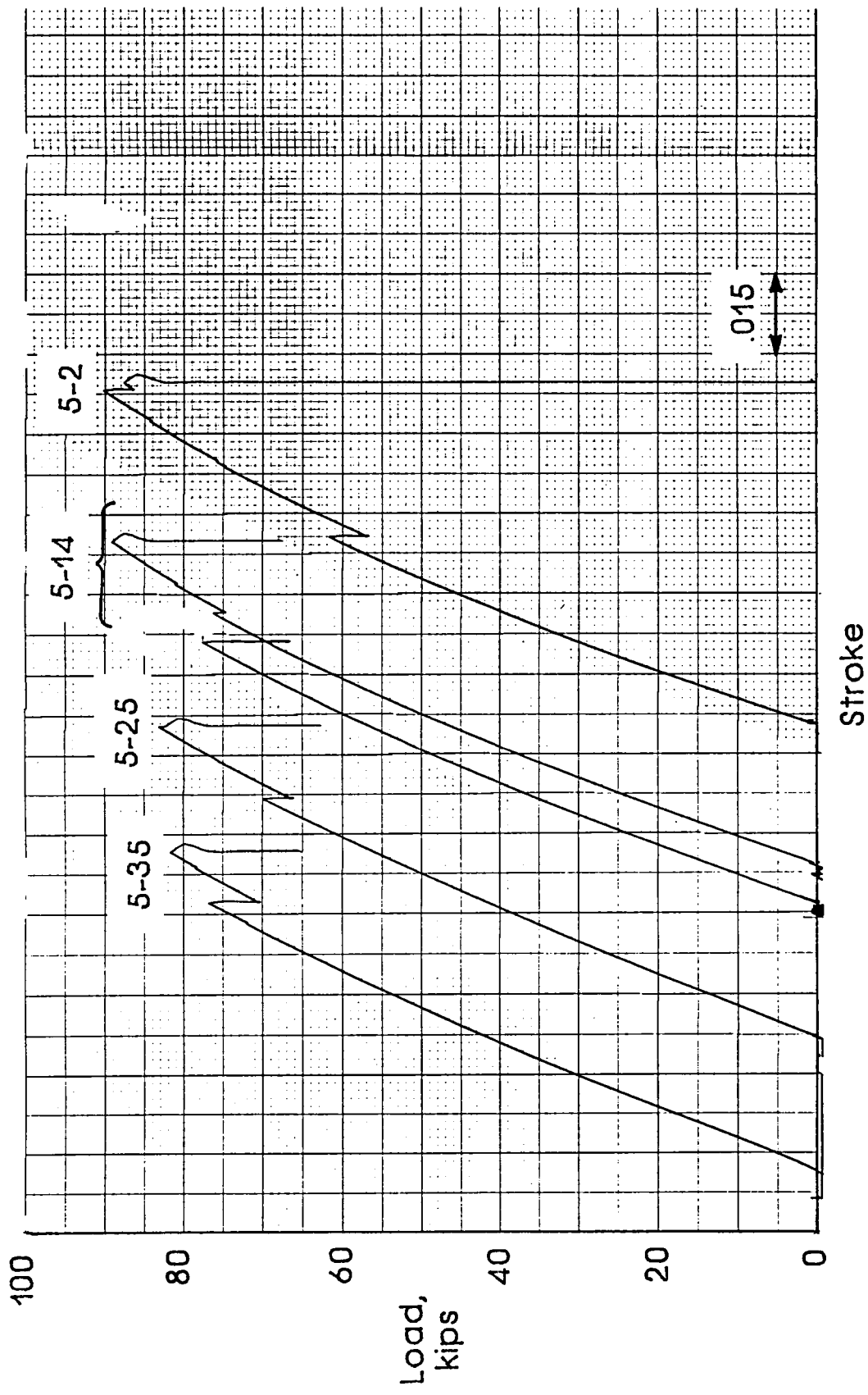
(i) $m_1 = 41.1 \text{ lbf}$ and $KE = 103. \text{ ft-lbf}$.

Figure 27.- Continued.



(j) $m_1 = 41.1 \text{ lbm}$ and $\text{KE} = 206. \text{ ft-lbf.}$

Figure 27.- Continued.



(k) $m_1 = 41.1$ lbm and $KE = 329$. ft-lbf.

Figure 27.- Concluded.

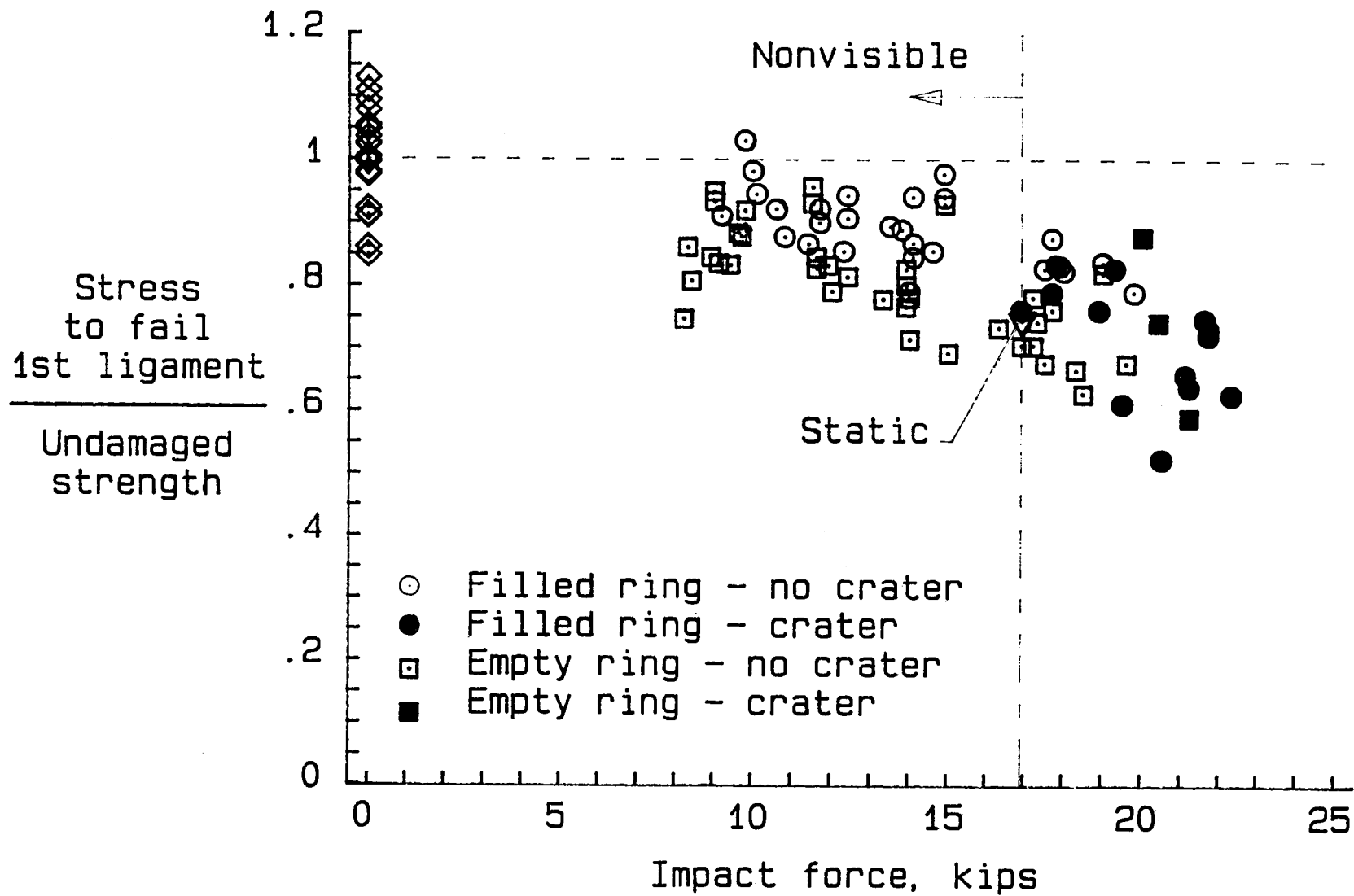


Figure 28.- Ratio of stress for first-ligament failure to undamaged strength versus impact force.

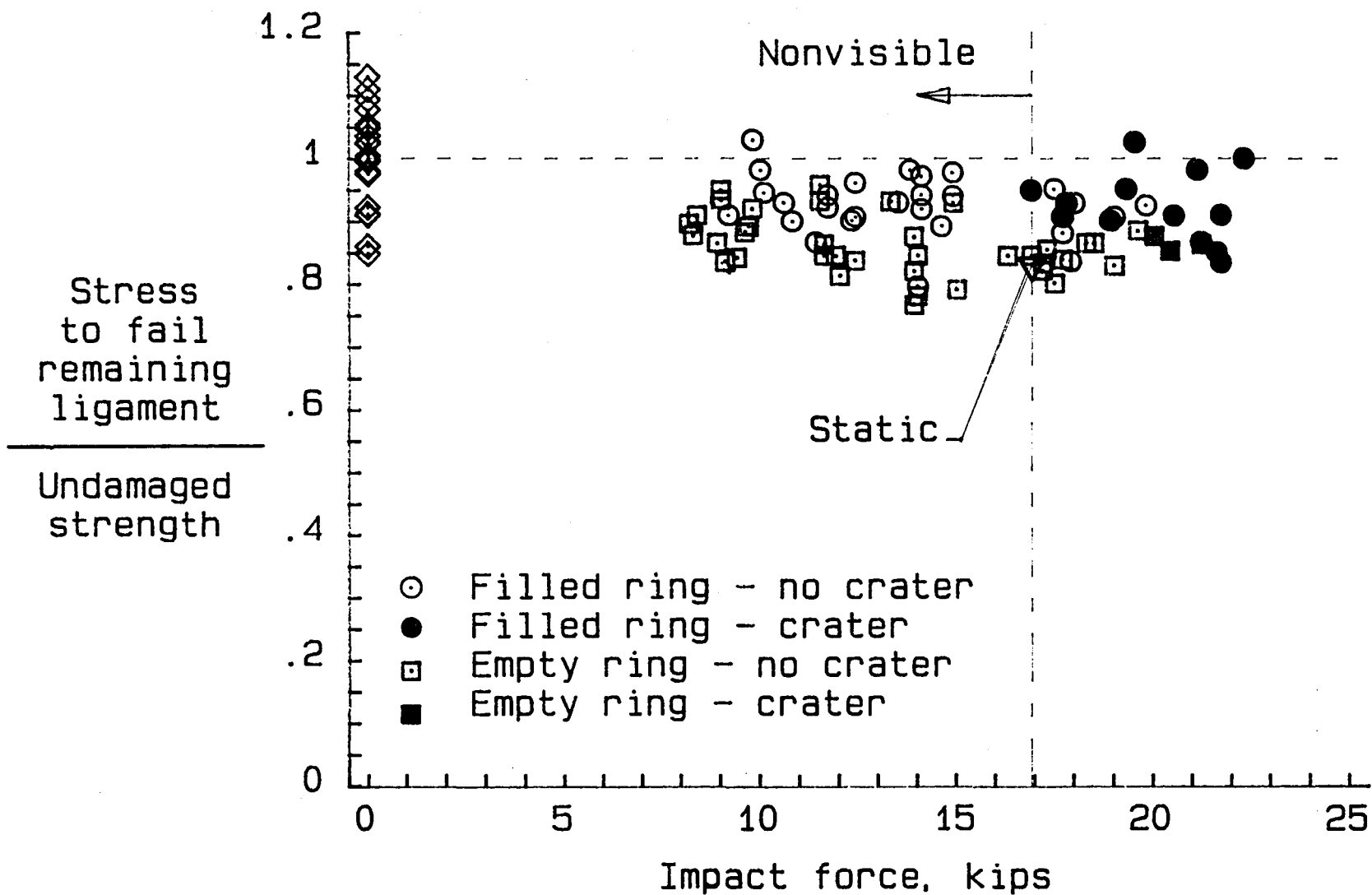


Figure 29.- Ratio of stress for remaining-ligament failure to undamaged strength versus impact force.

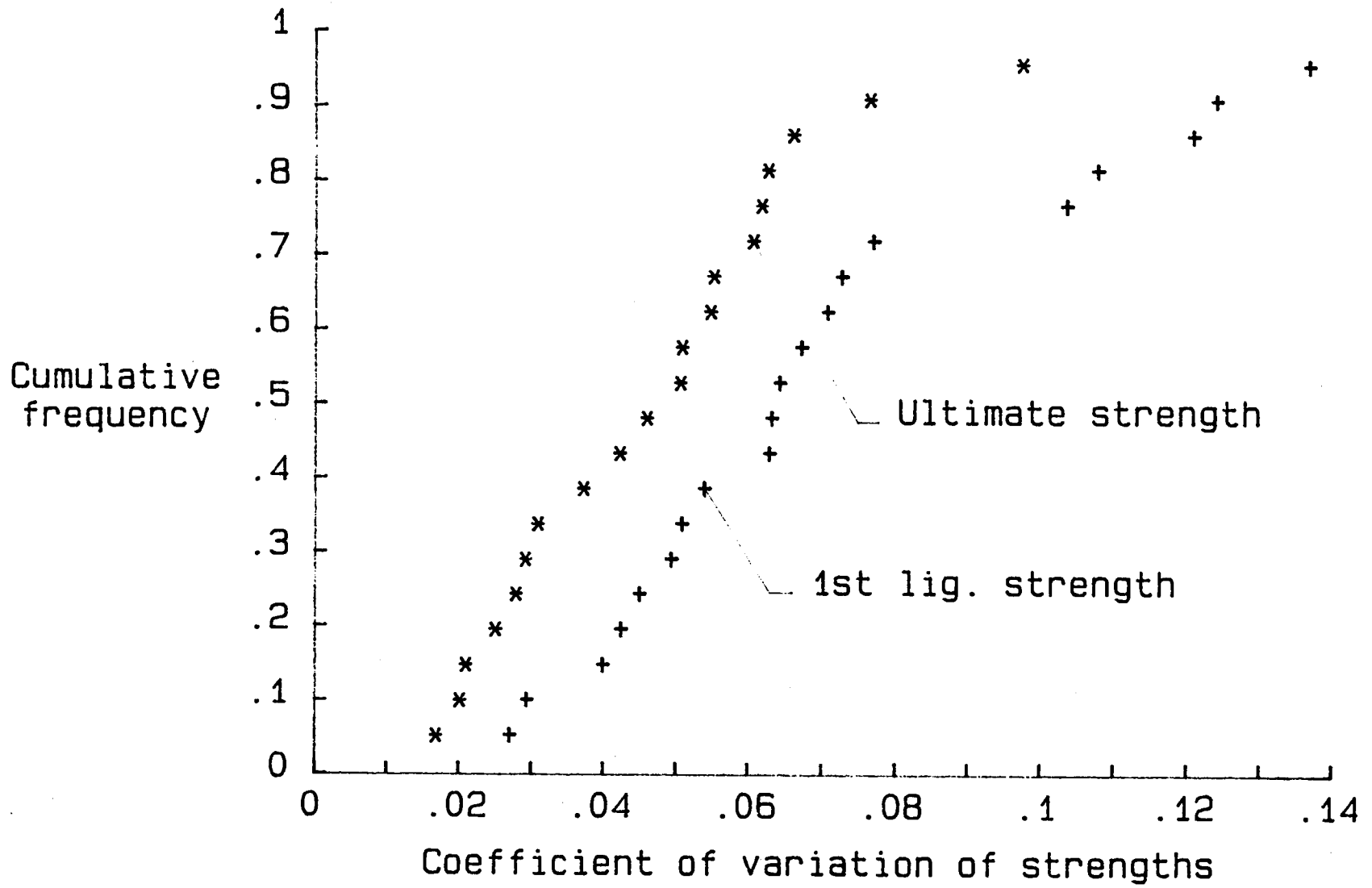


Figure 30.- Cumulative frequency versus coefficient of variation of strengths for groups of specimens with the same impactor mass and kinetic energy.

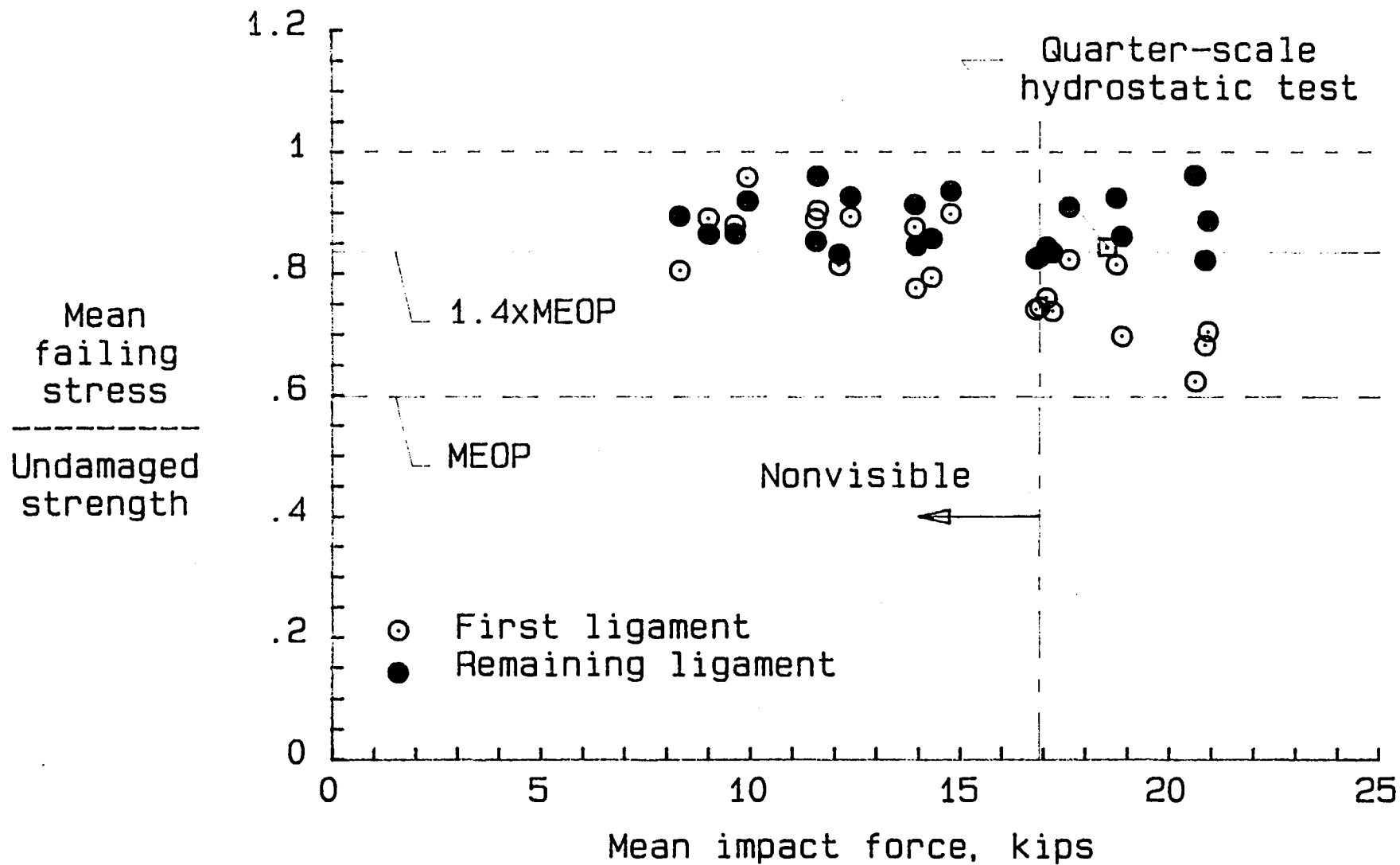


Figure 31.- Comparison of tensile tests and design conditions.

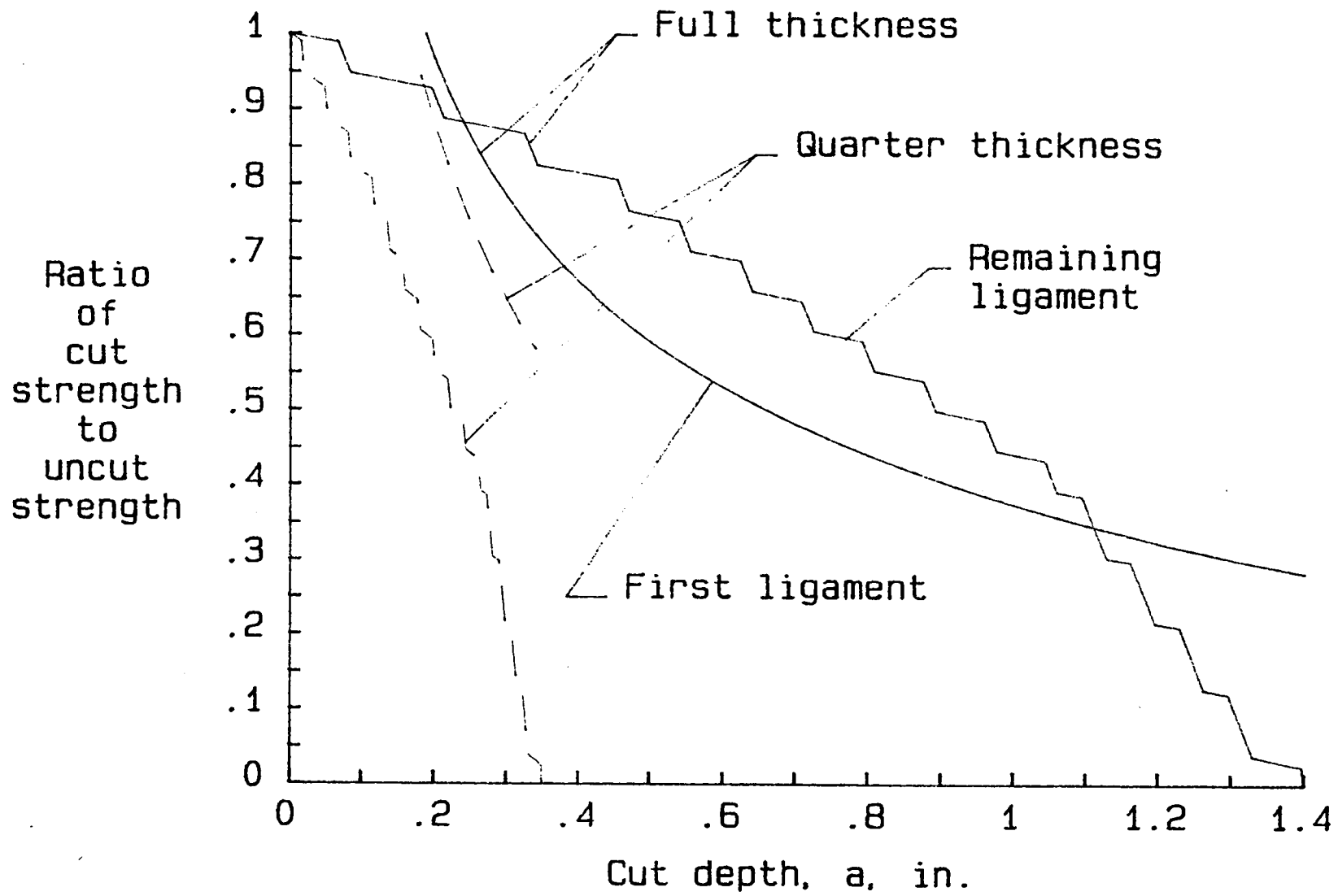


Figure 32.- Comparison of fracture behavior for full- and quarter-scale laminates. $c/a = 0.8$ and $K_Q = 27.3 \text{ ksi } \sqrt{\text{in.}}$

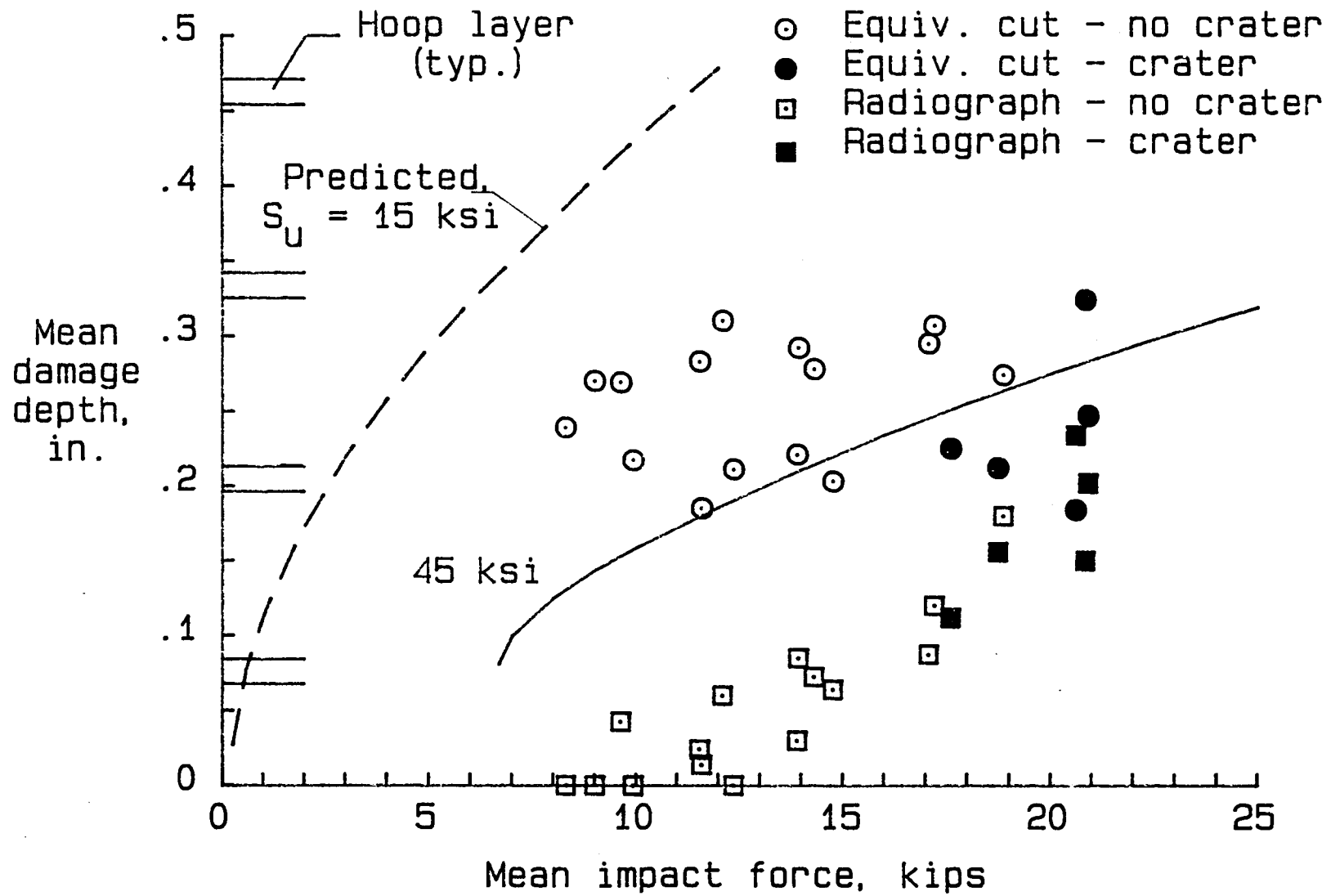


Figure 33.- Comparison of equivalent cut depth and measured and predicted damage depth.

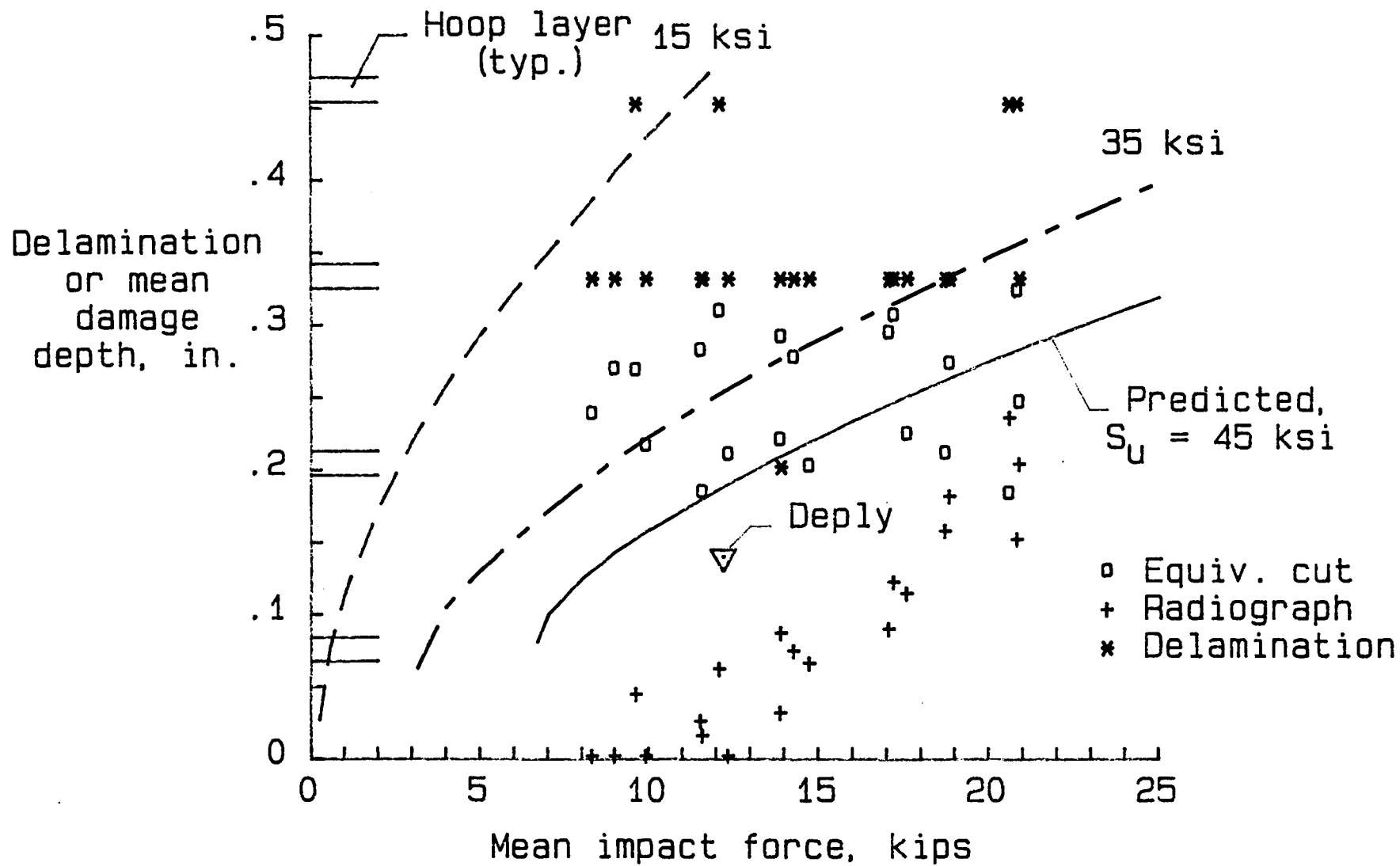
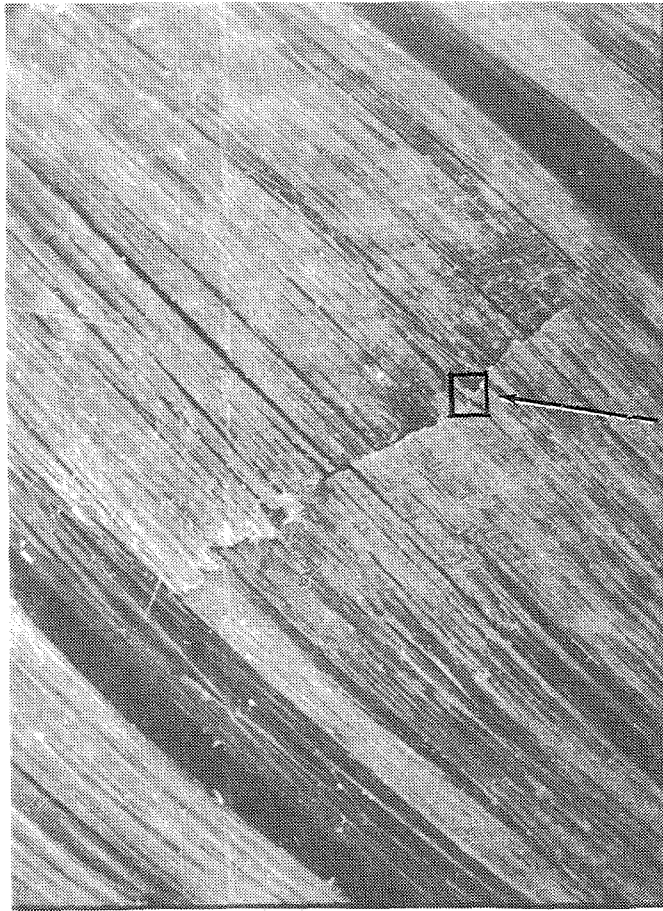
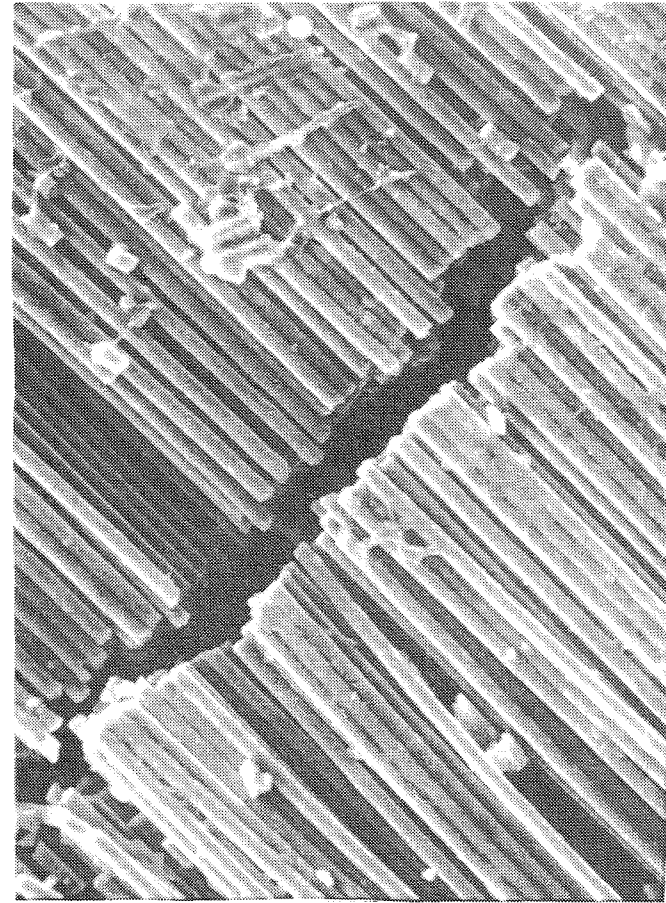


Figure 34.- Comparison of delamination and damage depth.



(a) 13X magnification.



(b) 280X magnification.

Figure 35.- Photographs of deepest layer with fibers broken by impact (second helical layer below the outermost hoop layer).

1. Report No. NASA TM-87771		2. Government Accession No.		3. Recipient's Catalog No.	
4. Title and Subtitle Tension Strength of a Thick Graphite/Epoxy Laminate After Impact by a 1/2-in.-Radius Impactor				5. Report Date July 1986	
				6. Performing Organization Code 534-06-23	
7. Author(s) C. C. Poe, Jr., W. Illg and D. P. Garber*				8. Performing Organization Report No.	
9. Performing Organization Name and Address NASA Langley Research Center Hampton, VA 23665				10. Work Unit No.	
				11. Contract or Grant No.	
12. Sponsoring Agency Name and Address National Aeronautics and Space Administration Washington, DC 20546				13. Type of Report and Period Covered Technical Memorandum	
				14. Army Project No.	
15. Supplementary Notes *D. P. Garber, PRC Kentron, Inc., Hampton, VA 23666					
16. Abstract NASA is developing graphite/epoxy filament-wound cases for the solid rocket motors of the space shuttle. They are wet-wound with AS4W graphite fiber and HBRF-55A epoxy. The membrane region is about 1.4 inches thick. Two 30-inch-diameter by 12-inch-long cylinders were impacted every two inches of circumference with 1/2-inch-radius impactors that were dropped from various heights. One cylinder was empty and the other was filled with inert propellant. Two-inch-wide test specimens were cut from the cylinders. Each was centered on an impact site. The specimens were x-rayed and loaded to failure in uniaxial tension. Rigid body mechanics and the Hertz law were used to predict impact force, local deformations, contact diameters, and contact pressures. The depth of impact damage was predicted using Love's solution for pressure applied on part of the boundary of a semi-infinite body. The predictions were reasonably good. The strengths of the impacted specimens were reduced by as much as 37 percent without visible surface damage. Even the radiographs did not reveal the nonvisible damage.					
17. Key Words (Suggested by Author(s)) Composite materials Radiography Fracture mechanics Space Shuttle Filament winding Solid rocket motor Graphite/epoxy case Impact Pressure vessel				18. Distribution Statement Unclassified - Unlimited Subject Category 24	
19. Security Classif. (of this report) Unclassified		20. Security Classif. (of this page) Unclassified		21. No. of Pages 129	22. Price* A07

End of Document